

Applied Bionics and Biomechanics

Bionics and Human Biomechanics Applied in Intelligent Crash Tests of Cars

Lead Guest Editor: Tao Xu

Guest Editors: Tatsuo Yoshino, Shujun Zhang, Guowu Wei, and Zhixin Liu





Bionics and Human Biomechanics Applied in Intelligent Crash Tests of Cars

Applied Bionics and Biomechanics

Bionics and Human Biomechanics Applied in Intelligent Crash Tests of Cars

Lead Guest Editor: Tao Xu

Guest Editors: Tatsuo Yoshino, Shujun Zhang, Guowu Wei,
and Zhixin Liu



Copyright © 2019 Hindawi. All rights reserved.

This is a special issue published in “Applied Bionics and Biomechanics.” All articles are open access articles distributed under the Creative Commons Attribution License, which permits unrestricted use, distribution, and reproduction in any medium, provided the original work is properly cited.

Editorial Board

Andrea Cereatti, Italy
Laurence Cheze, France
Christian Cipriani, Italy
Jose L. Contreras-Vidal, USA
Agnès Drochon, France
Fabio Esposito, Italy
Ángel Gil-Agudo, Spain
Eugenio Guglielmelli, Italy
Hiroaki Hobara, Japan

Zhongmin Jin, China
Kiros Karamanidis, Germany
Justin Keogh, Australia
Jan Harm Koolstra, Netherlands
Thibault Lemaire, France
Le Ping Li, Canada
Andrea Marinozzi, Italy
Craig P. McGowan, USA
Jose Merodio, Spain

Juan C. Moreno, Spain
Estefanía Peña, Spain
Simo Saarakkala, Finland
Fong-Chin Su, Taiwan
Wei Tan, USA
Amir A. Zadpoor, Netherlands
Stefano Zaffagnini, Italy
Li-Qun Zhang, USA
Nigel Zheng, USA

Contents

Bionics and Human Biomechanics Applied in Intelligent Crash Tests of Cars

Tao Xu , Tatsuo Yoshino , Shujun Zhang, Guowu Wei, and Zhixin Liu 

Editorial (2 pages), Article ID 8750413, Volume 2019 (2019)

Biobjective Optimization Algorithms Using Neumann Series Expansion for Engineering Design

Huan Guo, Yoshino Tatsuo , Lulu Fan , Ao Ding , Tianshuang Xu , and Genyuan Xing

Research Article (13 pages), Article ID 7071647, Volume 2018 (2019)

Development and Validation of Dummies and Human Models Used in Crash Test

Tao Xu , Xiaoming Sheng , Tianyi Zhang , Huan Liu , Xiao Liang , and Ao Ding 

Review Article (12 pages), Article ID 3832850, Volume 2018 (2019)

Biomechanical Responses and Injury Characteristics of Knee Joints under Longitudinal Impacts of Different Velocities

Yan Xiong, Xueliang Zhao, Hongyi Xiang, Yunjiao Wang, Zhikang Liao, Xiyan Zhu, and Hui Zhao 

Research Article (11 pages), Article ID 1407345, Volume 2018 (2019)

Numerical Low-Back Booster Analysis on a 6-Year-Old Infant during a Frontal Crash Test

I. L. Cruz-Jaramillo , C. R. Torres-San-Miguel, O. Cortes-Vásquez, and L. Martínez-Sáez

Research Article (6 pages), Article ID 2359262, Volume 2018 (2019)

Numerical Analysis of Occupant Head Injuries in Impacts with Dump Truck Panel

Shence Wang , Deshun Liu, and Zhihua Cai 

Research Article (9 pages), Article ID 8373479, Volume 2018 (2019)

Editorial

Bionics and Human Biomechanics Applied in Intelligent Crash Tests of Cars

Tao Xu ¹, Tatsuo Yoshino ¹, Shujun Zhang,² Guowu Wei,³ and Zhixin Liu ⁴

¹School of Mechanical Science and Engineering, Jilin University, Changchun, China

²School of Computing and Technology, University of Gloucestershire, Cheltenham, UK

³School of Computing, Science & Engineering, University of Salford, Salford, UK

⁴China Automotive Technology and Research Center (CATARC), Tianjin, China

Correspondence should be addressed to Tao Xu; xutao@jlu.edu.cn

Received 21 October 2018; Accepted 21 October 2018; Published 8 January 2019

Copyright © 2019 Tao Xu et al. This is an open access article distributed under the Creative Commons Attribution License, which permits unrestricted use, distribution, and reproduction in any medium, provided the original work is properly cited.

1. Introduction

Improving crash safety of cars has become an important content in the research of automotive safety. The optimum design of intelligent crash test technology and devices for automotive safety has become a hot issue in the field. In order to test active safety or passive safety by braking or crash tests, intelligent testing devices (also called anthropomorphic test devices (ATDs) or crash test dummies) need to describe and simulate the damage mechanism and the tolerance limit of biological characteristics of the human body, such as dynamics and kinematics response to impact or acceleration. This is essential to protect human beings from car accidents.

Along with the increasing exploration of nature, organisms with rigid flexible coupling structures are gradually discovered, which have excellent performances such as impact resistance, abrasion resistance, and drag reduction. The combination of bionics and biomechanics constantly brings about new inspiration and innovation to the field of engineering and automotive safety. So, this special issue called for original research articles on basic biomechanical researches of the human body, computer simulation for human body modeling and analysis, new development of intelligent anthropomorphic test devices for measuring the response of the human body in certain environments where an impact or other loadings are applied to the body, and the application of bionic structures in automobiles to improve their anticollision performance. The contents can

involve bionics, biomechanics, automobile engineering, human body modeling, impact and contact mechanics, materials science of skin, and high-precision sensor informatics and mechanical processing technology. The highly integrated dummy design is also subject to various standard calibration tests, so this special issue is a cross-discipline.

2. Injury Criteria

In crash tests of cars, each part of the occupant could be injured to varying degrees. Some injury criteria of key parts are shown in Table 1, and the specific meanings of the symbols can be found in [1].

3. Description of the Special Issue

This special issue accepted 5 papers out of 10 after careful reviewing by editors, which leads to an acceptance ratio of 50%. The 5 papers focus on crash dummy improvement, injury characteristics of knee joints, and injury in some special conditions.

T. Xu et al. review the development and validation of dummies and human models used in crash tests. The mechanical dummies are introduced according to the collision types: frontal impact dummy, side impact dummy, and rear impact dummy. And the human model section details WSU, HUMOS, THUMS, and GHBMC human models. From the article, we can see the technological progress of the dummies and the human body models.

TABLE 1: Injury criteria of key parts.

Part	Injury criterion	Formula
Head	HIC	$HIC = (t_2 - t_1) \left[\frac{1}{t_2 - t_1} \int_{t_1}^{t_2} a dt \right]^{2.5}$
Neck	N_{ij}	$N_{ij} = (F_z/F_{int}) + (M_y/M_{int})$
Chest	CTI	$CTI = (A_{max}/A_{int}) + (D_{max}/D_{int})$
Tibia	TI	$TI = (M_R/M_{R\ max}) + (F_Z/F_{Z\ max})$

Injury criteria and biomechanical tests in early time are also introduced.

Y. Xiong et al. explore the mechanical response and injury characteristics of knee joints at different speeds using impact experiment with cadaveric knee samples and finite element simulation. The tests are all carried under conditions of longitudinal impacts, and the results all show that low-speed impact mainly leads to medial injuries, while high-speed impact leads to both medial and lateral injuries. The study can provide research basis for the prevention and treatment of longitudinal impact injuries of knee joints.

S. Wang et al. use finite element models to analyze how the panel design parameters can affect occupant head injuries. The paper focuses on the three factors of panel hardness, elastic modulus of the filling and frame, and the distance from fixed location. The findings indicate that a soft panel with a long fixing distance is beneficial for the head prevention.

I. L. Cruz-Jaramillo et al. study the head injury criterion (HIC) and chest severity index (CSI) with a 6-year-old Hybrid III dummy in the low-back booster (LBB) passive safety system. The findings of this study suggest that using materials, the attachment system of the LBB and the belt restraint system properly placed over the infant trunk are the main factors to reduce the injury criterion rate.

H. Guo et al. applied a novel biobjective algorithm Newton Neumann Series Expansion Frisch Algorithm (NNSEFA) to dummy head FE experiment. By optimizing the dummy head with the algorithm, the improved model has a better accuracy in the collision simulation. The application of the biobjective optimization algorithm provides new ideas for occupant safety design.

Conflicts of Interest

The Guest Editorial team as a whole declares that any member of the team does not have any conflict of interest or private agreements with companies.

Acknowledgments

We want to thank all the authors and reviewers for their valuable work to disseminate and curate the content of this special issue. We hope that this special issue can contribute to the discussion of the scientific community to focus on some

routes of the research and to enhance some gaps that can be filled in future works.

Tao Xu
Tatsuo Yoshino
Shujun Zhang
GuoWu Wei
Zhixin Liu

References

- [1] K. U. Schmitt, P. F. Niederer, M. H. Muser, and F. Walz, *Trauma Biomechanics: Accidental Injury in Traffic and Sports*, Springer, 2009.

Research Article

Biobjective Optimization Algorithms Using Neumann Series Expansion for Engineering Design

Huan Guo,^{1,2} Yoshino Tatsuo ,¹ Lulu Fan ,¹ Ao Ding ,³ Tianshuang Xu ,¹
and Genyuan Xing¹

¹School of Mechanical Science and Engineering, Jilin University, Changchun, China

²Aviation University of Air Force, Changchun, China

³Tianjin Aerisafety Science and Technology Co. Ltd., Tianjin, China

Correspondence should be addressed to Tianshuang Xu; xts@jlu.edu.cn

Received 5 April 2018; Revised 27 August 2018; Accepted 19 September 2018; Published 19 December 2018

Academic Editor: Jose Merodio

Copyright © 2018 Huan Guo et al. This is an open access article distributed under the Creative Commons Attribution License, which permits unrestricted use, distribution, and reproduction in any medium, provided the original work is properly cited.

In this paper, two novel algorithms are designed for solving biobjective optimization engineering problems. In order to obtain the optimal solutions of the biobjective optimization problems in a fast and accurate manner, the algorithms, which have combined Newton's method with Neumann series expansion as well as the weighted sum method, are applied to deal with two objectives, and the Pareto optimal front is achieved through adjusting weighted factors. Theoretical analysis and numerical examples demonstrate the validity and effectiveness of the proposed algorithms. Moreover, an effective biobjective optimization strategy, which is based upon the two algorithms and the surrogate model method, is developed for engineering problems. The effectiveness of the optimization strategy is proved by its application to the optimal design of the dummy head structure in the car crash experiments.

1. Introduction

It is very important to research on the multiobjective optimization problems in the engineering designs. For example, the economist fuel, the maximum carrying capacity, and the lightest weight need to be considered at the same time in the design of aircraft and spacecraft [1]; the strong rigidity, lightweight, and low-order modes also need to be considered commonly in the thin-walled beam section optimization problem of the automobile body structure design [2]. According to the investigation on the dummy head under automobile impact condition, the peak of synthetic acceleration of frontal and lateral drop is the main indicators of mechanical characteristics of dummy head [3]. A bilevel optimization was carried out for the cross-sectional shape of a thin-walled car body frame constrained with static and dynamic stiffness [4]. The common coin of these engineering problems is complex mechanical structure and too much design variables always lead to the intricate solving procedure and large amount of

computation with the purpose of multiple objectives meeting the best simultaneously. However, in most cases, the change of one target may cause an influence on the other ones. It is almost impossible to get a solution which can make each objective function reach the optimal value [5]. Therefore, the importance of carrying out the research of multiobjective optimization is of significance to engineering itself especially.

In most cases, an optimal solution which meets all objectives at the same time in a multiobjective problem does not exist. Thus, the key to describe an optimization problem is establishing a scientific and reasonable standard. However, it is also an effective and acceptable way to keep all object values on a relatively better level in the case that the optimal solutions cannot be obtained simultaneously. So, designers can choose one from several groups of the relatively better designs to guide decisions based on engineering background knowledge. The concept of Pareto optimal solution in a multiobjective optimization problem is an objective description which can take into account of every object thoroughly, so

that optimization schemes can be calculated by designers in the circumstances of keeping the whole optimization level from dropping [6].

The idea of solving numerical multiobjective optimization problem is a scalarization process, which uses a suitable scalar (single objective) optimization problem instead of the vector (multiobjective) optimization problem [7]. The commonly used algorithms are provided for scalarization process such as minimax method [8], constraint method [9], and usual weighted sum method [10].

The proposed minimax method is a classical multiobjective optimization algorithm [8]. By proving that the set of Pareto optimal solutions coincides with the set of stationary points, it is a parameter-free optimization method for computing a point satisfying a certain first-order necessary condition in multiobjective optimization. It borrows the idea of Newton's method for single-objective optimization and with respect to the authors' theoretical results obtained; Newton's method for multiobjective optimization behaves exactly as its counterpart for single-criterion optimization: it is fairly robust with respect to the dimension of the problem and the starting point chosen, the rate of convergence is at least superlinear, and it is quadratic if the second derivatives are Lipschitz-continuous. But the authors did not discuss the adaptation of the approach they proposed for constrained multiobjective problems. Quasi-Newton's method for solving multiobjective was proposed by Qu et al. [11] and Povalej [12]. By using the well-known BFGS method and the idea of [8], the authors had proven that quasi-Newton's method for multiobjective optimization converges superlinearly to the solution of the given problem, if all functions involved are twice continuously differentiable and strongly convex. The advantage of this method, compared to Newton's approach, is that the approximation of Hessian matrices is usually reasonably faster than their actual evaluation. This difference is especially noticeable when the dimension of the problem rises. The adaptation of this approach to constrained multiobjective optimization is not considered too.

The representative constraint method is ε -constraint method [9]; it retains the objective function which designers most prefer, as an objective function of single-objective optimization function, turning other objective functions into constraints by adding a restriction domain ε_i [13]. This algorithm has high efficiency and produces Pareto solutions which have a relatively broad range and does not need to make a priority of getting each objective function in grading (to determine the weight) [6]. However, ε -constraint method cannot guarantee that the result is a Pareto optimal solution; selecting an appropriate constraint value often requires some prior knowledge and has a low calculating efficiency when the number of objective function increases. The main drawbacks of these common methods are the limitations on calculation and dissatisfactions with the quality of Pareto optimal solutions [14].

The weighted sum method has been widely used because of its simplicity and high computational efficiency [15]. The early usual weighted sum method transforms multiple objectives into an aggregated objective function by multiplying each objective function by a weighted factor and adding them

up. But it has two drawbacks: difficulty to obtain Pareto optimal solutions uniformly and failure to solve nonconvex problems [16–18].

Many methods for solving nonconvex optimization problems have been proposed over the decades. Typical one is the normal-boundary intersection method (NBIM) [19]. It approaches a group of Pareto optimal solutions through geometric intuition parametric method and gives an accurate pattern of Pareto front. NBIM can not only obtain the Pareto optimal solutions in nonconvex regions but also the solutions are uniformly distributed. However, there are still serious defects, for example, non-Pareto optimal solutions (dominated solutions) are also obtained which must be filtered out. The adaptive weighted sum method (AWSM) is presented for the biobjective optimization problems [20], by adding inequality constraints based on traditional weighted sum methods and redefining feasible regions of optimization problems. So, the solve area is extended, and the optimal solutions are iterated automatically.

There are many biobjective optimization problems in engineering applications. The increase of each objective value will immediately cause an influence on another one. For example, energy-absorbing and impact force are a typical pair of contradictory optimized objectives in bumper-crash box design, which needs to make the maximum of impact force decrease while maximize energy absorption to the peak value. But in the practical engineering, with the rising of energy absorption, the impact force of the crash box will be even greater. So, the biobjective optimization is of great significance in engineering.

In this paper, two new algorithms for biobjective optimization problem are presented. One is Newton Neumann Series Expansion Algorithm (NNSEA) for unconstrained problem and Newton Neumann Series Expansion Frisch Algorithm (NNSEFA) for constrained problems. Two examples are given to demonstrate the valid and effectiveness of the algorithms, respectively. Finally, two algorithms are applied to the optimization problem in a dummy head design, and some good results are obtained. The following sections will discuss them in detail.

2. Newton Weighted Sum Algorithm for Unconstrained Multiobjective Optimization

2.1. Definition and Some Theories of the Multiobjective Optimization Problems. In order to accurately describe the concept of Pareto optimal solution, some definitions and symbols of multiobjective optimization will be presented first.

In this paper, denote by N_+ the positive integer set, by R the real number set, by R^n the n -dimensional real vector space, and by $R^{m \times n}$ the linear space which is composed of n -order real matrix. The Euclidean norm in R^n will be denoted by $\|\cdot\|$, and we will use the same notation $\|\cdot\|$ to describe the induced operator norms on the corresponding matrix spaces. $\mathbf{x} = (x_1, x_2, \dots, x_n)^T \in R^n$ is a vector of design variables. $F(\mathbf{x}) = (f_1(\mathbf{x}), f_2(\mathbf{x}), \dots, f_l(\mathbf{x}))^T \in R^l$ is the vector-valued objective function which components $f_j(\mathbf{x}) = f_j(x_1, x_2, \dots, x_n)$ are n -variable real functions for all $j = 1, 2, \dots, l$.

A general multiobjective optimization problem can be defined as follows:

$$\begin{cases} \min & F(\mathbf{x}), \\ \text{s.t.} & \mathbf{x} \in U \subset R^n, \end{cases} \quad (1)$$

where $F(\mathbf{x})$ is called the objective vector-valued function and U is the feasible region of (1). U can be described by

$$U = \{\mathbf{x} \in R^n \mid c_j(\mathbf{x}) = 0, c_i(\mathbf{x}) \leq 0, j = 1, \dots, m_e, i = m_e + 1, \dots, m\}, \quad (2)$$

where $c_j(\mathbf{x}) = 0$ and $c_i(\mathbf{x}) \geq 0$ are the equality and inequality constraints of multiobjective optimization, respectively. If $U = R^n$, (1) is called an unconstrained multiobjective optimization problem.

For solving (1), we provide the concept of Pareto optimality as explained below.

Definition 1. A point $x^* \in U$ is a local Pareto optimum or local Pareto optimal solution of $f(x)$ if and only if there does not exist $x \in U$ such that

$$f(x) \leq f(x^*), \quad x \neq x^*. \quad (3)$$

Note that if U and $f(x)$ are both convex, then the local Pareto optimality is equivalent to the global Pareto optimality. So a Pareto optimal solution means the reasonable solution, which satisfies the objectives at an acceptable level without being dominated by any other solution.

In order to obtain the information of every objective function and the change tendency of optimization process more intuitively, the set of objective function values can be used in case of making impolitic decision. The detailed definition is as below.

Definition 2. If $V \subset R^n$ is the set of Pareto optimal solutions in (1), then set P is a Pareto front of V for which

$$P = \{F(\mathbf{x}) = (f_1(\mathbf{x}), f_2(\mathbf{x}), \dots, f_l(\mathbf{x})) \mid \mathbf{x} \in V\} \quad (4)$$

holds.

Assume $f_j(\mathbf{x})$ is twice continuously differentiable on feasible region U , i.e., $f_j(\mathbf{x}) \in C^2(U)$. And for $\mathbf{x} \in U \subset R^n$, let $\nabla f_j(\mathbf{x}) \in R^n$ and $\nabla^2 f_j(\mathbf{x}) \in R^{n \times n}$ denote the gradient and Hessian matrix of $f_j(\mathbf{x})$ at \mathbf{x} for all $j = 1, 2, \dots, m$, respectively.

Throughout the paper, unless explicitly mentioned, we will assume that $f_j(\mathbf{x}) \in C^2(U)$ with strong convexity which implies the $\nabla^2 f_j(\mathbf{x})$ is positive definite for all $\mathbf{x} \in U \subset R^n$, and $j = 1, 2, \dots, m$.

2.2. Newton Method Based on Weighted Sum Technique. Newton's method is extensively used in optimization problem, and the iteration direction includes the gradient and

Hessian matrix information of objectives. When the initial iteration point is very close to the optimal point, the rate of convergence is rapid. And if the objective functions satisfy some conditions, it can achieve superlinear convergence or quadratic convergence. So in multiobjective optimization problem, Newton method combined with weighted sum method is chosen as the main calculation algorithm. The derivation process is as follows.

In the multiobjective optimization problem (1), $f_j(\mathbf{x}) \in C^2(U)$, the Taylor expansion of $f_j(\mathbf{x})$ around $\mathbf{x}_k \in U$ is

$$\begin{aligned} f_j(\mathbf{x}) &= f_j(\mathbf{x}_k) + \nabla f_j(\mathbf{x}_k)(\mathbf{x} - \mathbf{x}_k) \\ &+ \frac{1}{2}(\mathbf{x} - \mathbf{x}_k)^T \nabla^2 f_j(\mathbf{x}_k)(\mathbf{x} - \mathbf{x}_k) + o(\|\mathbf{x} - \mathbf{x}_k\|^2). \end{aligned} \quad (5)$$

Hence, the second order approximate Taylor expansion of $f_j(\mathbf{x})$ around $\mathbf{x}_k \in U$ is

$$f_j(\mathbf{x}) \approx f_j(\mathbf{x}_k) + \nabla f_j(\mathbf{x}_k)(\mathbf{x} - \mathbf{x}_k) + \frac{1}{2}(\mathbf{x} - \mathbf{x}_k)^T \nabla^2 f_j(\mathbf{x}_k)(\mathbf{x} - \mathbf{x}_k). \quad (6)$$

Here, in (6), $\nabla^2 f_j(\mathbf{x}_k)$ is positive definite. Hence, the problem is converted from finding the minimum of $f_j(\mathbf{x})$ into finding the second order approximation minimum of $f_j(\mathbf{x})$. Since from the derivative of (6) at both sides with respect to \mathbf{x} , using the necessary condition of extreme value, we obtain

$$\nabla f_j(\mathbf{x}_k) + \nabla^2 f_j(\mathbf{x}_k)(\mathbf{x} - \mathbf{x}_k) = 0. \quad (7)$$

Considering the algorithm is an iterative process, take $\mathbf{x} = \mathbf{x}_{k+1}$, we have the Newton iteration method for single objective as

$$\mathbf{x}_{k+1} = \mathbf{x}_k - \left[\nabla^2 f_j(\mathbf{x}_k) \right]^{-1} \nabla f_j(\mathbf{x}_k). \quad (8)$$

And note the iteration direction of Newton's method for a single objective at \mathbf{x}_k

$$\mathbf{d}_k = \mathbf{x}_{k+1} - \mathbf{x}_k = - \left[\nabla^2 f_j(\mathbf{x}_k) \right]^{-1} \nabla f_j(\mathbf{x}_k). \quad (9)$$

For solving problem (1), by weighted sums of $f_j(\mathbf{x})$ for all $j = 1, 2, \dots, m$, we have the sum function which will be denoted by $F_\lambda(\mathbf{x})$. Hence,

$$\begin{aligned} F_\lambda(\mathbf{x}) &= \sum_{j=1}^l \lambda_j f_j(\mathbf{x}) \\ &= \sum_{j=1}^l \lambda_j \left[f_j(\mathbf{x}_k) + \nabla f_j(\mathbf{x}_k)^T \mathbf{d}_k + \frac{1}{2} \mathbf{d}_k^T \nabla^2 f_j(\mathbf{x}_k) \mathbf{d}_k \right], \end{aligned} \quad (10)$$

where the weighting factors will be denoted by λ_j and $\lambda_j \geq 0$, $\sum_{j=1}^l \lambda_j = 1$ for all $j = 1, 2, \dots, l$.

Expression (10) can be calculated as the derivative at both sides with respect to \mathbf{d}_k , then, the iterative formula of Newton weighted sum algorithm for (1) is

$$\mathbf{x}_{k+1} = \mathbf{x}_k - \left[\sum_{j=1}^l \lambda_j \nabla^2 f_j(\mathbf{x}_k) \right]^{-1} \sum_{j=1}^l \lambda_j \nabla f_j(\mathbf{x}_k). \quad (11)$$

So, we can conclude the direction of Newton weighted sum algorithm for (1) at \mathbf{x}_k

$$\mathbf{d}_k = - \left[\sum_{j=1}^l \lambda_j \nabla^2 f_j(\mathbf{x}_k) \right]^{-1} \sum_{j=1}^l \lambda_j \nabla f_j(\mathbf{x}_k). \quad (12)$$

3. Neumann Series Expansion

The Neumann series is the expansion of the matrix inversion, and its function lies in the efficiency of the matrix inversion. In engineering, the problem can be solved by the Newton method, and when there are many design variables, a considerable amount of calculation is needed. But when there are two object functions, the introduction of expansion principle can not only maintain the advantages of the Newton method but also reduce the work by half that is needed to run two object functions. The theorem is as follows:

Theorem 1. Assume that $\mathbf{K} \in R^{n \times n}$ is a n -order invertible matrix. Then, for matrix $\Delta \mathbf{K} \in R^{n \times n}$, there exists $\mathbf{N} = \mathbf{K}^{-1} \Delta \mathbf{K}$, and when $\|\mathbf{N}\| < 1$, such

$$\bar{\mathbf{K}}^{-1} = (\mathbf{K} + \Delta \mathbf{K})^{-1} = (\mathbf{K}(\mathbf{I} + \mathbf{K}^{-1} \Delta \mathbf{K}))^{-1} = (\mathbf{I} + \mathbf{N})^{-1} \mathbf{K}^{-1}, \quad (13)$$

$$\bar{\mathbf{K}}^{-1} = (\mathbf{I} - \mathbf{N} + \mathbf{N}^2 + \dots + (-1)^m \mathbf{N}^m + \dots)^{-1} \mathbf{K}^{-1} \quad (14)$$

hold for $m \in N_+$. (14) is called the Neumann series expansion.

According to (10), the weighted sum function of problem (31) is

$$F_\lambda(\mathbf{x}) = \sum_{j=1}^2 \lambda_j f_j(\mathbf{x}), \quad (15)$$

and the corresponding Newton's iterative format is

$$\mathbf{x}_{k+1} = \mathbf{x}_k - \left[\sum_{j=1}^2 \lambda_j \nabla^2 f_j(\mathbf{x}_k) \right]^{-1} \sum_{j=1}^2 \lambda_j \nabla f_j(\mathbf{x}_k). \quad (16)$$

Then the iterative direction vector of (16) at \mathbf{x}_k is

$$\mathbf{d}_k = - \left[\sum_{j=1}^2 \lambda_j \nabla^2 f_j(\mathbf{x}_k) \right]^{-1} \sum_{j=1}^2 \lambda_j \nabla f_j(\mathbf{x}_k) \quad (17)$$

According to (17) and Neumann series expansion of Theorem 1, let \mathbf{K} be the square matrix $\lambda_1 \nabla^2 f_1(\mathbf{x}_k)$ in (13), and $\Delta \mathbf{K}$ be the square matrix $\lambda_2 \nabla^2 f_2(\mathbf{x}_k)$ in (13), therefore,

$$\begin{aligned} \mathbf{N} &= \mathbf{K}^{-1} \Delta \mathbf{K} = (\lambda_1 \nabla^2 f_1(\mathbf{x}_k))^{-1} (\lambda_2 \nabla^2 f_2(\mathbf{x}_k)) \\ &= \frac{\lambda_2}{\lambda_1} (\nabla^2 f_1(\mathbf{x}_k))^{-1} \nabla^2 f_2(\mathbf{x}_k). \end{aligned} \quad (18)$$

Define $\lambda = \lambda_2 / \lambda_1 > 0$ with $\lambda_1 + \lambda_2 = 1$. Then we should state $\|\mathbf{N}\| < 1$ holds with λ adjusted under some certain conditions.

Assume that $U \subset R^n$ is a bounded set, for $\mathbf{x} = (x_1, x_2, \dots, x_n)^T \in U$, then $G : R^n \rightarrow R^{n \times n}$ defined by (19) is a linear operator.

$$G(\mathbf{x}) = \nabla^2 f_j(\mathbf{x}) \in R^{n \times n}. \quad (19)$$

Boundedness and continuity of $G(\mathbf{x})$ are as follows.

Theorem 2. A linear operator $G : R^n \rightarrow R^{n \times n}$ is bounded if and only if there exists a constant $M > 0$, such that

$$\|G\mathbf{x}\| \leq M\|\mathbf{x}\|, \quad \mathbf{x} \in U \quad (20)$$

holds.

Proof. Assume that G is a bounded linear operator, so the unit ball $\bar{B}_1(\theta) = \{\mathbf{x} \in R^n \mid \|\mathbf{x}\| \leq 1\}$ can be mapped into a bounded set on $R^{n \times n}$ by G , i.e., the image set of $\bar{B}_1(\theta)$ is a bounded set on $R^{n \times n}$.

Take $M = \sup \{\|G\mathbf{x}\| \mid \mathbf{x} \in \bar{B}_1(\theta)\}$. If $\theta \in U$, then θ satisfies to (22). For any $\mathbf{x} \in U$, $\mathbf{x} \neq \theta$, we have $\mathbf{x}/\|\mathbf{x}\| \in \bar{B}_1(\theta)$ and

$$\left\| G \left(\frac{\mathbf{x}}{\|\mathbf{x}\|} \right) \right\| \leq M, \quad (21)$$

i.e.,

$$\|G\mathbf{x}\| \leq M\|\mathbf{x}\|, \quad \mathbf{x} \in U, \mathbf{x} \neq \theta. \quad (22)$$

Therefore, if G is a bounded linear operator, then (22) holds.

Inversely, assume that (22) holds. The boundedness of $U \subset R^n$ implies that there exists a positive constant M_1 such that

$$\|\mathbf{a}\| \leq M_1, \text{ for } \mathbf{a} \in U. \quad (23)$$

And there exists $\mathbf{a} \in U$, such that

$$\mathbf{y} = G\mathbf{a} \quad (24)$$

holds for every $\mathbf{y} \in GU$. From (20), we have

$$\|\mathbf{y}\| = \|G\mathbf{a}\| \leq M\|\mathbf{a}\| \leq M \cdot M_1. \quad (25)$$

Therefore, $\sup \{\|\mathbf{y}\|: \mathbf{y} = \mathbf{G}\mathbf{a}, \mathbf{a} \in U\} \leq M \cdot M_1$, i.e., GU is a bounded set on $\mathbb{R}^{n \times n}$.

Theorem 3. A linear operator $G: \mathbb{R}^n \rightarrow \mathbb{R}^{n \times n}$ is continuous if and only if G is bounded.

Proof. (The necessary condition). Assume G is unbounded, then the inequality (20) is not satisfied. Hence, if there exists $\mathbf{x}_n \in \mathbb{R}^n$, such that

$$\|\mathbf{G}\mathbf{x}_n\| > n\|\mathbf{x}_n\| \quad (26)$$

holds for any natural number n . Take $\mathbf{y}_n = \mathbf{x}_n/n\|\mathbf{x}_n\|$, we have

$$\|\mathbf{G}\mathbf{y}_n\| > 1, \|\mathbf{y}_n\| = \frac{1}{n} \rightarrow 0 (n \rightarrow \infty), \quad (27)$$

therefore, $\mathbf{y}_n \rightarrow \theta$ but $\mathbf{G}\mathbf{y}_n \rightarrow \theta$ which is contradictory to the continuity of G .

(The sufficient condition). From the inequality (20), if $\mathbf{x}_n \rightarrow \theta$, then we have

$$\|\mathbf{G}\mathbf{x}_n\| \leq M\|\mathbf{x}_n\| \rightarrow 0 (n \rightarrow \infty), \quad (28)$$

therefore, $\mathbf{G}\mathbf{x}_n \rightarrow \theta$ and G is continuous.

Because of $G(\mathbf{x}) = \nabla^2 f_j(\mathbf{x})$ and under the assumption of $\nabla^2 f_j(\mathbf{x})$ is continuous matrix function for $j = 1, 2$. Therefore, the linear operator G is bounded on $U \subset \mathbb{R}^n$.

From the foregoing, we concluded that G is a continuous and bounded linear operator, so $\|\mathbf{G}(\mathbf{x})\|$ has an upper bound W_1 on U . Similarly, linear operator $G^{-1}(\mathbf{x}) = \nabla^2 f_j(\mathbf{x})^{-1}$ and $\|\mathbf{G}^{-1}(\mathbf{x})\|$ have their own upper bound $W'_1 = 1/W_1$ on U for $j = 1, 2$. So, back to (18) and the compatibility of norms, we can have

$$\begin{aligned} \|\mathbf{N}\| &= \frac{\lambda_2}{\lambda_1} \left\| (\nabla^2 f_1(\mathbf{x}_k))^{-1} \nabla^2 f_2(\mathbf{x}_k) \right\| \\ &\leq \frac{\lambda_2}{\lambda_1} \|\nabla^2 f_1(\mathbf{x}_k)^{-1}\| \cdot \|\nabla^2 f_2(\mathbf{x}_k)\|. \end{aligned} \quad (29)$$

In (29), $\|\nabla^2 f_1(\mathbf{x}_k)^{-1}\| \cdot \|\nabla^2 f_2(\mathbf{x}_k)\|$ has a public upper bound which denoted by $W > 0$. Hence, it can fully satisfy the requirement of $\|\mathbf{N}\| < 1$ by adjusting $\lambda = \lambda_2/\lambda_1$ appropriately.

4. An Algorithm for Unconstrained Biobjective Optimization Problem Based on Neumann Series Expansion (NSE)

When there are only two objective functions, a biobjective optimization algorithm is established in this paper by introducing the technique of NSE [21] to Newton weighted sum method. With this algorithm, the complicated inverse calculation of n -rank matrix is avoided. It is only needed to calculate the inversion once for Hessian matrix of one objective function in (1). So the operating speed is improved especially in a high-dimensional design variables condition. Hence, the

proposed algorithm is named as Newton Neumann Series Expansion Algorithm (NNSEA).

When there are only two objective functions, rewrite the problem (1) as

$$\begin{aligned} F(\mathbf{x}) &= \min (f_1(\mathbf{x}), f_2(\mathbf{x}))^T, \\ \text{s.t.} \quad &\begin{cases} c_i(\mathbf{x}) = 0, & i = 1, 2, \dots, m_e, \\ c_i(\mathbf{x}) \leq 0, & i = m_e + 1, \dots, m. \end{cases} \end{aligned} \quad (30)$$

Note that when the feasible region U is extended to \mathbb{R}^n , the constraints are invalid and (30) can be turned into unconstrained biobjective optimization as

$$F(\mathbf{x}) = \min_{\mathbf{x} \in \mathbb{R}^n} (f_1(\mathbf{x}), f_2(\mathbf{x}))^T. \quad (31)$$

The whole process of NNSEA for calculating a biobjective Pareto optimal solution is symbolized by Algorithm 1 as follows.

By selecting multiple groups of weighting factors, each group can obtain a Pareto optimal solution and the corresponding Pareto front. The process of NNSEA for solving unconstrained biobjective is shown in Figure 1.

5. NNSEFA Based on NNSEA

NNSEA is a method for solving unconstrained biobjective optimization problem. But the design variables are mostly under some inequality constraints in engineering application. Therefore, to improve the NNSEA by handling constraints is of great significance in engineering case. By introducing a penalty function, the constraints can be transformed to penalty terms and integrated into objective functions. Based on the NNSEA and combined with Frisch's penalty function method, the proposed algorithm for solving constrained biobjective optimization is named Newton Neumann Series Expansion Frisch Algorithm (NNSEFA).

5.1. Handling the Constraints with Frisch Penalty Function. The Frisch penalty function is one of the interior penalty function methods by employing a logarithm to handle with the constraint. In problem (30) with constraints

$$c_i(\mathbf{x}) \leq 0, \quad i = 1, 2, \dots, m. \quad (32)$$

The penalty term is constructed by Frisch's method, which is expressed as

$$q(\mathbf{x}) = -\frac{1}{\sigma} \sum_{i=1}^m \log(-c_i(\mathbf{x})). \quad (33)$$

When the penalty term $q(\mathbf{x})$ is closer to zero, it means that design variables satisfy the constraints. During the solving process, $q(\mathbf{x})$ should be scaled down until it is small enough to be neglected compared to the object values. At this moment, the obtained solution can not only be equivalent to the optimal solution of the original problem but also satisfy the constraints. The process of NNSEFA is as follows.

(Initialization)

Step 1 Choose $\mathbf{x}_0 \in U$ and a set of weighting factors (λ_1, λ_2) , and stopping criteria denoted by a small value $\varepsilon > 0$, solve $\nabla f_j(\mathbf{x}_0)$ for $j = 1, 2$, $\nabla^2 f_1(\mathbf{x}_0)^{-1}$, $\nabla^2 f_2(\mathbf{x}_0)$.

(Main loop)

Step 2 If $\|\sum_{j=1}^2 \lambda_j \nabla f_j(\mathbf{x}_k)\| \leq \varepsilon$, then stop and output \mathbf{x}_k . Else, go to Step 3.

Step 3 Solve $\mathbf{N} = \lambda_2/\lambda_1 [\nabla^2 f_1(\mathbf{x}_k)]^{-1} \nabla^2 f_2(\mathbf{x}_k)$,

If $\|\mathbf{N}\| < 1$, the direction is

$$\mathbf{d}_k = -(1/\lambda_1)(\mathbf{I} - \mathbf{N} + \mathbf{N}^2 - \mathbf{N}^3) \nabla^2 f_1(\mathbf{x}_k)^{-1} [\sum_{j=1}^2 \lambda_j \nabla f_j(\mathbf{x}_k)];$$

Else, adjust weighting factors λ_1 and λ_2 to satisfy with $\|\mathbf{N}\| < 1$.

(Update)

Step 4 Define $\mathbf{x}_{k+1} = \mathbf{x}_k + \mathbf{d}_k$.

Step 5 Set $k := k + 1$, go to Step 2.

ALGORITHM 1

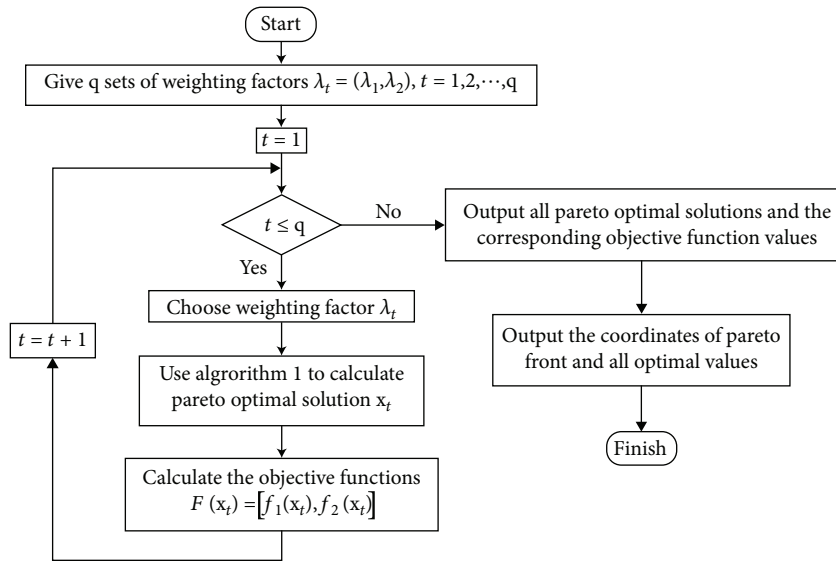


FIGURE 1: The process of NNSEA for solving unconstrained biobjective optimization.

First, denote the logarithmic penalty function of $f_j(\mathbf{x})$ as

$$p_j(\mathbf{x}) = f_j(\mathbf{x}) - \frac{1}{\sigma} \sum_{i=1}^m \log(-c_i(\mathbf{x})), \quad (34)$$

the Taylor expansion of $p_j(\mathbf{x})$ around $\mathbf{x}_k \in U$ is

$$\begin{aligned} p_j(\mathbf{x}) &= p_j(\mathbf{x}_k) + \nabla p_j(\mathbf{x}_k)(\mathbf{x} - \mathbf{x}_k) \\ &+ \frac{1}{2} (\mathbf{x} - \mathbf{x}_k)^T \nabla^2 p_j(\mathbf{x}_k) (\mathbf{x} - \mathbf{x}_k) + o(\|\mathbf{x} - \mathbf{x}_k\|^2). \end{aligned} \quad (35)$$

Hence, the second order approximation Taylor expansion of $p_j(\mathbf{x})$ around $\mathbf{x}_k \in U$ is

$$p_j(\mathbf{x}) \approx p_j(\mathbf{x}_k) + \nabla p_j(\mathbf{x}_k)(\mathbf{x} - \mathbf{x}_k) + \frac{1}{2} (\mathbf{x} - \mathbf{x}_k)^T \nabla^2 p_j(\mathbf{x}_k) (\mathbf{x} - \mathbf{x}_k). \quad (36)$$

Then, by adding $p_j(\mathbf{x})$ together for $j = 1, 2$, a sum function denoted by $P_\lambda(\mathbf{x})$ which can be expressed as

$$\begin{aligned} P_\lambda(\mathbf{x}) &= \sum_{j=1}^2 \lambda_j p_j(\mathbf{x}) \\ &= \sum_{j=1}^2 \lambda_j \left[p_j(\mathbf{x}_k) + \nabla p_j(\mathbf{x}_k)^T \mathbf{d} + \frac{1}{2} \mathbf{d}^T \nabla^2 p_j(\mathbf{x}_k) \mathbf{d} \right], \end{aligned} \quad (37)$$

where $\sum_{j=1}^2 \lambda_j = 1$ and $\lambda_j > 0$.

By taking derivative of (37) at both sides with respect to \mathbf{d} , the iterative formula is

$$\mathbf{x}_{k+1} = \mathbf{x}_k - \left[\sum_{j=1}^2 \lambda_j \nabla^2 p_j(\mathbf{x}_k) \right]^{-1} \sum_{j=1}^2 \lambda_j \nabla p_j(\mathbf{x}_k). \quad (38)$$

So, the iteration direction at \mathbf{x}_k is

$$\mathbf{d}_k = - \left[\sum_{j=1}^2 \lambda_j \nabla^2 p_j(\mathbf{x}_k) \right]^{-1} \sum_{j=1}^2 \lambda_j \nabla p_j(\mathbf{x}_k). \quad (39)$$

Just like NNSEA, by calculating $\mathbf{N} = \lambda_2/\lambda_1 [\nabla^2 p_1(\mathbf{x}_k)]^{-1} \nabla^2 p_2(\mathbf{x}_k)$, and based on the value of $\|\mathbf{N}\|$, we choose the direction properly. In order to ensure all the directions are descending during the optimization, an identification process is introduced. Taking the negative gradient direction of sum function, i.e., $\mathbf{d}_k = -\sum_{j=1}^2 \lambda_j \nabla p_j(\mathbf{x}_k)$. The criterion of this strategy is the product of Newton direction and negative gradient direction denoted by

$$a_k = - \left(\sum_{j=1}^2 \lambda_j \nabla p_j(\mathbf{x}_k) \right)^T \left(\sum_{j=1}^2 \lambda_j \nabla^2 p_j(\mathbf{x}_k) \right)^{-1} \sum_{j=1}^2 \lambda_j \nabla p_j(\mathbf{x}_k). \quad (40)$$

5.2. NNSEFA for Constrained Biobjective Optimization Problem. The whole process of NNSEFA for calculating a constrained biobjective Pareto optimal solution is symbolized by Algorithm 2 as follows.

Similarly, by selecting multiple groups of weighting factors, each group can obtain a Pareto optimal solution and the corresponding Pareto front. The process of NNSEFA for solving inequality constrained biobjective is shown in Figure 2.

6. Numerical Examples

Two benchmark test examples are chosen to test the effectiveness of NNSEA and NNSEFA. The first is an example from a published paper [22] for NNSEA. The second one is from the Genetic Algorithm Toolkit (GATool) of MATLAB for NNSEFA.

6.1. Test 1.

$$\min F(\mathbf{x}) = \begin{cases} F_1 = (x_1 - 1)^2 + (x_1 - x_2)^2, \\ F_2 = (x_2 - 3)^2 + (x_1 - x_2)^2. \end{cases} \quad (41)$$

Start coding in MATLAB 7.9.0(R2009b) for NNSEA, and set $\varepsilon = 10^{-5}$, weighting factors $\lambda = (\lambda_1, \lambda_2)$ are generated in $(0, 1)$. Initial point $\mathbf{x}_0 = (x_1, x_2)^T = (1, 0)^T$. Note that the weighting factors are generated in two approaches, one is generated randomly, and another is provided uniformly. Then start the calculation and output the coordinates of Pareto front with all 200 groups of optimal solutions in Figures 3 and 4.

As can be seen in Figures 3 and 4, each red asterisks represents a Pareto optimal function value of one specific set of weighting factor. And all the function values compose the Pareto front. The blue asterisks and blue lines represent the iterative points and descent directions in the whole process. 200 groups of Pareto optimal solutions are all convergent and distributed uniformly and broadly. In this paper, the calculations are executed 20 times by each weighting factor

generate approach, the detailed information is listed in Table 1. It is clear that this NNSEA has high performance and good adaptability for biobjective optimization problem.

6.2. Test 2.

$$\min F(\mathbf{x}) = \begin{cases} F_1 = x_1^4 - 10x_1^2 + x_1x_2 + x_2^4 - x_1^2x_2^2, \\ F_2 = x_2^4 - x_1^2x_2^2 + x_1^4 + x_1x_2, \end{cases} \\ \text{s.t.} \quad \begin{cases} -5 \leq x_1 \leq 5, \\ -5 \leq x_2 \leq 5. \end{cases} \quad (42)$$

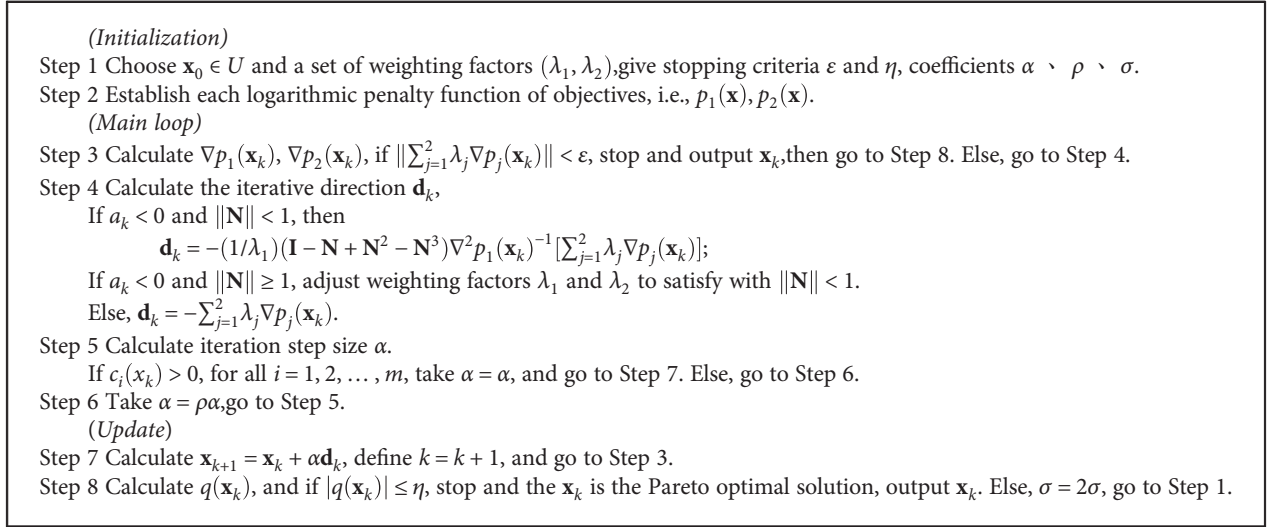
Similarly, in test 2 we set $\varepsilon = 10^{-5}$ and weighting factors are generated in $(0, 1)$ randomly. Initial point is $\mathbf{x}_0 = (x_1, x_2)^T = (2, -2)^T$, and set coefficients $\alpha = 0.9, \rho = 0.9, \eta = 0.05$ with initial $\sigma = 2$, the iterative number for calculating every Pareto optimal solution is no more than 200. Then start the calculation and output the coordinates of Pareto front with all 200 groups of optimal solutions in Figure 5.

Only the Pareto front is displayed for giving an observation of function values more clearly. In the biobjective optimization problem, the middle section of Pareto front should be emphatically focused because of the values of this section, without favoring either function. We can see the middle section of the red asterisks, which are arranged smoothly and compactly, in Figure 6. Executed 20 times in the same computer and recorded, the average time of calculation is 270.85 s with the average number of iterative for each Pareto solution of 8.54, and all the Pareto optimal solutions are convergent which means NNSEFA has a good performance of efficiency and convergence.

7. Biobjective Optimization for Dummy Head in Car Crash Experiment

With the rapid development of automobile industry, the passive safety of automobiles has become a more and more important research subject for enterprises and research institutes. As an anthropomorphic test device, collision dummies are widely used in automobile safety testing. The collision dummy is made up of the head, neck, chest, buttocks, upper limbs, and lower limbs. Head injury is one of the most common injuries in traffic accidents, and statistics show that the mortality caused by head injury is the highest, which accounts for 68% of all deaths, making head injury the greatest killer in car accidents [23]. Therefore, research on dummy head structure in automobile crashes is essential to head injury analysis and vehicle safety.

7.1. Modeling of Biobjective Optimization Problem for Dummy Head Design. In this paper, to improve the efficiency of the dummy head analysis, a simplified dummy head model is developed based on the finite element (FE) model of Hybrid III 50th. Sensitivity analysis and the equivalent modeling in mechanics are applied to developing the new simplified dummy head structure. Through sensitivity analysis of the materials used for dummy head structure such as



ALGORITHM 2

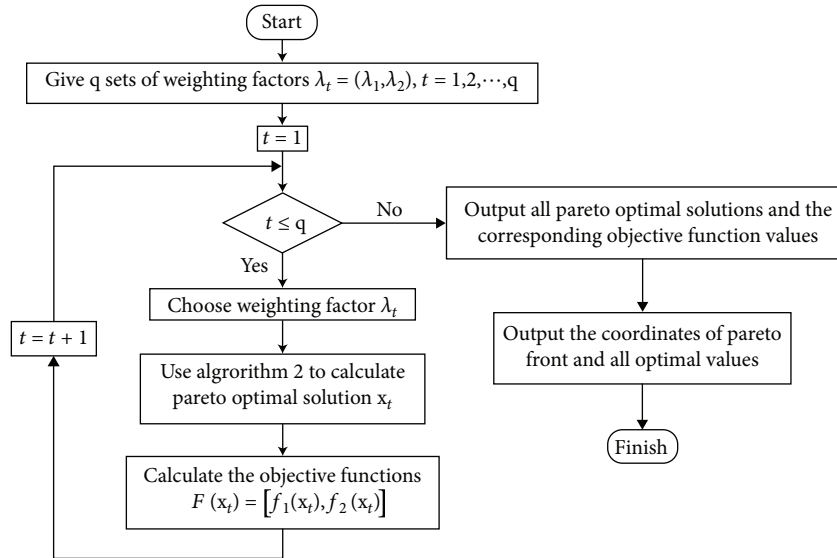


FIGURE 2: The process of NNSEFA for solving inequality constraints biobjective optimization.

artificial skin and bones and mechanical property response, a simplified dummy head model is proposed in this section. In Figure 7(b), the detailed FE model of the proposed simplified head model is given and the dummy head FE model of Hybrid III 50th is shown in Figure 7(a). All models in this paper are meshed by software HyperMesh and then solved in LS-DYNA and meshed with shell and body elements.

For the dummy head calibration test, there is a legal and authoritative standard to examine the validity of the dummy structure. The synthetic head acceleration generated in automobile crashes is applied to evaluating the mechanical properties of the head structure. Considering the frontal and lateral impact condition, the peak accelerations of the dummy head generated in frontal and lateral collision are denoted as a_{frb} and a_{mdb} , respectively. The accuracy of the dummy head model is comprehensively considered by using

the method of frontal and lateral head regulation, and thus the peak a_{frb} and a_{mdb} are used as the main indexes of the mechanical characteristics of the dummy head. In simulating the collision process of the head structure, the models drop from a certain height and hit a rigid plate, as shown in Figure 8. The simulation processes of the dummy head in frontal and lateral collisions are presented in Figures 8(a) and 8(b), respectively.

7.2. *Validity of the Dummy Head Model.* Acceleration curves of the simplified dummy head models under frontal (FRB) and lateral (MDB) impacts are obtained, and calibration test is referred for comparison analysis. Thus, two acceleration-time curves compared with the test curves of the dummy head model under different collision stations are depicted in Figure 9. In Figure 9, the green curves are obtained in

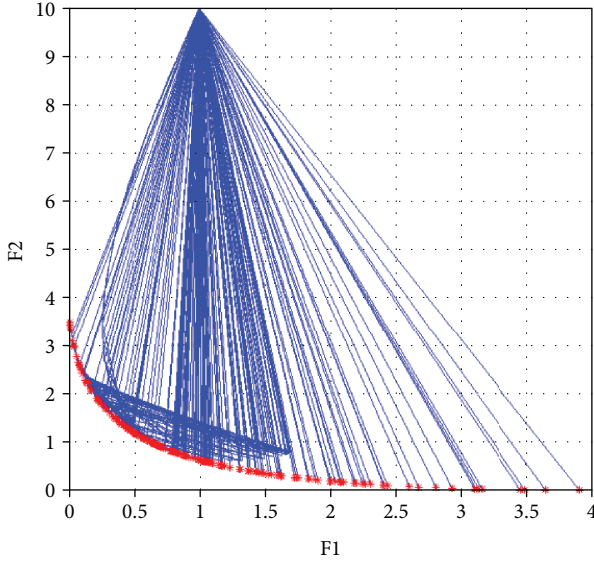


FIGURE 3: The Pareto optimal front of test 1 (random distribution).

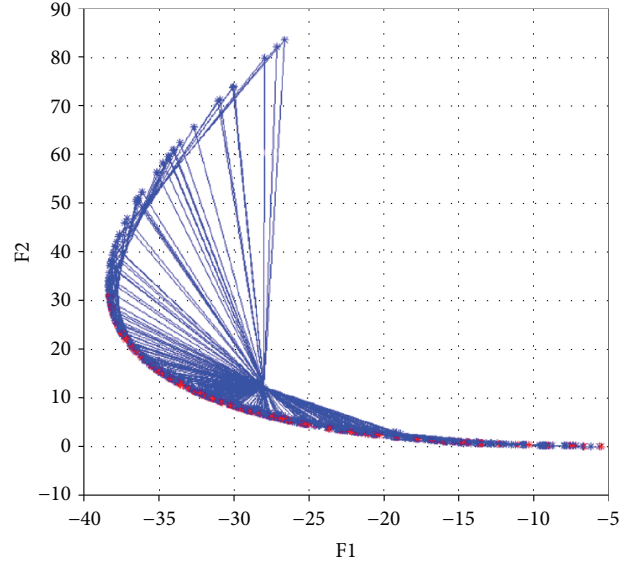


FIGURE 5: The Pareto optimal front of test 2 (contains each iteration).

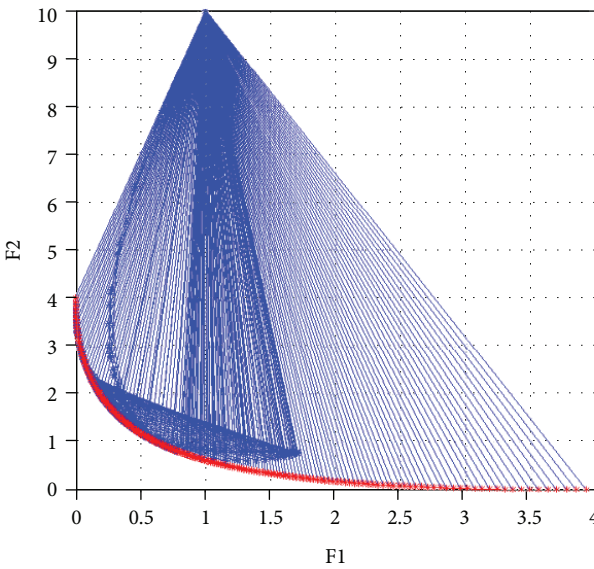


FIGURE 4: The Pareto optimal front of test 1 (uniform distribution).

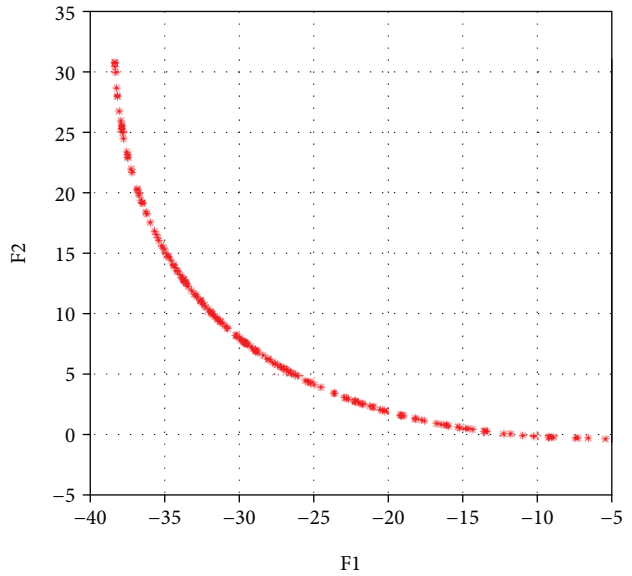


FIGURE 6: The Pareto optimal front of test 2.

TABLE 1: The average calculating time and iteration information of NNSEA for solving test 1.

Weighting factor	Average time	Average number of iterations	Convergence
Random distribution	185.32 s	13.48	Yes
Uniform distribution	144.24 s	12.33	Yes

simulated dummy test, and the blue curves in physical dummy test. Moreover, Figure 9(a) is in frontal impact and Figure 9(b) in lateral collision.

According to Figure 9, the acceleration-time curves of the simplified dummy head model proposed in this paper

is consistent with the experimental results, and also, the two peak acceleration values a_{frb} and a_{mdb} meet the calibration requirement. The quantitative analysis of the two peak accelerations compared with the test results are carried out in Table 2, and the errors in peak acceleration between the simplified model and physical dummy head are also considered in this paper.

From Table 2, we can conclude that the two peak acceleration values are all within calibration range, which means that the simplified dummy head model developed in this paper is effective and can be used in the simulation research of the head injuries. However, the figures in Table 2 also present a fact that the error of the peak acceleration of simplified head model is greater; thus, the accuracy of the head model

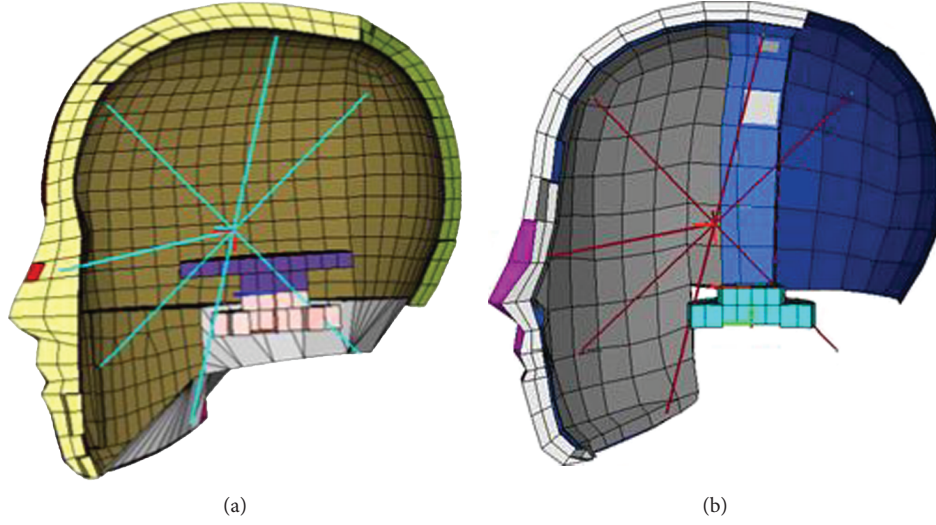


FIGURE 7: Detailed FE models of Hybrid III 50th and the simplified head structure.

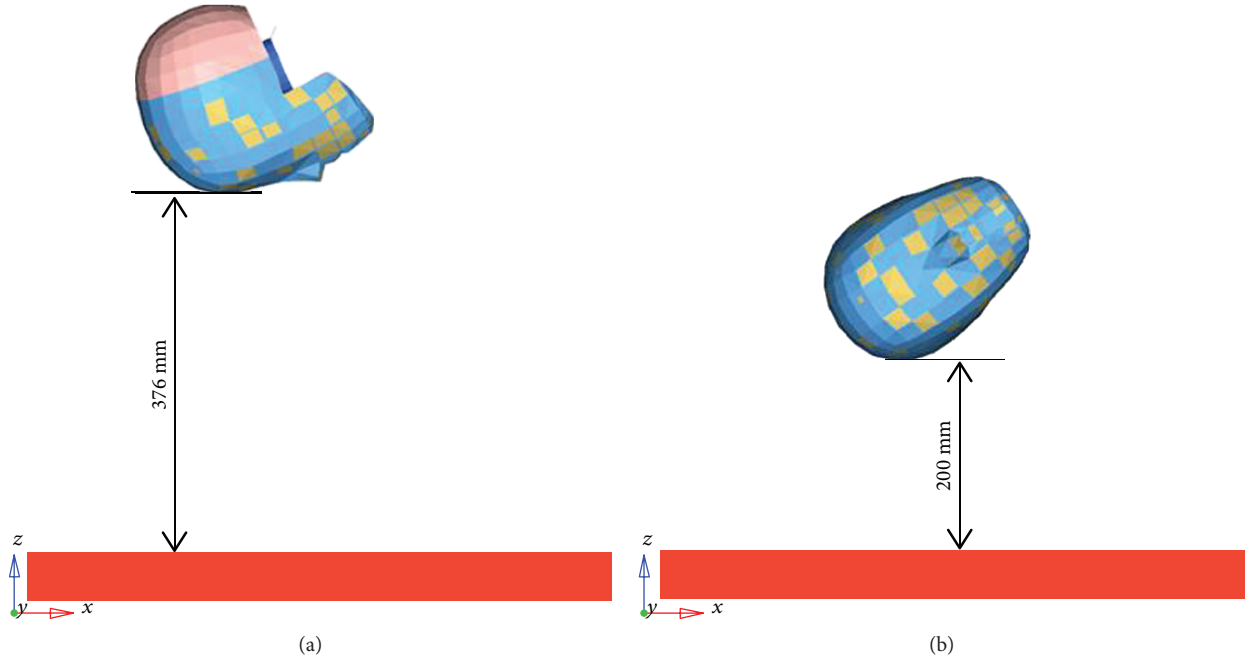


FIGURE 8: Two forms of frontal and lateral impacts.

cannot be guaranteed in some cases. Therefore, an optimization design of the dummy head structure will be carried out in the following section to improve the accuracy of the simplified head model.

7.3. Establishment of Mathematical Model for Optimization Design of the Dummy Head. According to Wood et al. [24], the mechanical responses of dummy head in automobile collision are typically dependent on the viscoelastic properties of the head polymer skin. In order to improve the accuracy of the simplified dummy head proposed in this paper, three material parameters—relaxation modulus (GI), shear modulus (MU1), and decay constant (BETA)—are selected as design variables based on the material sensitivity and the research on physical properties. Considering the frontal and

lateral collision, thus the optimization design of the dummy head is a biobjective optimization problem. Thus, a biobjective optimization problems for optimization design of the dummy head structure is established as follows:

$$\begin{cases} \min & (F_1 = |a_{fr0} - a_{frb}(x)|, F_2 = |a_{m0} - a_{mdb}(x)|), \\ \text{s.t.} & l_i \leq x_i \leq u_i, \quad i = 1, 2, 3, \end{cases} \quad (43)$$

where F_1 and F_2 are two objectives; $a_{fr0} = 250.14$ g, and $a_{m0} = 137.1$ g are the experiment values of the peak acceleration of the dummy head, while $a_{frb}(x)$ and $a_{mdb}(x)$ are acceleration peak values of the simplified model under frontal and lateral impact conditions. And $x_i, i = 1, 2, 3$ are design variables that

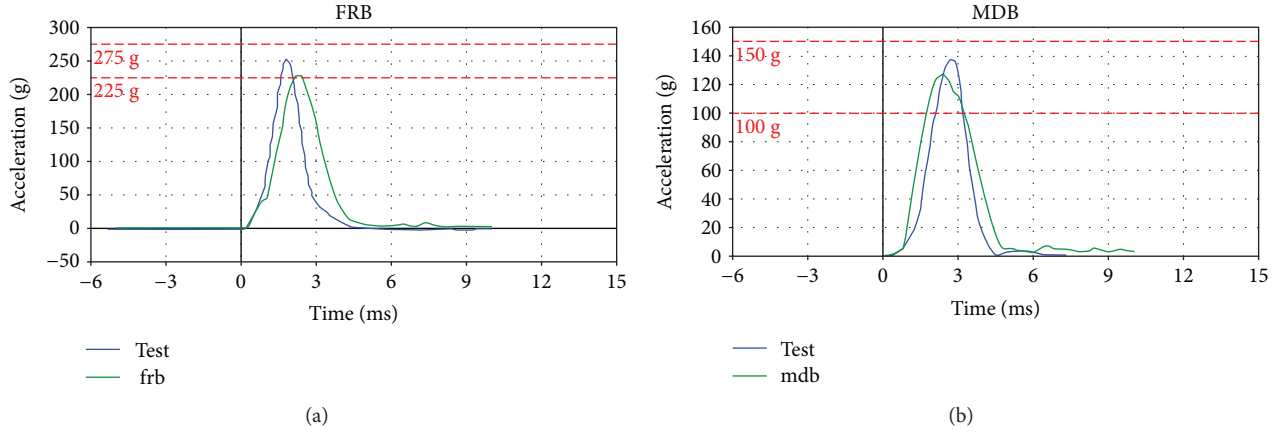


FIGURE 9: The acceleration-time curves of the dummy head model under frontal and lateral collisions.

TABLE 2: Comparison of two peak accelerations between simplified head model and physical dummy head.

Model	Design variables			Acceleration	
	x_1 (Gpa)	x_2 (Gpa)	x_3	a_{frb}/g	a_{mdb}/g
Original design	0.0015	$7.5e-4$	0.3	230.5	127.8
Calibration requirement	—	—	—	225–275	100–150
Test result	—	—	—	250.14	137.1
Error	—	—	—	-7.85%	-6.78%

consist of GI, MU1, and BETA; according to the calibration test design requirements, in this paper, $x_1 \in [0.0005, 0.005]$, $x_2 \in [7e-4, 1e-3]$, $x_3 \in [0.3, 1.2]$.

7.4. Establishment of Surrogate Model of Dummy Head. To reduce the complexity of the optimization problem in practical engineering, surrogate modeling has been broadly applied to many fields for its simple theory and excellent function. In this simulation, the response surface methodology (RSM) is selected for its better performance in many multiobjective optimization problems [25–27]. Firstly, 16 groups data (3 factors 4 levels) are obtained by the orthogonal experimental design (DOE) method, and the corresponding acceleration results performed in LS-DYNA are shown in Table 3.

According to the data in Table 3, the quadratic polynomial response surface models of the objective functions F_1 and F_2 are constructed as equation (44) and (45).

$$\begin{aligned}
 F_1 = & 49.30481 - 16344.7x_1 - 2419.06x_2 - 38.0611x_3 \\
 & - 101547x_1^2 - 3.9E + 07x_2^2 + 4.4533029x_3^2 \\
 & + 15829917x_1x_2 + 3693.5245x_1x_3 + 48179.205x_2x_3,
 \end{aligned} \tag{44}$$

$$\begin{aligned}
 F_2 = & 26.32685 - 1454.22x_1 - 43582.2x_2 + 15.05433x_3 \\
 & + 109443.5x_1^2 + 32371025x_2^2 - 0.72198x_3^2 \\
 & - 2137901x_1x_2 + 1413.658x_1x_3 - 16641x_2x_3.
 \end{aligned} \tag{45}$$

TABLE 3: 16 groups obtained by DOE and its corresponding response.

Number	x_1 (GI)	x_2 (MU1)	x_3 (BETA)	$ a_{fr0} - a_{frb} $	$ a_{m0} - a_{mdb} $
1	0.0005	$7e-4$	0.3	25.64	11.2
2	0.0005	$7.5e-4$	0.6	24.54	11.8
3	0.0005	$8e-4$	0.9	25.24	12.1
4	0.0005	$1e-3$	1.2	26.64	11.1
5	0.0015	$7e-4$	0.6	23.24	10.9
6	0.0015	$7.5e-4$	0.3	19.64	9.3
7	0.0015	$8e-4$	1.2	30.24	11.8
8	0.0015	$1e-3$	0.9	27.84	10.0
9	0.0035	$7e-4$	0.9	19.44	9.4
10	0.0035	$7.5e-4$	1.2	29.24	9.9
11	0.0035	$8e-4$	0.3	11.84	4.0
12	0.0035	$1e-3$	0.6	16.94	5.7
13	0.005	$7e-4$	1.2	22.84	11.6
14	0.005	$7.5e-4$	0.9	17.44	7.0
15	0.005	$8e-4$	0.6	16.14	4.6
16	0.005	$1e-3$	0.3	12.34	1.4

Then, after surrogate models are obtained, the determination coefficient of variance analysis is employed to verify the fitting precision of response surface models. In general, if the determination coefficient is closer to 1, the surrogate model function with respect to response variables is more precise. In the paper, the determination coefficients R_{frb}^2 and R_{mdb}^2 [27] are 93.153% and 98.8691%, respectively. Therefore, the surrogate models in this paper can simulate response variables accurately.

7.5. Optimization Design of the Dummy Head Structure. The effective optimization strategy proposed in this paper is applied to the biobjective optimization design of the dummy head structure. Following the optimal process of the strategy NNSEFA, the Pareto optimal solutions of the biobjective problem (43) are obtained quickly and after comparative analysis, an optimal scheme with design variables $x_1 =$

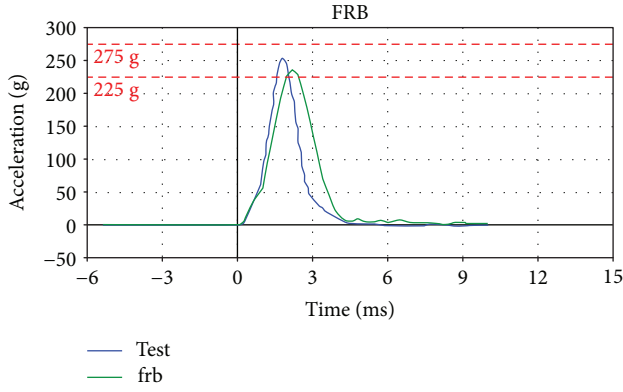


FIGURE 10: Acceleration-time curves of the dummy head under frontal collision.

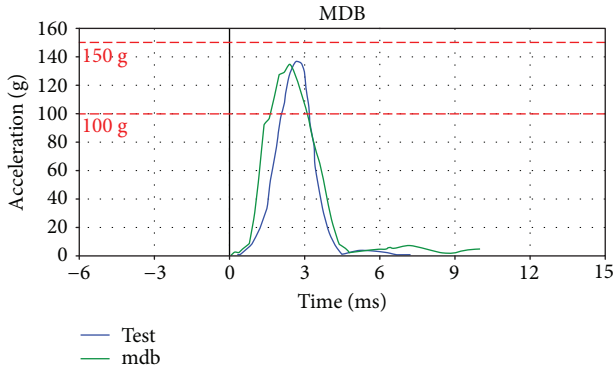


FIGURE 11: Acceleration-time curves of the dummy head under lateral collision.

0.0056 Gpa, $x_2 = 6e-4$ Gpa, and $x_3 = 0.3$ is selected for optimization design of the simplified dummy head model. The two accelerations were considered to evaluate the performance of the optimal design. Figures 10 and 11 show the acceleration-time curves of the optimal dummy head model compared with the physical dummy head structure under frontal and lateral collision, respectively. Moreover, the green curves in Figures 10 and 11 are obtained through the simulated dummy head experiment and the blue curves through physical dummy test.

According to the acceleration-time curves presented in Figures 10 and 11, the optimal design of the dummy head structure satisfy the calibration requirement, and its peak value of the two accelerations is close to the acceleration value obtained in the experiment of the physical dummy head. In addition, the acceleration-time curves of the optimal design are consistent with the experimental results. To analyze the properties of the optimal dummy head model, the design scheme and its two corresponding responses are shown in Table 4.

From Table 4, the degree of the optimizations for the simplified dummy head model is obvious and appreciable. Firstly, the peak values of acceleration for the frontal and lateral drop of the dummy head model is in accordance with the

TABLE 4: Detailed design variables and its corresponding responses compared with the original design and the result obtained by test.

Model	Design variables			Acceleration	
	x_1 (Gpa)	x_2 (Gpa)	x_3	a_{frb}/g	a_{mdb}/g
Original model	0.0015	7.5e-4	0.3	230.5	127.8
Optimal design	0.0054	6e-4	0.3	236.7	136.0
Calibration requirement	—	—	—	225–275	100–150 <i>reference goes here</i>
Test result	—	—	—	250.14	137.1
Error	—	—	—	-5.37%	-0.80%
Optimal percentage	—	—	—	2.48%	5.98%

calibration test completely. The peak synthesis acceleration of frontal head drop is 236.7g, the error of the simulated model being -5.37% , reduced by 2.48% compared with the original model before optimization, and the synthetic acceleration peak in lateral drop is 136.0g, the deviation from the peak of the test curve being -0.80% , reduced by 5.98% after optimization. It can be seen that the optimal model of the dummy head is not only effective but also accurate in calculation. In addition, the dummy head model has been simplified for high computation efficiency, and the biojective optimization performed in the optimal design has made the model more accurate. In summary, the optimization scheme for dummy head structure is of high accuracy and can be applied to the study on the occupant safety protection.

8. Conclusion

Two algorithms—NNSEA and NNSEFA—are presented in this paper. In NNSEA, the Neumann series expansion is introduced in Newton's weighted sum method so it can simplify the calculation on matrix inversion. And based on NNSEA, Frisch penalty function is employed to handle the constraints. So NNSEFA can achieve biojective optimization with constraints. When the objective functions are strong convex, the proposed NNSEA and NNSEFA are two efficient approaches for biojective optimization problems according to the test function analysis.

In the engineering application of dummy, NNSEFA provides valuable reference to designers. As computer simulation shows, the general calibration curve, the peak and the peak time for the optimized model of dummy head, and physical dummy are very consistent. Compared with the original design, this optimization model can simulate the injury of human head in the collision process more accurately. It provides the design idea for occupant safety design. Obviously, the optimization is feasible.

Data Availability

The data used to support the findings of this study are available from the corresponding author upon request.

Conflicts of Interest

The authors declare no conflicts of interest.

Acknowledgments

The authors would like to acknowledge the National Natural Science Funds for Distinguished Young Scholar (Grant No. 51505181), the China Postdoctoral Science Foundation funded project (No. 2016M590256), the Advanced Manufacturing Project of Provincial School Construction of Jilin Province (No. SXGJSF2017-2), and the Science & Technological Project of Smart Manufacturing in Tianjin supported by Tianjin Science and technology commission (No. 16ZXZNGX00100).

References

- [1] C. A. C. Coello, *An empirical study of evolutionary techniques for multiobjective optimization in engineering design*, Tulane University, New Orleans, Louisiana, USA, 1996.
- [2] H. Wang, Z.-D. Ma, N. Kikuchi, C. Pierre, and B. Raju, "Multi-domain multi-step topology optimization for vehicle structure crashworthiness design," in *SAE Technical Paper Series*, March 2004.
- [3] C. Libo, Z. Jiadong, and J. Wu, *Finite Element Model for Child Dummy Head of Q6 and Validation*, Mechanical Science and Technology for Aerospace Engineering, 2016.
- [4] W. Zuo, "Bi-level optimization for the cross-sectional shape of a thin-walled car body frame with static stiffness and dynamic frequency stiffness constraints," *Proceedings of the Institution of Mechanical Engineers, Part D: Journal of Automobile Engineering*, vol. 229, no. 8, pp. 1046–1059, 2015.
- [5] C. Chih-Ming, C. Ying-ping, and Z. Qingfu, "Enhancing MOEA/D with guided mutation and priority update for multi-objective optimization," in *2009 IEEE Congress on Evolutionary Computation*, vol. 18-21, pp. 209–216, Trondheim, Norway, May 2009.
- [6] G. Mavrotas, "Effective implementation of the ϵ -constraint method in multi-objective mathematical programming problems," *Applied Mathematics and Computation*, vol. 213, no. 2, pp. 455–465, 2009.
- [7] R. T. Marler and J. S. Arora, "The weighted sum method for multi-objective optimization: new insights," *Structural and Multidisciplinary Optimization*, vol. 41, no. 6, pp. 853–862, 2010.
- [8] J. Fliege, L. M. G. Drummond, and B. F. Svaiter, "Newton's method for multiobjective optimization," *SIAM Journal on Optimization*, vol. 20, no. 2, pp. 602–626, 2009.
- [9] C. Vira and Y. Y. Haimes, *Multiobjective Decision Making: Theory and Methodology*, North Holland, 1983xvii.
- [10] A. M. Geoffrion, "Proper efficiency and the theory of vector maximization," *Journal of Mathematical Analysis and Applications*, vol. 22, no. 3, pp. 618–630, 1968.
- [11] S. Qu, M. Goh, and F. T. S. Chan, "Quasi-Newton methods for solving multiobjective optimization," *Operations Research Letters*, vol. 39, no. 5, pp. 397–399, 2011.
- [12] Ž. Povalej, "Quasi-Newton's method for multiobjective optimization," *Journal of Computational and Applied Mathematics*, vol. 255, pp. 765–777, 2014.
- [13] T. Takahama, S. Sakai, and N. Iwane, "Constrained optimization by the ϵ constrained hybrid algorithm of particle swarm optimization and genetic algorithm," in *AI 2005: Advances in Artificial Intelligence*, Lecture Notes in Computer Science, S. Zhang and R. Jarvis, Eds., pp. 389–400, Springer Berlin Heidelberg, Berlin, Heidelberg, 2005.
- [14] T. Takahama and S. Sakai, "Constrained optimization by the ϵ -constrained differential evolution with an archive and gradient-based mutation," in *IEEE Congress on Evolutionary Computation*, vol. 18–23, pp. 1–9, Barcelona, Spain, July 2010.
- [15] R. T. Marler and J. S. Arora, "Survey of multi-objective optimization methods for engineering," *Structural and Multidisciplinary Optimization*, vol. 26, no. 6, pp. 369–395, 2004.
- [16] K. Il Yong and W. Olivier de, "Adaptive weighted sum method for multiobjective optimization," in *10th AIAA/ISSMO Multidisciplinary Analysis and Optimization Conference*, Albany, NY, USA, August 2004.
- [17] I. Das and J. E. Dennis, "A closer look at drawbacks of minimizing weighted sums of objectives for Pareto set generation in multicriteria optimization problems," *Structural Optimization*, vol. 14, no. 1, pp. 63–69, 1997.
- [18] A. Messac and C. A. Mattson, "Generating well-distributed sets of Pareto points for engineering design using physical programming," *Optimization and Engineering*, vol. 3, no. 4, pp. 431–450, 2002.
- [19] I. Das and J. E. Dennis, "Normal-boundary intersection: a new method for generating the Pareto surface in nonlinear multicriteria optimization problems," *SIAM Journal on Optimization*, vol. 8, no. 3, pp. 631–657, 1998.
- [20] I. Y. Kim and O. L. de Weck, "Adaptive weighted-sum method for bi-objective optimization: Pareto front generation," *Structural and Multidisciplinary Optimization*, vol. 29, no. 2, pp. 149–158, 2005.
- [21] F. Yamazaki, A. Member, M. Shinozuka, and G. Dasgupta, "Neumann expansion for stochastic finite element analysis," *Journal of Engineering Mechanics*, vol. 114, no. 8, pp. 1335–1354, 1988.
- [22] M. Sefrioui and J. Perlaux, "Nash genetic algorithms: examples and applications," in *Proceedings of the 2000 Congress on Evolutionary Computation. CEC00 (Cat. No.00TH8512)*, vol. 501, pp. 509–516, CA, USA, 2000.
- [23] T. A. N. G. Jun, *Simulation Study on Chinese Dummy Head Model*, Hunan University, Changsha, China, 2016.
- [24] G. W. Wood, M. B. Panzer, C. R. Bass, and B. S. Myers, "Viscoelastic properties of hybrid III head skin," *SAE International Journal of Materials and Manufacturing*, vol. 3, no. 1, pp. 186–193, 2010.
- [25] G. Sun, H. Zhang, J. Fang, G. Li, and Q. Li, "Multi-objective and multi-case reliability-based design optimization for tailor rolled blank (TRB) structures," *Structural and Multidisciplinary Optimization*, vol. 55, no. 5, pp. 1899–1916, 2017.
- [26] L. Fan, T. Yoshino, T. Xu, Y. Lin, and H. Liu, "A novel hybrid algorithm for solving multiobjective optimization problems with engineering applications," *Mathematical Problems in Engineering*, vol. 2018, Article ID 5316379, 15 pages, 2018.
- [27] G. Yang, T. Xu, X. Li, H. Xiu, and T. Xu, "An efficient hybrid algorithm for multiobjective optimization problems with upper and lower bounds in engineering," *Mathematical Problems in Engineering*, vol. 2015, Article ID 932029, 13 pages, 2015.

Review Article

Development and Validation of Dummies and Human Models Used in Crash Test

Tao Xu ¹, Xiaoming Sheng ¹, Tianyi Zhang ¹, Huan Liu ¹, Xiao Liang ¹,
and Ao Ding ²

¹School of Mechanical Science and Engineering, Jilin University, Changchun, China

²Tianjin Aerasafety Science and Technology Co. Ltd, Tianjin, China

Correspondence should be addressed to Tianyi Zhang; 297481719@qq.com

Received 6 April 2018; Revised 4 July 2018; Accepted 26 August 2018; Published 13 November 2018

Academic Editor: Andrea Cereatti

Copyright © 2018 Tao Xu et al. This is an open access article distributed under the Creative Commons Attribution License, which permits unrestricted use, distribution, and reproduction in any medium, provided the original work is properly cited.

The crash test dummy, an important tool for car crash safety tests, is of great significance to explore the injury biomechanics of the occupants and improve the safety performance of the vehicle. The article mainly consists of four parts: brief introduction of injury mechanism, early experiments for obtaining biomechanical response (animal tests, cadaver tests, and volunteer tests), and development and validation of mechanical dummies and computational models. This study finds that the current crash test dummies are generally designed based on European and American, so they have limitations on the damage prediction of other regions. Further research in the crash test dummy needs the participation of various countries in order to develop a crash test dummy that meets the national conditions of each country. Simultaneously, it is necessary to develop dummies of vulnerable groups, such as the elderly dummy and obese people dummy.

1. Introduction

Automobiles provide great convenience and quickness for people's life and make a great contribution to the economy and social development. However, with the rapid development of the automotive industry, road accidents have also suddenly increased, resulting in a large number of casualties and economic losses. According to the World Road Safety Global Status Report on Road Safety 2015 issued by the World Health Organization, it can be seen that the number of people who died from traffic accidents is roughly around 1.25 million every year, which means that one person is killed in traffic accidents every 25 seconds on a global scale. Traffic accidents are the main cause of death in the 15- to 29-year-old population [1]. China, the most populous country in the world, had a total of 187,781 road traffic accidents in 2015 [2]. The total direct property losses caused by the accident were 103,692 million yuan, of which the total number of injured people was 199,880, and the death toll was 58,022. These shocking figures all indicate that improving the safety protection for occupants and reducing the

casualties caused by traffic accidents have become an important issue to be solved urgently.

In fact, as early as the 1950s, in order to investigate the human injuries caused by collisions and correctly assess the actual injuries suffered by occupants in car collisions, researchers began to study the injury biomechanics of occupants in car collisions. Researchers used human corpses as surrogates to collect data on human injuries caused by accidents in crash experiments and subsequently adopted animals and volunteers as crash surrogates. Although these experiments provided valuable data for collision safety, they were gradually abandoned due to restrictions such as ethical and moral constraints, physiological function differences, experimental risks, and experimental irreproducibility. With the development of science and technology, crash detection device—mechanical crash test dummy, known as anthropometric test device (ATD), came into being. When dummy is subjected to physical quantities such as force, acceleration, and speed during a car crash, the mechanical response curve should be highly fitted to the data obtained from human cadaver experiments. Using the crash test dummy to perform

repeated crash tests, the injury location can be effectively predicted, and the injury indicators of the occupants can be estimated.

This paper reviews the development of dummies and is introduced from four aspects. The first is theoretical foundation of crash test dummy, named biomechanical injury mechanism. In order to study the injury mechanism, researchers conducted cadaver experiment, animal experiment, and volunteer test in early time, so the second aspect is about biomechanical test. The third and fourth aspects introduce the development and verification process of the mechanical dummies and computational models used in crash test.

2. Injury Criteria

The main purpose of crash test dummy used as a substitute for human in car collisions is to determine the injury severity to human body caused by the accident. Thus, understanding how the mechanical properties of dummy meet injury mechanism of human and correspond to the harm standard is absolutely essential. The current study believes that the blunt impact injury mechanism is the degree of deformation or strain of the tissue exceeding its recoverable limit [3]. In the car crash, the main load type of human exposure to injury is blunt impact. The main sites of injury are the head, neck, chest, abdomen, pelvis, and other parts of the extremities. In order to describe the human injury condition intuitively, according to the type of injury of the human body when it is damaged by impact, the corresponding injury index is formulated.

The Abbreviated Injury Scale (AIS) (shown in Table 1), proposed by the Association for the Advancement of Automotive Medicine (AAAM), standardized the injury types and ranked injury levels by severity. It is the most widely used measurement for crash injury currently. However, the dummy can only output parametric impact result rather than the visualized injury characterization. Therefore, it is important to seek the relationship between assessment of human injury by severity and loads on the dummy. Researchers fitted the risk assessment equation of the corresponding injury site through a large number of accident statistics and converted the experimental data into the corresponding injury types and severity in reality (shown in Table 2).

In car collisions, most of the deadly head injuries come from the impact fracture of the skull and the brain tissue injury. National Highway Traffic Safety Administration (NHTSA) raises the HIC value based on the acceleration to measure the max limit of injury to the human head in the collision of the car. The widely used HIC value is calculated by (1). The formula is as follows:

$$\text{HIC} = (t_2 - t_1) \left[\frac{1}{t_2 - t_1} \int_{t_1}^{t_2} a dt \right]^{2.5}, \quad (1)$$

where t_1 and t_2 (s) are two time points in the crash acceleration curve. a is measured as a multiple of the gravitational acceleration (g), and the equation uses a three-way

TABLE 1: Abbreviated injury score.

AIS code	Injury severity	AIS% prob. of death
1	Minor	0
2	Moderate	1–2
3	Serious	8–10
4	Severe	5–50
5	Critical	5–50
≥6	Unsurvivable	100

synthetic acceleration. It also stipulates that the time difference between t_1 and t_2 cannot exceed 36 ms; HIC value cannot exceed 1000 (tolerance limit). Hertz [4] fitted the relationship between HIC and the probability of skull fracture ($\text{AIS} \geq 2$) by experimental data and found that for 50th male, the probability of skull fracture was about 48% when HIC is 1000.

Neck injury has become the most frequent injury in car crash accident and also one of the most important causes of occupant's disability. NHTSA [5] proposes the guideline N_{ij} to evaluate the neck injury in frontal impact car crash. N_{ij} was defined by neck axial force F_z and force moment M_y . The formula is shown as follows:

$$N_{ij} = \frac{F_z}{F_{\text{int}}} + \frac{M_y}{M_{\text{int}}}. \quad (2)$$

The N_{ij} value can be used to estimate the neck injury on AIS1 level. Bohmann et al. [6] studied the neck injury on AIS1 and claimed that the tolerance limit should decrease to 0.2 and 0.16 for long term and short term damage, respectively.

When the chest suddenly is decelerated due to blunt instrument impact, the injury mechanisms include three main types: compression, viscous loads, and inertial loads of internal organs. Injury results can be categorized as skeletal injury and soft tissue injury. In general, the main forms of injury are rib fractures and lung injuries, as well as a smaller chance of heart bruises and ruptures and rupture and breakage of the aorta. The chest composite index represents a chest injury criterion in frontal impact. The response under compression coupled with acceleration is considered. At the same time, the load of the airbag to the occupant and the restraint effect of the seatbelt to the occupant are described. The definition of CTI is evaluated by a combination of the 3 ms resultant acceleration of the spine and the amount of deformation of the chest. The CTI value is calculated as follows:

$$\text{CTI} = \frac{A_{\text{max}}}{A_{\text{int}}} + \frac{D_{\text{max}}}{D_{\text{int}}}, \quad (3)$$

where A_{max} is the single peak value (g) of 3 ms for the resultant acceleration of the spine; A_{int} is the 3 ms intercept reference (g); D_{max} is the maximal chest deformation (mm); and D_{int} is the intercept reference value (mm) of the deformation.

The abdomen peak force (APF) was elaborated by European ECE R95 guideline and rules that the external force of abdomen should not exceed 4.5 kN.

TABLE 2: Common injury indicators for different parts of the human body.

Head	Neck	Chest	Abdomen	Pelvis and lower extremities
Acceleration (g)	Force (N)	Deformation (mm)		
HIC value	Force moment (N*m)	Acceleration (g)	Force (N)	Force (N)
	N_{ij} value	CTI value		

The injury mechanism of femoral fractures caused by collisions with dashboards, which often occurs in frontal crashes in cars, is mostly caused by axial compression (62%), followed by bending (24%), twisting (5%), and shear (5%). Because the femur is not completely straight, the shape of the femur will affect the fracture in the case of indirect loading. Similar to fractures of the femur, tibial fractures can also be caused by retrograde direct or indirect loads. Pubic symphysis peak force (PSPF) in ECE R95 rules that the collision force at the pubic symphysis should be less than 6 kN. The criteria for tibial fractures, also known as the tibial index, are used to evaluate the tibia injuries. It is calculated by the hinge restraint of the fixed hinge on the load sensor at the upper and lower positions of the sacrum, as defined by each force and moment value.

$$TI = \frac{M_R}{M_{RMAX}} + \frac{F_Z}{F_{ZMAX}}, \quad (4)$$

where F_Z refers to the axial pressure of the lower leg (kN); F_{ZMAX} refers to axial pressure threshold; $M_R = \sqrt{M_X^2 + M_Y^2}$; M_X and M_Y refer to bending moment of X and Y; and M_{RMAX} represents the synthetic bending moment threshold.

3. Biomechanical Tests in Early Time

To improve the car's ability to protect the occupant and reduce human injury during car collision, it is necessary to have a preliminary understanding of the occupant's biomechanical response during the collision. In the early stages, there are three kinds of biomechanical tests to explore biomechanical responses: volunteer tests, animal tests, and human cadaver tests.

In the field of volunteer test, US Air Force Colonel John P. Stapp is a well-known pioneer. He personally went through a series of tests and even sat on a rocket skateboard with a speed of up to 1000 km/h. His volunteer tests obtained valuable data which were later widely used in the injury biomechanics, such as human body acceleration tolerance data [7]. However, crash tests have certain risks, and volunteer tests are inevitably performed at low-speed and light-load conditions, such as head injury study at low rotational speeds [8] and spine deformation study at low-speed rear impacts [9]. For biomechanical studies under high-speed and heavy-load conditions, volunteer tests are obviously not suitable.

In order to study the physiological responses under heavy load conditions, some scholars conducted experiments on living animals. In 1980, Ono et al. [10] conducted a head impact experiment on live monkeys and found that impact acceleration, impact contact area, and other factors will affect

the head injury. When the brain of a monkey suffered a fracture, the tolerance value was at a dangerous threshold. Combining the obtained data with the results of the human cadaver skull impact test, a human head impact tolerance threshold can be deduced. In 1981, twelve anesthetized male pigs were used by Kroell et al. [11] to study the chest injury mechanism, injuries such as cardiovascular ruptures, pulmonary contusions, and skeletal fractures. The results emphasized the importance of loading speed for determining the overall severity of chest blunt impact. Although animal tests can provide a biological reflection basis, the animal body mass distribution and morphological characteristics are different from the human body. Therefore, the results of animal experiments have limited promotional value.

In general, fresh human cadaver is a better substitute for biomechanical studies of impact injury, and there are corresponding cadaveric tests to investigate the response of parts of the body (head, chest, etc.). Hodgson and Patrick [12] found that when the head of a cadaver received a sinusoidal vibration input, the mode frequency of the skull corresponds to spring-mass system. In response to this discovery, they proposed a method to compare the cadaver head response to spring-mass system. Kroell et al. [13, 14] conducted a series of tests to study the responses of cadaver's chest. 23 cadaver samples of different ages, heights, and weights were chosen to be used in tests. Impactor mass and velocity were in various combinations to apply to tests. These tests obtained valuable chest response data.

In the abovementioned volunteer tests, animal tests, and cadaver tests, there are significant drawbacks such as experimental risks, physical differences, and violating ethics. Therefore, developing a new human substitute to apply to the research on vehicle impact injury biomechanics is important. The substitute model is supposed to have the same structure, size, mass distribution, and impact motion characteristics compared to human body. The crash test dummy is such a substitute for human body in crash tests. It is made of various materials such as steel, aluminum, rubber, and polymers and is equipped with multiple acceleration sensors, force sensors, torque sensors, and displacement sensors to record responses.

4. Mechanical Dummies

4.1. Development. In 1949, the first dummy was used in the air force; after years of development, the dummies have been widely used as substitutes for human body in car crash tests. According to the type used for collision, the dummies can be categorized as frontal impact dummy, side impact dummy, and rear impact dummy. Table 3 lists crash test dummy types and their application conditions. In order to better

TABLE 3: Dummies and their application areas.

Model name	Hybrid III	THOR-M	SID	SID-II's
Figure				
Application	Frontal impact	Frontal impact	Side impact	Side impact
Model name	BioSID	EuroSID-II	WorldSID	BioRID
Figure				
Application	Side impact	Side impact	Side impact	Rear impact

understand the development of mechanical dummies, the following describes in detail the development process of each series of dummy.

4.1.1. Frontal Impact Dummy. In 1971, ARL and Sierra collaborated to develop the Hybrid I dummy. This dummy can be used to measure head and chest triaxial acceleration and femur load. In 1972, with the support of the U.S. automotive giants, FTSS (First Technology Safety Systems) developed the Hybrid II dummy [15]. Many parts had been redesigned to achieve better results: the head/neck interface was more anatomical, the improved neck mount model facilitated the reproducibility of head kinematics, the self-centering shoulders and improved shoulder load distribution yielded more repeatable responses, and lower torso with butyl rubber lumbar spine improved overall repeatability. In general, its major improvements over Hybrid I dummy designs were good durability and acceptable repeatability. In 1973, ATD 502 dummy was developed. By improving the material and positioning structure, this dummy achieved a more human-like seating posture and a better repeatability. Although ATD 502 dummy had made a great progress, the biomechanical responses of various parts were still lacking. In 1976, General Motors (GM) made significant improvements in the neck, chest, and knees of Hybrid II and ATD 502 to develop Hybrid III dummy, whose biofidelity and injury prediction measurement capacity had been improved. Nowadays, the Hybrid III dummy has been widely used in

the field of car crash tests, including the 50th adult male dummy, the 95th adult male dummy, and the 5th adult female dummy. The Hybrid III 50th adult male dummy is currently the most widely used dummy in various countries. The Federal Motor Vehicle Safety Standard (FMVSS 208) clearly stipulates that the Hybrid III 50th dummy is designated as frontal impact dummy in car crash tests.

The THOR dummy program had been supported by National Highway Traffic Safety Administration (NHTSA) of the United States since last century. Currently, the improved THOR-M dummy has been qualified to enter the market and the Euro NCAP is considering using the THOR-M dummy for future frontal impact tests. Compared with the Hybrid III dummy, the THOR-M dummy has better damage prediction ability and has more human-like characteristics. For example, the THOR-M dummy has sensors mounted on the face to measure facial injuries in frontal crashes, while the Hybrid III dummy cannot predict such risks. Two wire spring dampers are added to the neck to simulate the head rotation lag. The flexibility of the neck is closer to human characteristics. In summary, the THOR-M dummy provides more body injury measurement data than the Hybrid III dummy and it will be widely used in the frontal impact test in the future.

4.1.2. Side Impact Dummy. In the late 1970s, the University of Michigan and the NHTSA jointly developed the world's first side impact dummy SID which was developed according to

50th American male [16, 17]. Its head and neck retained the structure in Hybrid II, and foam parts are used instead of the omitted arms in the torso. The chest of the SID cannot simulate the chest response of human for its material had no elasticity in the horizontal direction.

As SID dummy developing, Europe also launched the development work of the side impact dummy. During 1978–1982, three dummies produced by APR, ONSER, and MIRA were released, respectively [18]. Although these dummies cannot obtain the desired lateral impact response, they provided prototypes for the new side impact dummy EuroSID. The EuroSID-I was developed according to the European male size in the mid-1980s.

The SID and EuroSID were evaluated by the International Standards Organization (ISO) to be found without sufficient biofidelity [19]. In response to this conclusion, a biofidelic side impact dummy named BioSID was developed by General Motors and Society of Automotive Engineers (SAE) [20]. The head, neck, shoulders, chest, abdomen, and pelvis of the BioSID have good biofidelity in side collisions. SID-II was developed in 1995, representing a 5th small female. In 2000, EuroSID-II (ES-2) was developed and upgraded based on EuroSID-I; a lot of changes were made in the original structure, for example, a load sensor was added to the head-neck contact surface, reducing the coefficient of friction between the clavicle and the mounting plate, added a new backplane with load cell, and so on.

In 1997, the ISO initiated the development of a more biofidelic side impact dummy: the WorldSID dummy. WorldSID dummy was based on the medium size of men worldwide. The reproducibility, the durability, and the sensitivity have been greatly improved compared to other dummies.

4.1.3. Rear Impact Dummy. In the 1990s, a consortium consisted of Chalmers University, Volvo Car Corporation, and Saab Automobile AB was formed to develop the new dummy BioRID which was used in rear impact [21]. The BioRID dummy was designed to represent a 50th male in Europe, and its vertebral column curve fitted well with that of human. The vertebral column consisted of 24 separate vertebrae; the vertebral column will perform realistic movements when faced with impact load. Compared with Hybrid III dummy, BioRID dummy is more closely related to human characteristics on the neck and vertebrae [16]. Therefore, it is more realistic to simulate the human response after a rear-end collision in a rear collision accident.

It can be seen from the development of the dummies that all kinds of dummies have undergone continuous improvement, so that the response of each part of the dummy can be more and more close to the human body response. However, most of these dummies are designed based on the male size in Europe and America. But the size of the human body varies greatly from country to country. For example, the height and weight of 50th male in China were 167.8 cm and 59 kg (GB 10,000–1988), these values differ from those of Hybrid III (175.5 cm and 65.5 kg). Furthermore, the center position, moment of inertia, and radius of rotation of various parts of the human body are closely related to the height and weight of the human body. In this respect, the dummy may

have limited ability to predict the injury of people who are not European and American.

4.2. Validation. As the key equipment for vehicle collision safety inspection, the crash test dummy must not only be similar to the human structure in terms of external dimensions and mass distribution, but at the same time, the mechanical response of the major parts of the dummy should also be highly similar to the biological response of the same part of the human body. The higher the similarity is, the easier it is to get a more accurate injury assessment. Therefore, it is very important for the artificial simulation of dummy. In different collision conditions such as frontal impact, side impact, and rear impact, the major parts of the injured parts are not exactly the same, the forms of injury are different, and the method of verifying the biofidelity of the dummy is also different. According to the type of collision, the following introduces the validation of different dummies.

4.2.1. Frontal Impact Dummy. In the frontal impact, the most vulnerable parts of the body are the head, neck, chest, and knee. The Hybrid III is the most widely used frontal impact dummy around the world, and it has been done in various parts of rigorous tests to validate the biofidelity of dummy; Foster [15] detailed the validation process of the head, neck, chest, and knee. For head validation, the head was dropped from a position of 376 meters high to a flat rigid steel plate, three acceleration measurements were taken at the head center of gravity, and the acceleration directions were orthogonal to each other. The resultant of three accelerations was the final head response. For neck validation, biomechanical neck responses can be divided into response to flexion and extension tests. The whole dummy was restrained to conduct the sled tests, and the angle responses were obtained from high-speed motion pictures, while torque responses were measured by the dummy's neck load transducer. For chest validation, each dummy "sitted" on a flat surface with the upper and lower limbs and ribs parallel to the seating surface, a ballistic pendulum impactor weighing 4.3 kg struck at the center of the sternum with impact velocities 4.3 and 6.7 m/s. By multiplying the impactor mass and the deceleration, the chest impact force could be obtained. A potentiometer was used to measure the sternum relative to the thoracic spine, which was called chest deflection. For knee validation, each upper leg needed to be installed horizontally and there was an angle of 1.15 radians between the upper leg and lower leg; three pendulum impactors weighing 0.5 kg, 1.0 kg, and 1.5 kg were used to impact the knee along the axis of the femur, respectively, and the deceleration during the impact could be measured by axis accelerometer mounted on the impactor. Knee impact force was obtained from the product of pendulum mass and deceleration. The responses of the four parts of the validation were compared with the cadaver data obtained by Hubbard and McLeod [22], Mertz et al. [23], Neathery [24], and Horsch and Patrick [25], and the responses of the Hybrid III dummy were all distributed in the range of the cadaver data.

TABLE 4: ISO biofidelity classifications.

Level	Excellent	Good	Fair	Marginal	Unacceptable
Score range	>8.6 to 10.0	>6.5 to 8.6	>4.4 to 6.5	>2.6 to 4.4	0 to 2.6

TABLE 5: Side impact dummy biofidelity comparison.

	Head	Neck	Shoulder	Biofidelity rating			Overall
				Chest	Abdomen	Pelvis	
WorldSID	10	5.3	10	8.2	9.3	5.1	8
BioSID	6.7	6.7	7.3	6.3	3.8	4	5.7
EuroSID-I	5	7.8	7.3	5.4	0.9	1.5	4.4
ES-II	5	4.4	5.3	5.2	2.6	5.3	4.6

4.2.2. *Side Impact Dummy.* When the car is subjected to a side collision, the most vulnerable parts of the human body are the head, neck, shoulders, chest, abdomen, and pelvis, and each part needs to be validated. ISO had made a rating scale to evaluate the biofidelity of dummy as shown in Table 4. Scherer et al. [26] conducted tests according to ISO to judge the side dummies. For the head, neck, and chest validation, the test processes were similar to those of the frontal impact dummy, except that the experimental parameters were different, such as the head dropped from 200 meters instead of 376 meters, the sled used for neck validation changed to 6.9 and 5.8 m/s, and the impact direction of pendulum impactors changed. For the shoulders and pelvis, these parts are mainly affected by the blunt impact of the door; when the validation tests were conducted, rigid pendulum impactors were used to impact at certain velocities.

As can be seen from Table 5, all the side impact dummies have the acceptable biofidelity. The WorldSID performed well in many parts of biofidelity comparison, and the WorldSID is the only side impact dummy which can get “good” level from the overall performance. Most of the previous side impact tests used ES-II dummies. Now, WorldSID has become the side impact test dummy in U-NCAP, C-NCAP, and other regulations with its good biofidelity.

4.2.3. *Rear Impact Dummy.* The validation of the BioRID was conducted by comparing the responses with the PMHS data and volunteer data. Davidsson and Linder had contributed a lot to the validation in the early time; they carried out the validation tests at different impact velocities by different impact types. For example, Linder et al. [27] conducted sled tests to evaluate the BioRID. The sled used in the tests was generated by compressed air, and the acceleration pulse of sled was controllable. When compared with PMHS data, the dummy was exposed to a change of velocity (Δv) of 10 and 15 km/h, while compared with volunteer data, the dummy was subjected to a maximum acceleration of $3.5g$ at Δv of 10 km/h. In horizontal accelerations and displacements of the head and the chest, the neck forces were chosen as the comparison indicators. The responses of BioRID correlated well with the volunteer and PMHS data, which indicated that the BioRID can be used as a sensitive tool for rear impact.

The neck is most vulnerable to injury when the rear-end impact occurs; some researchers focused on this part. Ono and Kaneoka [28], Davidsson et al. [29], and Geigl et al. [30] used volunteer tests to obtain data on human neck injuries in rear-end impacts. Foret-Bruno et al. [31] analyzed the injury status and the form of motion of the head and neck and the corresponding parts of the back of the Hybrid III dummy in the postimpact mode. The conclusion is that the stiffness of the neck of the Hybrid III dummy is quite different from that of the human body.

From these experimental results, the existing dummy model currently used anthropomorphic crash test dummies that can reflect the human response to a certain extent, but they are limited in their biofidelity and in their application type. Further improvement research on existing physical dummy is necessary.

5. Computational Models

Nowadays, commercial mechanical dummies are expensive and consume huge during crash tests. Only large corporations and research institutes have the financial resources to purchase physical dummies for research on car crash safety. With the continuous advancement of computer technology and digitization methods, visual model in computer is also widely used in automotive crash simulation. Currently, the models used for car crash studies mainly include multirigid models and finite element models. Multirigid body models are based on multibody dynamics theory. Engineers use simple planes and ellipsoids to simulate various structures of the human body and construct adult body model, using ADAMS, MADYMO, and other software to analyze. The finite element model uses the principle of finite element method to build the model. The essence of the finite element method is to discretize the entire study object. In contrast, the finite element model is more detailed so that it can investigate the local deformation and stress distribution. Therefore, the application of the finite element model is more extensive.

5.1. *Traditional FE Models.* The study of finite element dummy for car crash originated in the late 1970s. Some companies have developed recognized FE dummy models, such

as ERAB, ETA, FTSS, ARUP, and FAT [32]. Based on the mechanical dummies mentioned above, the FE model of dummies can be developed by five steps [33]. Firstly, capture the geometries of mechanical dummies by 3D scan. Secondly, translate the obtained geometries to CAD data. Thirdly, represent the model with 3D elements that means generating the FEM meshes. Fourthly, develop single components. Lastly, validate the model; the validation process is consistent with that of the mechanical dummy. Recent advancements in computer hardware technology and software developments have made it possible to develop detailed finite element models, by increasing the model structural details, refining mesh density, and improving material properties to improve the calculation accuracy of FE model. Nowadays, the commercial mechanical dummies all have a finite element dummy corresponding to them; the most recognized FE models are developed by FTSS.

Many scholars also have validated the finite element dummies by comparing with physical tests or regulations. In 2002, Nouredine et al. [34] illustrated the construction and validation of the Hybrid III dummy FE model in detail. The simulation results of chest model, head model, and neck model were compared with the mechanical dummy tests according to the Code of Federal Regulations. The time histories of the chest acceleration and head acceleration showed reasonable agreement with the results of physical test. In 2007, Friedman et al. [35] performed a head drop test using a Hybrid III finite element dummy to compare the upper neck force with the test in published mechanical dummy test. The results demonstrated that FE model shows good agreement with the test response in a rollover crash environment. In 2013, Tanaka et al. [36] studied the relationship between external force to shoulder and chest injury using WorldSID FE model. According to the seating posture and impact position of the manual to perform the CAE, there was a good agreement between CAE simulation results and physical test results. In 2017, the FE model of 5th percentile THOR had been compared with biofidelity corridors from head to toe [37]. The peak thorax probe impact response can be consistent with that of biofidelity corridors.

5.2. Human Models. Since the 1990s, in order to study human injuries in more detail, scholars have begun to explore the biofidelic human models gradually. The human model is developed based on the human body's geometric dimensions and anthropomorphic material properties. It can predict human injuries such as skeletal fractures, internal organ injuries, stress distribution of brain tissue, and skin contusion. There are several available whole-body human models, including H-model [16], Ford human body model [38], WSU human model, HUMOS, THUMS, and GHBM model. The latter four models are relatively widely used. The development of them is described, respectively, as follows.

In the past 20 years, Wayne State University (WSU) Bioengineering Center has been devoted to the development of finite element models as shown in Figure 1. Since 1993, a skull-brain FE model of the human which is called the WSU-BIM model was developed. The initial version of the WSU-BIM model was designed to simulate the basic anatomy of



FIGURE 1: WSU model [46].

the human head (including the scalp, cerebral spinal fluid, dura, parasagittal bridging, venous sinuses, three-layered skull, gray matter, white matter, cerebellum, falx, pia matter, tentorium, brain stem, and ventricles) and facilitate further study of head injury mechanisms [39]; the model was able to predict the sensitivity of the brain to the effects of impact from different directions and the location of diffuse axonal injury (DAI) in the brain. In addition, a sliding interface was added to the model to simulate the interaction between the matter and cerebral spinal fluid [40]. With the sliding interface introduced, the model was capable of predicting the relative displacement time histories of the brain. The response data could be matched with pressure and contact force data by Nahum [41]. Based on the previous work, a more detailed WSUBIM model was developed. The density of the mesh had been further improved, and the number of model elements rose from 41,354 to 314,500, when nodes increased from 32,898 to 281,800 [42]. The new detailed model has the ability to simulate at high rotational acceleration conditions up to $12,000 \text{ rad/s}^2$ and has been validated against published cadaveric test data [41]. WSU also studied the other advanced models involving the human chest [43], neck [44], and abdomen [45], and their validation is confirmed by experiments conducted at the experimental center of WSU. The WSU human models have served many workers and institutions as a basis for their own development and research (Ford, General Motors, Nissan, Toyota, ESI, Mecalog, etc.).

At the beginning of the 21st century, Toyota Motor Corporation developed a new type of total body finite element dummy called THUMS [47]. According to the data obtained by Schneider et al. [48], the THUMS was first scaled to fit the 50th percentile of American male which consists of a base model and several detailed models (head/face, shoulder, and internal organs). The base model totally includes 60,000 nodes, 1000 materials, and 83,500 elements; solid elements were used to represent the spongy bone while the cortical bone was modeled using shell elements; there was

a ligament connection between the bones, and sliding interfaces were defined in the contact area; the whole model had no mechanical joint [49]. Several simulations were performed to compare with the data of cadaveric test to validate impact responses of each body part [50, 51]. The model was used in injury reconstruction and successfully reproduced multiple injuries of an occupant, such as bone fractures and ligament ruptures, but the internal organs in this model were fused to form continuum bodied with homogeneous material properties, which means that the internal organs are not modeled individually. In order to extend the predictable range of the model, the research team refines the brain and internal organs structure for these issues [52]. The THUMS Ver.2.0 model had individual internal organs which include the bronchus, trachea, lung, heart, diaphragm, kidney, aorta, vena cava, spleen, esophagus, lung, stomach, pancreas, intestine, liver, and duodenum. These individual organs constituted the respiratory system, circulatory system, and digestive system. As for the brain model, a 2D head/brain model was developed, and they concluded that modeling of sulci of the cerebrum can affect the prediction of occurrence of brain injury. Then in 2007, THUMS Ver.3.0 model with a 3D brain consisting of the skull, brain, and skin was developed; the white matter, grey matter, cerebral spinal fluid (CSF), cerebellum, and cerebrum were included. The head/brain model was validated against three series of test data, in which translational and rotational accelerations were applied to the center of gravity (CG) of the head [53]. Then in 2012, the THUMS Ver.3.0 was mainly improved in the following aspects [54]: the model added some detailed parts, such as internal organs and the long bone in the lower extremities. In addition, the muscles had been added in the whole body, even in the sophisticated parts such as shoulder, chest, and lumbar spines. Moreover, the gap between the skull and the brain was eliminated at the base of the skull to more accurately represent the anatomy of the head and brain. These features had been verified by comparing the response with cadaveric and volunteer tests data from previous reference [55–57]. The updated THUMS with a vehicle sled model was used to investigate that the muscle activation levels and the activation timings had a nonnegligible effect on the driver's kinematics and injury outcomes. The updated THUMS is a promising tool to be used in accident injury reconstruction. In order to meet the need of real-world automotive accidents prediction, factors including body sizes, ages, and genders are considered by the research team. Therefore, a small 5th percentile female THUMS model [58] and a 6-year-old child THUMS [59] were developed successively as shown in Figure 2.

Since 1999, HUMOS (shown in Figure 3) was launched and funded by the European Commission in the Industrial and Materials Technologies (IMT) program (Brite-EuRam III), and the LAB (Laboratory of Accidentology and Biomechanics PSA Peugeot Citroën Renault) was involved in shoulder and the thorax meshing process [60]. Aiming at developing an exquisite human model that could be widely accepted by the crashworthiness community, the geometry acquisition is the basis of the task. By slicing a frozen cadaver, 491 images including detailed information of a

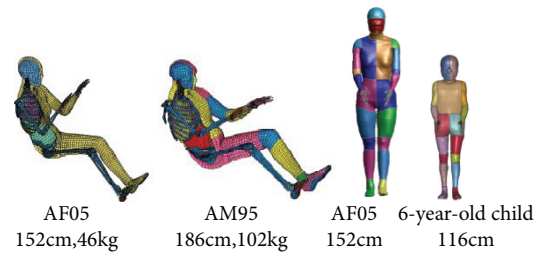


FIGURE 2: THUMS models [53].



FIGURE 3: HUMOS model [66].

50th percentile European male were obtained. After the process of 3D geometrical reconstruction and meshing, the segment of the model had been validated by comparing the results to reference [13, 61–63]. Then further investigation on how muscular tensing influences the body response had been conducted by volunteer experiment [63]. HUMOS model had been validated having the ability to predict cervical trauma and other type trauma as well [64]. The human body was modified to study the relationship between chest deformation and the number of rib fractures. However, the results show that the maximum peak strain of the ribs does not correctly predict the number of rib fractures [65, 66].

Committed to creating the world's most biofidelic computational human body model, the Global Human Body Models Consortium (GHBMCM) developed a full-body CAD model of 50th percentile male model, which was called the GHBMCM model (as shown in Figure 4). Gayzik et al. [67, 68] described the human data acquisition and model building process of a living 26-year-old male occupant (174.9 cm, 78.6 kg, BMI: 25.7) in detail. Seventy-two scans were performed using three medical imaging modalities



FIGURE 4: GHBMC model [68].

(CT, MRI, and upright MRI); more than 300 individual components like bones (without thin cortical bone structures), organs (head, thorax, abdomen, etc.), vessels (without thin-wall vessels), muscles, cartilage, fibrocartilage, ligament, and tendon (without tissues) were generated through segmentation to represent the human anatomy. The model was validated from the component level, including the abdomen [69], cervical spine [70, 71], foot and ankle [72], and head [73]. And then whole-body validation had been conducted, under far-side conditions, Katagiri et al. [74] verified that the whole-body response of the GHBMC model had kinematic behavior sensitivity compared to six PMHS tests data [75], involving several parts such as the shoulder, head, pelvis, and abdomen. Under lateral sled and lateral drop conditions, Vavalle et al. [76] evaluated the whole-body response of the GHBMC model in thorax, abdomen, and pelvis regions and found that thorax and abdomen regions showed a good biofidelity. Park et al. [77] compared impact forces and kinematics data of GHBMC to that of PMHS obtained by Shaw et al. [78] at an impact velocity of 4.3 ± 0.1 m/s and assessed the biofidelity of GHBMC through correlation analysis. From the results, it can be concluded that the shoulder of the GHBMC model has a poor correlation with the PMHS, which means that the shoulder area needs to be improved. In order to improve the shoulder region, two modifications about material property of shoulder-related muscles and adipose tissue and three kinds of improvements on modeling technology were introduced into the repositioned model by Park et al. [79]; the sensitivity analysis showed that these modifications significantly influence the response and the shoulder region of modified model showed a better biofidelity. The research also indicated that the appropriate initial posture of the model contributes to fewer errors of peak shoulder deflection. Other researcher also realized the importance of initial posture on model biofidelity, and some research on repositioning were conducted. Marathe et al. [80] proposed a spline-based technique to locate the sagittal plane of human model; based on this research, different cubic

splines are provided at the cervical, thoracic, and lumbar spine of GHBMC model by Chhabra [81], and the shape can be better controlled to predict the flexion, abduction, and twisting of human body by moving the control points. Chawla et al. [82] applied contour-based deformation technique to lower limbs (including ankle joint, knee joint, and hip joint) of the GHBMC model. Nonintersecting contours outline important skeleton; Delaunay triangulation method was then used to divide a three-dimensional space into small tetrahedrons, and the last step involves contour transformation based on the desired input, and it is expected that the key points can be transformed using the same parameters. This technology can greatly increase computational efficiency and ensure the calculation accuracy at the same time. The above studies are almost about the 50th percentile male model; in fact, establishing 5th percentile female GHBMC model was also listed as part of the project; the process of medical imaging dataset acquisition and the CAD model establishment was the same as that of the male model. The initial version of 5th percentile female had been established [83], but more validation work is needed in the future study.

It can be seen from the development of these human models that models are developing in the direction of gradual complication and anthropomorphization. However, with the refinement of the model mesh and the increase of the cells, the calculation time became longer and longer. Moreover, almost all of the existing human models are designed based on European and American men, which has limitation to predict the car crash injury for people of different genders, different countries, and different physical characteristics.

6. Conclusion

In this article, the development and verification process of mechanical dummies, related finite element models, and human models developed based on injury biomechanics are introduced in detail. From the description above, it can be seen that

- (1) the existing commercial crash test dummies are based on the human characteristics of Europe and the United States. From the perspective of injury mechanisms, they cannot represent the general human characteristics of other countries. In order to better protect the safety of occupants and improve the accuracy of injury prediction, each country should work hard to develop a crash test dummy that meets the human characteristics of its national conditions
- (2) most of the existing dummies and models are based on the male body. However, in the real collision, the elderly, obese, and dwarf women are more vulnerable to injury. In the subsequent model establishment, the diversity of people's type, size, and age can be taken into consideration

Conflicts of Interest

The authors declare no conflicts of interest.

Acknowledgments

The authors would like to acknowledge the National Natural Science Funds for Distinguished Young Scholar (Grant no. 51505181), the China Postdoctoral Science Foundation funded project (no. 2016M590256), the Advanced Manufacturing Project of Provincial School Construction of Jilin Province (no. SXGJSF2017-2), and the Science & Technological Project of Smart Manufacturing in Tianjin supported by the Tianjin Science and Technology Commission (no. 16ZZXNGX00100).

References

- [1] World Health Organization, *World Road Safety Global Status Report on Road Safety*, 2015.
- [2] National Bureau of Statistics of China, 2015, [EB/OL] <http://data.stats.gov.cn/index.htm>.
- [3] D. C. Viano, A. I. King, J. W. Melvin, and K. Weber, "Injury biomechanics research: an essential element in the prevention of trauma," *Journal of Biomechanics*, vol. 22, no. 5, pp. 403–417, 1989.
- [4] E. Hertz, "A note on the head injury criterion (HIC) as a predictor of the risk of skull fracture," in *Association for the Advancement of Automotive Medicine. 37th Annual Conference. Proceedings*, pp. 303–312, Des Plaines, IL, USA, 1993.
- [5] M. Kleinberger, E. Sun, and R. Eppinger, "Development of improved injury criteria for the assessment of advanced automotive restraint systems II," *National Highway Traffic Safety Administration*, vol. 54, no. 8, pp. 151–152, 1999.
- [6] K. Bohman, O. Boström, Y. Land, and A. Kullgren, "A study of AIS1 neck injury parameters in 168 frontal collisions using a restrained hybrid III dummy," *Stapp Car Crash Journal*, vol. 44, pp. 103–116, 2000.
- [7] J. P. M. Stapp, "Human exposure to linear decelerations," in *Part 2: The Forward Facing Position and the Development of a Crash Harness*, Wright-Patterson Air Force Base, Aero Medical Laboratory, Wright Air Development Center, Ohio, 1951.
- [8] E. Moffatt, B. Hare, R. Hughes, and L. Lewis, "Head excursion of restrained human volunteers and Hybrid III dummies in steady state rollover tests," *Annual Proceedings of Association for the Advancement of Automotive Medicine*, vol. 47, pp. 445–465, 2003.
- [9] K. Ono, S. Inami, K. Kaneoka et al., "Relationship between localized spine deformation and cervical vertebral motions for low speed rear impacts using human volunteers," in *Proceedings of the 1999 International IRCOBI Conference on the Biomechanics of Impact*, Sitges, Spain, 1999.
- [10] K. Ono, A. Kikuchi, M. Nakamura, H. Kobayashi, and N. Nakamura, "Human head tolerance to sagittal impact reliable estimation deduced from experimental head injury using subhuman primates and human cadaver skulls," SAE Technical Paper 801303, 1980.
- [11] C. K. Kroell, M. E. Pope, D. C. Viano, C. Y. Warner, and S. D. Allen, "Interrelationship of velocity and chest compression in blunt thoracic impact to swine," SAE Technical Paper 811016, 1981.
- [12] V. R. Hodgson and L. M. Patrick, "Dynamic response of the human cadaver head compared to a simple mathematical model," SAE Technical Paper 680784, 1968.
- [13] C. K. Kroell, D. C. Schneider, and A. M. Nahum, "Impact tolerance and response of the human thorax," SAE Technical Paper 710851, 1971.
- [14] C. K. Kroell, D. C. Schneider, and A. M. Nahum, "Impact tolerance and response of the human thorax," SAE Technical Paper No. 741187, 1971.
- [15] J. Foster, "Hybrid III-a biomechanically-based crash test dummy," SAE Technical Paper 770938, 1977.
- [16] E. Haug, H. Y. Choi, S. Robin, and M. Beaugonin, "Human models for crash and impact simulation," *Handbook of Numerical Analysis*, vol. 12, pp. 231–452, 2004.
- [17] F. Li and C. Li, "Analysis on application of vehicle side impact dummy," *Automotive Technology*, vol. 5, pp. 21–24, 2007.
- [18] E. G. Janssen and A. C. M. C. Vermissen, "Biofidelity of the European Side Impact Dummy–EUROSID," SAE Technical Paper 881716, 1988.
- [19] A. L. Irwin, L. A. Pricopio, H. J. Mertz, J. S. Balser, and W. M. Wkoreff, "Comparison of the EuroSID and SID impact responses to the response corridors of the International Standards Organization," Society of Automotive Engineers. Paper no. 890604, 1989.
- [20] M. S. Beebe, "What is BioSID?," Society of Automotive Engineers. Technical Paper no. 900377, 1990.
- [21] A. Linder and C. Svensson, "MY BioRID, a crash test dummy for rear impact: a review of development, validation and evaluation," in *Road Safety Research, Policing and Education Conference*, Brisbane, Queensland, Australia, 2000.
- [22] R. P. Hubbard and D. G. Mcleod, "Definition and development of a crash dummy head," SAE Technical Paper 741193, 1974.
- [23] H. J. Mertz, R. F. Neathery, and C. C. M. Culver, "Performance requirements and characteristics of mechanical necks," in *Human Impact Response*, 1973.
- [24] R. F. Neathery, "Analysis of chest impact response data and scaled performance recommendations," in *Proceedings of the Eighteenth Stapp Car Crash Conference*, Ann Arbor, MI, USA, 1974 Society of Automotive Engineers.
- [25] J. D. Horsch and L. M. Patrick, "Cadaver and dummy knee impact response," SAE Technical Paper 760799, 1976.
- [26] R. Scherer, K. Bortenschlager, A. Akiyama, S. Tylko, M. Hartlieb, and T. Harigae, "WorldSID production dummy biomechanical responses," *International Journal of Gynecology & Obstetrics*, vol. 107, Supplement 2, article S429, 2009.
- [27] A. Linder, P. Lövsund, and H. Steffan, "Validation of the BioRID P3 against volunteers and PMHS data and comparison to the Hybrid III in low-velocity rear-end impacts," in *The 43rd Annual Proceedings / Association for the Advancement of Automotive Medicine*, pp. 367–381, Barcelona, Spain, 1999.
- [28] K. Ono and K. Kaneoka, "Motion analysis of human cervical vertebrae during low speed rear impacts by the simulated sled," in *Proceedings of IRCOBI International Conference on the Biomechanics of Impacts*, pp. 223–237, Hannover, Germany, 1997.
- [29] J. Davidsson, P. Lövsund, K. Ono, and C. Svensson, "A comparison between volunteer, BioRID P3 and Hybrid III performance in rear-end sled collisions impacts," in *Proceedings of the International Research Council on the Biomechanics of Injury conference*, Barcelona, Spain, 1999.
- [30] B. C. Geigl, H. Steffan, C. Dippel, M. H. Muser, F. Waltz, and C. Svensson, "Comparison of head-neck kinematics during rear end impact between standard Hybrid III, RID neck, volunteers and PMTO's," in *Proceedings of the International*

- Research Council on the Biomechanics of Injury conference*, pp. 261–270, Brunnen, Switzerland, 1995.
- [31] J. Y. Foret-Bruno, F. Dauvilliers, C. Tarriere, and P. Mark, “Influence of the seat and head rest stiffness on the risk of cervical injuries in rear impact,” in *Proceeding of the 13th International Technical Conference on Experimental Safety Vehicles*, pp. 968–974, Paris, France, November 1991.
- [32] X. Qiu and S. L. Huang, “Application of nonlinear finite element simulation technology in passive safety research of automobiles,” vol. 2, pp. 15–19, 1998.
- [33] A. Rieser, C. Nussbaumer, A. Eichberger, and H. Steffan, “A development process for creating finite-element models of crash test dummies based on investigations of the hardware,” in *Proceedings of the 21st (Esv) International Technical Conference on the Enhanced Safety of Vehicles*, Stuttgart, Germany, 2009.
- [34] A. Noureddine, A. Eskandarian, and K. Digges, “Computer modeling and validation of a hybrid III dummy for crashworthiness simulation,” *Mathematical and Computer Modelling*, vol. 35, no. 7-8, pp. 885–893, 2002.
- [35] K. Friedman, J. Hutchinson, and D. Mihora, “Finite element modeling of rollover crash tests with Hybrid III dummies,” in *ASME 2007 Summer Bioengineering Conference*, pp. 846–852, Keystone, CO, USA, 2007.
- [36] S. Tanaka, S. Hayashi, S. Fukushima, and T. Yasuki, “Investigation of a relationship between external force to shoulder and chest injury of WorldSID and THUMS in 32 km/h oblique pole side impact,” *Traffic Injury Prevention*, vol. 14, Supplement 1, pp. S64–S76, 2013.
- [37] A. Lakshminarayana and C. S. Shah, “Development of the THOR-5F advanced frontal small female dummy FE model,” in *Proceedings of IRCOBI Conference*, Antwerp, Belgium, 2017.
- [38] R. E. El-Jawahri, T. R. Laituri, J. S. Ruan, S. W. Rouhana, and S. D. Barbat, “Development and validation of age-dependent FE human models of a mid-sized male thorax,” *Stapp Car Crash Journal*, vol. 54, pp. 407–430, 2010.
- [39] J. S. Ruan, T. B. Khalil, A. I. King, and C., “Finite element modeling of direct head impact,” in *37th Stapp Car Crash Conference Proceedings*, San Antonio, Texas, USA, 1993.
- [40] A. S. Al-Bsharat, W. N. Hardy, K. H. Yang, T. B. Khalil, S. Tashman, and A. I. King, “Brain/skull relative displacement magnitude due to blunt head impact: new experimental data and model,” SAE Technical Paper, 1999.
- [41] A. M. Nahum, “Intracranial pressure dynamics during head impact,” SAE Technical Paper 770922, 1977.
- [42] L. Zhang, K. H. Yang, R. Dwarampudi et al., “Recent advances in brain injury research: a new human head model development and validation,” *Stapp Car Crash Journal*, vol. 45, p. 369, 2001.
- [43] C. S. Shah, K. H. Yang, W. Hardy, H. K. Wang, and A. I. King, “Development of a computer model to predict aortic rupture due to impact loading,” *Stapp Car Crash Journal*, vol. 45, no. 45, p. 161, 2001.
- [44] J. Yang, *Bibliographic Study on Biomaterial Characterisation*, 1998.
- [45] J. B. Lee and K. H. Yang, “Development of a finite element model of the human abdomen,” *Stapp Car Crash Journal*, vol. 45, no. 45, pp. 79–100, 2001.
- [46] J. W. Hu, J. D. Rupp, and M. P. Reed, “Focusing on vulnerable populations in crashes: recent advances in finite element human models for injury biomechanics research,” *Journal of Automotive Safety & Energy*, vol. 3, pp. 295–307, 2012.
- [47] M. Iwamoto, Y. Kisanuki, I. Watanabe, K. Furusu, and K. Miki, “Development of a finite element model of the total human model for safety (thums) and application to injury reconstruction,” in *Proceedings of the International IRCOBI conference*, Munich, Germany, 2002.
- [48] L. W. Schneider, D. H. Robbins, M. A. Pflug, and R. G. Snyder, *Anthropometry of Motor Vehicle Occupants, Vol. 2*, UMTRI-83-53-2, NHTSA, 1983.
- [49] F. Oshita, K. Omori, Y. Nakahira, and K. Miki, “Development of a finite element model of the human body,” in *7th International LS-DYNA Users Conference*, pp. 3–37, Detroit, MI, USA, 2002.
- [50] K. Furusu, I. Watanabe, C. Kato, K. Miki, and J. Hasegawa, “Fundamental study of side impact analysis using the finite element model of the human thorax,” *JSAE Review*, vol. 22, no. 2, pp. 195–199, 2001.
- [51] A. Tamura, K. Furusu, M. Iwamoto, C. Kato, K. Miki, and J. Hasegawa, “Development of a finite element model of the human lower extremity for assessing automotive crash injury potential,” in *Human Biomechanics and Injury Prevention*, 2000.
- [52] M. Iwamoto, K. Omori, H. Kimpara et al., “Recent advances in THUMS: development of individual internal organs, brain, small female and pedestrian model,” in *Proceedings of 4th European LS Dyna Users conference*, pp. 1–10, Ulm, Germany, 2003.
- [53] M. Iwamoto, Y. Nakahira, A. Tamura, H. Kimpara, I. Watanabe, and K. Miki, “Development of advanced human models in THUMS,” in *Development of advanced human models in THUMSLS-DYNA Users’ Conference*, Gothenburg, Sweden, May 2007.
- [54] M. Iwamoto, Y. Nakahira, H. Kimpara, T. Sugiyama, and K. Min, “Development of a human body finite element model with multiple muscles and their controller for estimating occupant motions and impact responses in frontal crash situations,” SAE Technical Paper, 2012.
- [55] D. E. Anderson, M. L. Madigan, and M. A. Nussbaum, “Maximum voluntary joint torque as a function of joint angle and angular velocity: model development and application to the lower limb,” *Journal of Biomechanics*, vol. 40, no. 14, pp. 3105–3113, 2007.
- [56] A. B. Schultz, D. N. Warwick, M. H. Berkson, and A. L. Nachemson, “Mechanical properties of human lumbar spine motion segments—part I: responses in flexion, extension, lateral bending, and torsion,” *Journal of Biomechanical Engineering*, vol. 101, no. 1, pp. 46–52, 1979.
- [57] H. Yamada, *Strength of Biological Materials*, The Williams & Wilkins Company, Baltimore, MD, 1970.
- [58] H. Kimpara, M. Iwamoto, and K. Miki, “Development of a small female FEM model,” in *Proceedings of JSAE Spring Congressno. 2002*, pp. 1–4, Japan, 2002, (No. 59-02).
- [59] K. Furukawa, K. Furusu, and K. Miki, “A development of child FEM model: part I: skeletal model of six-year-old child,” in *The Proceedings of the JSME Annual Meeting*, pp. 89–90, Japan, 2002.
- [60] S. Robin, “HUMOS: human model for safety—a joint effort towards the development of refined human-like car occupant models,” in *17th international technical conference on the enhanced safety vehicle*, Amsterdam, Netherlands, 2001.

- [61] E. Lizée, S. Robin, E. Song et al., "Development of a 3D finite element model of the human body," SAE Technical Paper 983152, 1998.
- [62] E. Lizée, E. Song, S. Robin, and J. Y. Le Coz, "Finite element model of the human thorax validated in frontal, oblique and lateral impacts: a tool to evaluate new restraint systems," in *International IRCOBI Conference on the Biomechanics of Impact*, Göteborg, Sweden, 1998.
- [63] P. Vezin and J. P. Verriest, "Development of a set of numerical human models for safety models for safety," in *19th International Technical Conference on the Enhanced Safety of Vehicles*, Washington, DC, USA, 2005.
- [64] P. Tropiano, L. Thollon, P. J. Arnoux et al., "Using a finite element model to evaluate human injuries application to the HUMOS model in whiplash situation," *Spine*, vol. 29, no. 16, pp. 1709–16, 2004.
- [65] E. Song, X. Trosseille, and P. Baudrit, "Evaluation of thoracic deflection as an injury criterion for side impact using a finite elements thorax model," *Stapp Car Crash Journal*, vol. 53, no. 53, pp. 155–191, 2009.
- [66] E. Song, E. Lecuyer, and X. Trosseille, *Development of Injury Criteria for Frontal Impact Using a Human Body FE Model*, 2011.
- [67] F. S. Gayzik, D. P. Moreno, C. P. Geer, S. D. Wuertzer, R. S. Martin, and J. D. Stitzel, "Development of a full body CAD dataset for computational modeling: a multi-modality approach," *Annals of Biomedical Engineering*, vol. 39, no. 10, pp. 2568–2583, 2011.
- [68] S. Gayzik, D. P. Moreno, N. A. Vavalle, A. C. Rhyne, and J. D. Stitzel, "Development of full human body finite element model for blunt injury prediction utilizing a multi-modality medical imaging protocol," in *12th International LS-DYNA User Conference*, Dearborn, MI, 2012.
- [69] P. Beillas and F. Berthet, "Performance of a 50th percentile abdominal model for impact: effects of size and mass," *Journal of Biomechanics*, vol. 45, p. S83, 2012.
- [70] J. A. Dewit and D. S. Cronin, "Cervical spine segment finite element model for traumatic injury prediction," *Journal of the Mechanical Behavior of Biomedical Materials*, vol. 10, no. 10, pp. 138–150, 2012.
- [71] J. B. Fice, D. S. Cronin, and M. B. Panzer, "Cervical spine model to predict capsular ligament response in rear impact," *Annals of Biomedical Engineering*, vol. 39, no. 8, pp. 2152–2162, 2011.
- [72] J. Shin, N. Yue, and C. D. Untaroiu, "A finite element model of the foot and ankle for automotive impact applications," *Annals of Biomedical Engineering*, vol. 40, no. 12, pp. 2519–2531, 2012.
- [73] H. Mao, L. Zhang, B. Jiang et al., "Recent advances in developing finite element head model," in *International Crashworthiness Conference*, pp. 18–20, Milano, Italy, 2012.
- [74] M. Katagiri, J. Zhao, J. Kerrigan, R. Kent, and J. Forman, "Comparison of whole-body kinematic behaviour of the GHBMOC occupant model to PMHS in far-side sled tests," in *Proceedings of IRCOBI Conference*, pp. 679–693, Malaga, Spain, 2016.
- [75] J. L. Forman, F. Lopezvaldes, D. J. Lessley et al., "Occupant kinematics and shoulder belt retention in far-side lateral and oblique collisions: a parametric study," *Stapp Car Crash Journal*, vol. 57, pp. 343–385, 2013.
- [76] N. A. Vavalle, D. P. Moreno, A. C. Rhyne, J. D. Stitzel, and F. S. Gayzik, "Lateral impact validation of a geometrically accurate full body finite element model for blunt injury prediction," *Annals of Biomedical Engineering*, vol. 41, no. 3, pp. 497–512, 2013.
- [77] G. Park, T. Kim, J. R. Crandall, C. Arregui Dalmases, and B. J. Luzón Narro, "Comparison of kinematics of GHBMOC to PMHS on the side impact condition," in *2013 IRCOBI Conference Proceedings*, pp. 368–379, Gothenburg, 2013.
- [78] G. Shaw, D. J. Lessley, J. L. Ash et al., "Side impact PMHS thoracic response with large-volume air bag," *Traffic Injury Prevention*, vol. 15, no. 1, pp. 40–47, 2014.
- [79] G. Park, T. Kim, M. B. Panzer, and J. R. Crandall, "Validation of shoulder response of human body finite-element model (GHBMOC) under whole body lateral impact condition," *Annals of Biomedical Engineering*, vol. 44, no. 8, pp. 2558–2576, 2016.
- [80] R. S. Marathe, A. Chawla, S. Mukherjee, and R. Malhotra, "Predicting thoracic spinal postures in finite element model with Bezier technique," in *Proceedings of the International Research Council on the Biomechanics of Injury conference*, pp. 224–227, Krakow, Poland, 2011, International Research Council on Biomechanics of Injury.
- [81] A. Chhabra, "Spline-based repositioning for the vertebral column of the GHBMOC human body finite element model," in *Proceedings of IRCOBI Conference*, Antwerp, Belgium, 2017.
- [82] A. Chawla, S. Singh, S. Paruchuri, and A. Chhabra, "Contour based repositioning of specific joints of the GHBMOC human body FE model," Symposium on International Automotive Technical Paper 2017-26-0265, 2017.
- [83] M. L. Davis, B. Koya, J. D. Stitzel, and F. S. Gayzik, "Development of the GHBMOC 5th percentile female finite element model," in *2015 Ohio State University Injury Biomechanics Symposium*, Columbus, OH, USA, 2015.

Research Article

Biomechanical Responses and Injury Characteristics of Knee Joints under Longitudinal Impacts of Different Velocities

Yan Xiong,¹ Xueliang Zhao,¹ Hongyi Xiang,² Yunjiao Wang,¹ Zhikang Liao,² Xiyan Zhu,² and Hui Zhao ²

¹Department of Orthopedics, Daping Hospital and the Research Institute of Surgery, Third Military Medical University, Chongqing 400042, China

²Institute for Traffic Medicine, State Key Laboratory of Trauma, Burns & Combined Wound, Third Military Medical University, Chongqing 400042, China

Correspondence should be addressed to Hui Zhao; box.zhaohui@163.com

Received 7 March 2018; Accepted 6 June 2018; Published 5 August 2018

Academic Editor: Tatsuo Yoshino

Copyright © 2018 Yan Xiong et al. This is an open access article distributed under the Creative Commons Attribution License, which permits unrestricted use, distribution, and reproduction in any medium, provided the original work is properly cited.

Background and Objective. Knee joint collision injuries occur frequently in military and civilian scenarios, but there are few studies assessing longitudinal impacts on knee joints. In this study, the mechanical responses and damage characteristics of knee longitudinal collisions were investigated by finite element analysis and human knee impact tests. **Materials and methods.** Based on a biocollision test plateau, longitudinal impact experiments were performed on 4 human knee joints (2 in the left knee and 2 in the right knee) to measure the impact force and stress response of the bone. And then a finite element model of knee joint was established from the Chinese Visible Human (CVH), with which longitudinal impacts to the knee joint were simulated, in which the stress response was determined. The injury response of the knee joint-sustained longitudinal impacts was analyzed from both the experimental model and finite element analysis. **Results.** The impact experiments and finite element simulation found that low-speed impact mainly led to medial injuries and high-speed impact led to both medial and lateral injuries. In the knee joint impact experiment, the peak flexion angles were $13.8^\circ \pm 1.2$, $30.2^\circ \pm 5.1$, and $92.9^\circ \pm 5.45$ and the angular velocities were 344.2 ± 30.8 rad/s, 1510.8 ± 252.5 rad/s, and 9290 ± 545 rad/s at impact velocities 2.5 km/h, 5 km/h, and 8 km/h, respectively. When the impact velocity was 8 km/h, 1 knee had a femoral condylar fracture and 3 knees had medial tibial plateau fractures or collapse fractures. The finite element simulation of knee joints found that medial cortical bone stress appeared earlier than the lateral peak and that the medial bone stress concentration was more obvious when the knee was longitudinally impacted. **Conclusion.** Both the experiment and FE model confirmed that the biomechanical characteristics of the injured femur and medial tibia are likely to be damaged in a longitudinal impact, which is of great significance for the prevention and treatment of longitudinal impact injuries of the knee joint.

1. Introduction

Knee joint injuries are commonly caused by traffic accidents, sports medicine, and falling from high altitudes [1–3]. As the main weight-bearing joint of the human lower extremities, the knee joint is characterized by various activities and complex anatomical and mechanical structures, and the mechanisms and biomechanical responses of the knee joint to injuries have been popular research topics [4–7]. A large number of experimental studies have been conducted worldwide studying injury mechanisms [8–10]. A recently

published clinical study suggests that a single fracture-free blunt trauma will thicken the subchondral bone after injury [11], which is followed by chronic osteoarthritis [12]. Currently, biomechanical studies concerning the knee joint are mainly carried out by performing impact tests in cadavers and studying knee fractures [13]. From impact tests with different bending angles of the knee joint, it was concluded that increases in the bending angle lead to increases in the fracture load. Furthermore, because of the knee's complicated anatomical structure, finite element models have been widely used in biomechanical studies of knee injuries [14]. However,

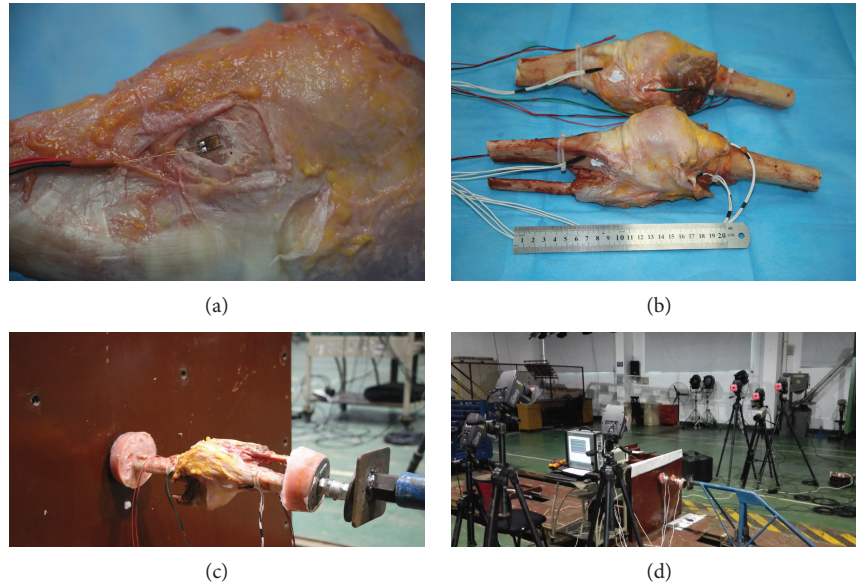


FIGURE 1: Photos of the experimental device to assess longitudinal impact on knee joints. (a) Method for implanting the knee joint strain sensing plate. (b) Condition after double knee electrode implantation. (c) Knee impact unit settings. (d) Traction track and Synergy version 5.0 data acquisition software.

in daily sports and military training [15], longitudinal impacts to the knee in a straight state often occur. In the above studies, the knee joint is mostly in a bent state [16], and studies assessing the mechanical response to longitudinal impacts to the knee in an extended state are relatively limited. As a result, the mechanical changes of the femoral-knee-tibiofibular structure and the mechanical responses of the accessory structures in the joint cavity while sustaining a longitudinal impact are still not clear. It is of great significance to explore the mechanisms and characteristics of longitudinal impact injuries with the knee in a straight position, as in sports and military injury scenarios. The purpose of the study, therefore, is to study the knee longitudinal impact injuries using both the impact experiment with cadaver knee samples and finite element model (FEM).

2. Materials and Methods

2.1. Knee Impact Experiment. This study was approved by the Ethics Committee of the Third Affiliated Hospital of the Third Military Medical University.

Two unembalmed cadavers (4 knees) were used. Before the experiment, knee X-ray examinations were performed for the two specimens, and the specimen with bone injuries would be excluded. Knee joint specimens were obtained using a chainsaw, the joint capsule remained intact, and 15 cm of the proximal and distal knees was preserved. A screw was fixed to the femoral head with bone cement, and the screw was mounted on a rigid wall. The tibial end was fixed with a screw, and a force sensor (CL-YD-311A, Sino-cera Piezotronics Inc., Jiangsu, China) was mounted to measure the impact force acting on the knee joint. Strain gauges (350Ω) were attached to the medial and lateral condyles of the femur of the knee joint and the medial and lateral tibia, respectively, to measure the amount of strain in the bone

(Figure 1). The specimens were put in a prone position during the knee impact experiment, that is, the patella was in a downward direction, the femur was connected with a fixed barrier, and the sled hit the tibia.

The impact experiments used a motor traction system, data acquisition system (Synergy C Rack, Hi-Techniques Inc., Madison, USA), and high-speed photography system (Phantom v12.1, Vision Research, Inc., Wayne, USA). The strain and impact force signals were sampled at a sampling frequency of 10 kHz. In the traction system, an impactor was mounted on a small sled, with a total mass of 65 kg. When the test was initiated, the sled was dragged and moved when it reached the specified speed. The moving impactor impacted the inferior portion of the knee. Each subject experienced the three impacts at the impact speed of 2.5 and 5.0 km/h and once at the impact speed of 8 km/h.

Following the impact, the responses of the knee joint were analyzed. In the study, ε is the strain value, determined by the formula $\varepsilon = \lim_{L \rightarrow 0} (\Delta L/L)$. In this formula, L is the length before deformation, ΔL is the elongated length, the strain unit is 1 (the skeletal deformation is 0.1%), and strain ε is expressed as 10^{-3} .

2.2. Finite Element Analysis. Anatomical knee data from the Chinese Visible Human (CVH) of the Third Military Medical University was selected and imported into Amira® software to outline the boundaries of the knee tissues, exported in ASCII data format, and finally imported into HyperMesh® to establish the initial knee model (Figure 2); the data were processed using surface smoothing, and high-order surfaces were created that closely fit the smoothed elements. As the corpse specimen was maintained in a supine position for a long time, the relative positions of the cartilage ligaments in the joint had changed; hence, the distorted structures, such

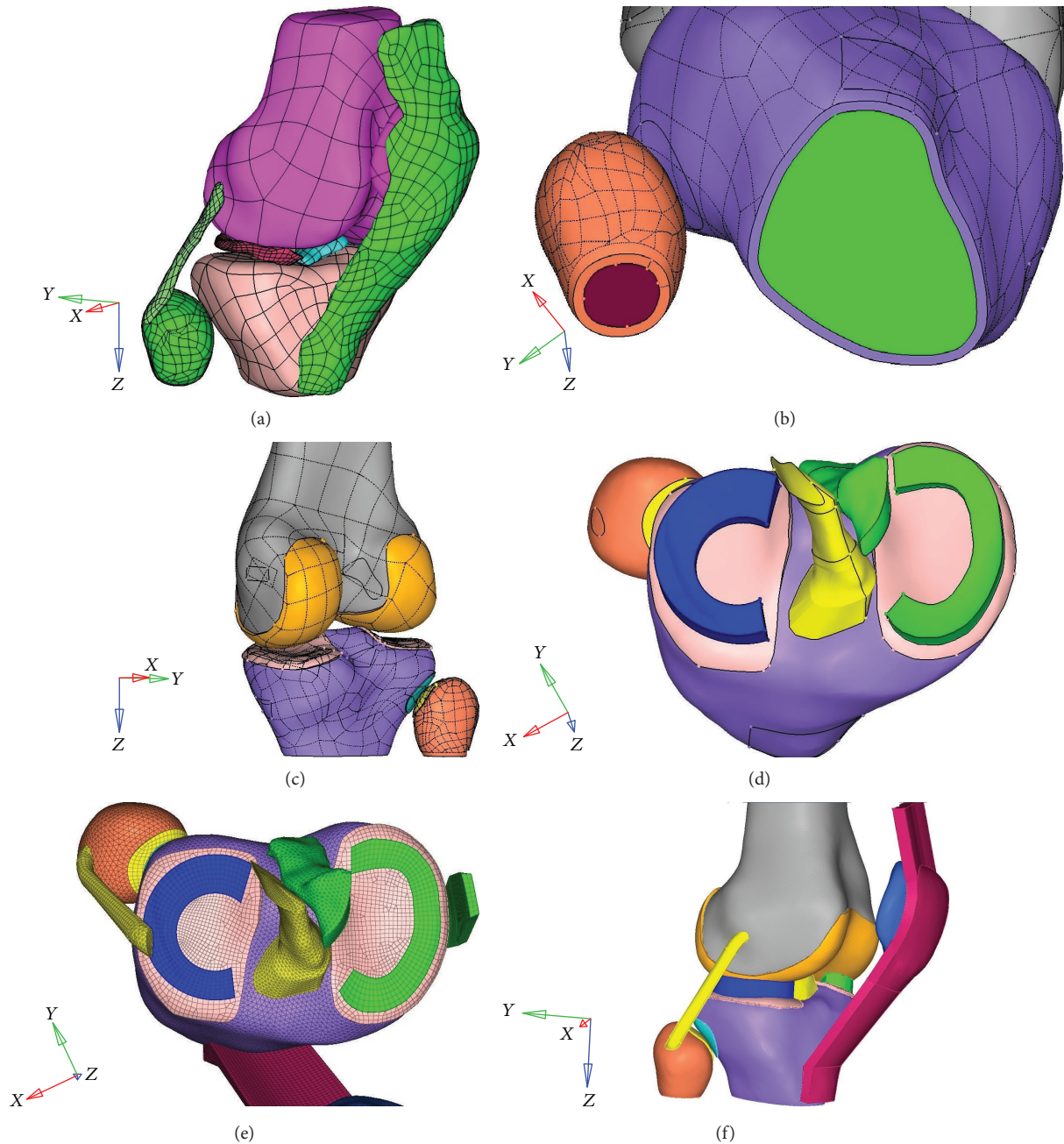


FIGURE 2: The development of the finite element model of the knee joint. (a) Initial inverse knee joint model showing a high-order surface after the smoothing processing. (b) The construction of cancellous bone and cortical bone boundaries; the inward bias of the cortical bone was set at 1.5 mm. (c) The articular cartilage thickness of the knee joint was set at 1 mm, and the cartilage thickness at the tibiofibular joint was set at 0.375 mm. (d) The reconstructed meniscus and cruciate ligament. (e) The mesh structure of the knee joint. (f) The completed finite element model of the knee joint.

as the meniscus and ligaments, needed to be artificially constructed; the connections between the bone and the ligaments needed to be reconstructed; and a 15 cm long osteotomy needed to be applied.

Due to the different mechanical properties of cortical bone and cancellous bone, the boundary between the cortical bone and the cancellous bone needed to be accurately established. The thickness of the cortical bone was set at 1.5 mm. Then, on the outer surface of the cortical bone, the boundaries of each cartilage were outlined with reference to the

anatomy. The outlined boundary was offset to the outside by an appropriate distance to generate the cartilage geometry of the body. The cartilage in the knee joint was set at a 1 mm thickness on the basis of references and anatomical structures, and the cartilage thickness in the tibiofibular joint was set at 0.375 mm. The medial meniscus is large and thin, with a “C” shape with a narrow front and a wide rear and an “O” shape on the outside [17]. The function of the meniscus is to stabilize the knee joint and transfer knee load [18]. The meniscus border was outlined in the tibial plateau

TABLE 1: Material assignment of the finite element model of the knee joint.

Materials	Model	Parameters	Reference
Cortical bone	ISO ILASTIC	$E = 12,000, u = 0.3$	[24]
Cancellous bone	ISO ILASTIC	$E = 400, u = 0.3$	[24]
Articular cartilage	ISO ILASTIC	$E = 100, u = 0.3$	[25]
Meniscus	ISO ILASTIC	Incompressible, $C10 = 2.67, C01 = 0.667 (E = 20, u = 0.49)$	[25]
Ligament	ISO ILASTIC	$E = 10, u = 0.3$	[26]

TABLE 2: Angle changes in knees at different velocities.

Impact speed	Range of motion				Mean value MAX° w(rad/s)
	N1 left MAX° w(rad/s)	N1 right MAX° w(rad/s)	N2 left MAX° w(rad/s)	N2 right MAX° w(rad/s)	
2.5 km/h	15.7	13.6	14.1	12.2	13.9 ± 1.0
	392.5	340.0	352.5	305.0	347.5 ± 25.0
5.0 km/h	26.2	20.6	35.2	32.4	28.6 ± 5.2
	1325.0	1030.0	1760	1620	1433.75 ± 256.25
8 km/h	94.1	98.6	83.2	88.6	91.1 ± 5.2
	9410.0	9860.0	8320.0	8860.0	9112.5 ± 522.5

MAX°: maximum deformation angle of the knee joint; W: A/T; A: angle change; T: time to maximum deformation.

cartilage. In addition, the connection between the cruciate ligament and the medial-lateral collateral ligament plays an extremely important role in the stability of the joint [19, 20]. The ligament model needed to be reconstructed based on the original ligament model and then connected with the bone [21].

During the mesh division, 1 mm grids were uniformly distributed on the surface of the meniscus. The grids were all quadrilateral and distributed in a concentric circular manner, and the surface grids were elongated into elements with a four-layer thickness. After dividing the meniscus mesh, the grids of the cartilage of the tibia that were connected with the meniscus were separated, and in this area, the nodes of the cartilage mesh were coincident with the nodes of the meniscus. Then, the grids on the medial collateral ligament, the patellar tendon, and the tibiofibular articular cartilage were divided. The cortical and cancellous bone regions were divided into 1 mm grids, which ensured more hexahedrons in the soft tissue, and the conjunction area between the soft tissue and bone shared the same nodes. Then, the grids on the femoral cartilage and lateral collateral ligament were divided. After finishing the grid division, the material properties, fixing, assembly, and loading constraints of the model were configured (Table 1), and the coefficient of friction was set as 0.1 [22]. Finally, a final finite element model of the knee joint was developed (Figure 2). Considering the brittle characteristics of the materials, the cortical bone was defined as failure when the stress reached 115 Mpa and the cancellous bone was considered failure when the stress reached 20 Mpa [23]. The model contained 490,978 units and 121,499 nodes.

3. Results

3.1. Knee Impact Experiment. The kinematic process were analyzed from the knee impact experiments, as shown in

Table 2, in which at the speeds of 2.5, 5, and 8 km/h, the maximal rotational angles of the knee joint were $13.8 \pm 1.2^\circ$, $30.2 \pm 5.1^\circ$, and $92.9 \pm 5.5^\circ$, respectively, while the angular velocities were 344.2 ± 30.8 rad/s, 1510.8 ± 252.5 rad/s, and 9290.0 ± 545.0 rad/s, respectively. Table 3 showed that with increases in collision velocity, the bone strain amplitude peak values and average values increased significantly, with significant differences between each group ($p < 0.05$).

No obvious damage was detected from the meniscus and ligaments at the impact speeds of 2.5 and 5.0 km/h, while at an impact velocity of 8 km/h, one knee of the two specimens showed fractures in the femoral shaft (Figure 3), and 3 knees showed fractures in the medial plateau, which were mostly split fractures and classified as Schatzker type IV. The collision strain curves at the impact rates of 2.5 km/h and 5 km/h were compared and showed that the velocity was positively related to the peak of the strain curve and the strain time (Figure 4).

3.2. Finite Element Simulation. Figure 5 showed the kinematic process and stress distribution with the failure mode, in which at an impact velocity of 2.5 km/h, for example, the bottom of the medial tibia first showed failure and then the failure extended to the center of the tibia until the entire tibial plateau was fractured. The knee was further inverted throughout the impact process. Before the fracture, the maximal varus angle of the femur was 12.28° . At an impact velocity of 5 km/h, the bottom of the medial tibia first showed cracks, and then, the crack extended to the center of the tibia until the entire tibial plateau was fractured. Compared to the 2.5 km/h impact velocity, the destruction was more intense at an impact velocity of 5 km/h. The figure also showed cracks at the bottom of the medial tibia at an impact speed of 8 km/h, followed by more intense fractures, making the entire fixed plane to show a comminuted fracture.

TABLE 3: Strain and impact force of knee joint.

Specimen	Impact speed	Strain				Impact force (N) Peak value
		Medial condyle of femur Peak value ($\times 10^{-6}$)	Lateral condyle of femur Peak value ($\times 10^{-6}$)	Medial condyle of tibia Peak value ($\times 10^{-6}$)	Lateral condyle of tibia Peak value ($\times 10^{-6}$)	
N1	2.5 km/h	2116.3 \pm 31.3	1835.5 \pm 32.1	3258.3 \pm 53.6	1357.5 \pm 24.3	2164.4 \pm 421.2
	5.0 km/h	4815.7 \pm 83.7	3865.4 \pm 63.2	7103.1 \pm 97.3	1394.6 \pm 23.1	3729.5 \pm 127.3
	8 km/h	6581.4 \pm 149.6	5321.5 \pm 161.2	12634.6 \pm 235.6	7653.2 \pm 81.6	5639.2 \pm 653.8
N2	2.5 km/h	1534.6 \pm 30.1	1235.2 \pm 16.3	3125.4 \pm 14.3	2525.1 \pm 21.3	2310.2 \pm 324.5
	5.0 km/h	4635.2 \pm 21.3	3765.4 \pm 59.3	7058.5 \pm 85.2	2312.6 \pm 25.1	4720.3 \pm 797.8
	8 km/h	6638.2 \pm 152.6	4521.5 \pm 122.6	11562.3 \pm 211.5	8426.9 \pm 74.2	6591.2 \pm 336.2
N3	2.5 km/h	2015.5 \pm 21.6	1845.3 \pm 30.5	3325.1 \pm 56.4	1325.3 \pm 21.1	2246.1 \pm 399.2
	5.0 km/h	4526.1 \pm 78.6	3567.4 \pm 61.2	6829.5 \pm 88.5	3356.2 \pm 21.0	5528.7 \pm 639.4
	8 km/h	7229.6 \pm 126.5	5638.2 \pm 121.6	11561.2 \pm 253.6	8465.3 \pm 75.3	8639.2 \pm 556.2
N4	2.5 km/h	1985.6 \pm 22.9	1562.8 \pm 16.2	3122.4 \pm 33.2	1242.6 \pm 22.6	2256.8 \pm 413.5
	5.0 km/h	4562.3 \pm 56.9	3356.2 \pm 22.9	5687.2 \pm 88.6	1234.1 \pm 56.3	4562.5 \pm 648.3
	8 km/h	6675.3 \pm 133.5	5013.2 \pm 155.2	8965.8 \pm 225.1	6628.1 \pm 85.3	5864.2 \pm 655.2

Figure 6 shows the strain of the bone impacted at the varied speeds. The curves indicated that the strain peak occurred first in the medial tibia and that the bigger the impact velocity, the earlier the peak appeared. The data in Figure 7 indicated that the medial strain of the tibia was still at a relatively small level when the peak of the strain reached at the medial tibia. Due to the destruction of the medial tibia, the maximum strain was the strain value at breakage, and the strain was essentially the same.

The simulation for the longitudinal impacts to knee joint exhibited varied degrees of varus at various impact speeds as shown in Figure 8. The maximum varus angles under the three impact velocities before the fracture are shown in Figure 9. As shown in Figure 10, before the initial crack, the stress on both menisci increased rapidly, and the medial side was slightly larger than the lateral side. When the crack occurred in the medial tibial base, the stress on the medial meniscus increased slowly. At this time, the lateral meniscus stress was greater than that of the inside. The meniscus stress had the same tendencies at all the speeds.

4. Discussion

Impacting injury to the knee joint is most commonly seen in traffic injuries [27] or sports injuries [28]. Most studies have been conducted under knee bending conditions [29], and there are relatively few studies on the mechanisms and characteristics of impact injury, especially for knee injuries induced by longitudinal impacts. In this study, knee specimens obtained from unembalmed cadavers were used, and the impact tests were conducted in a straight knee position to simulate the occurrence of human falling injuries or military training injuries and to explore the biomechanical characteristics of longitudinal impacts on the knee joint [30].

Previous experimental studies of impact injuries have mostly focused on the knee injury mechanisms in traffic accidents [27]. Bose et al. [31] conducted collision tests on 40 knee specimens to simulate knee impact injuries

in traffic accidents to explore the threshold of the knee valgus angle and shear displacement. Ruan et al. [4] showed that in frontal collisions between motor vehicles and pedestrians, the knee flexion angle, impact direction, and shape of the contact surface were all factors that affected the severity of the injury.

Our knee longitudinal impact experiment found that the speed of the impact unit was positively related to the knee flexion speed and the angle of flexion, indicating that the human knee buffers longitudinal impacts on the knee through knee flexion when falling from a high level, which may be related to increased contact area and longer force duration resulting from meniscus deformation during knee flexion [32]. At the same time, the initial flexion angular velocity is smaller during the process of knee flexion, and the angular velocity increases rapidly after a 30° flexion, which is related to the stress characteristics of the knee flexion process. We assume that the bone of the femoral and tibial medial and lateral condyle is the same, and knee stress findings showed that under the same impact velocity, the medial tibial plateau and the medial femoral condyle had greater deformation, stress range, and peak values. Our study found that in impact experiments using the cadaveric specimen, the knee injury but fracture was difficult to detect while Pedersen et al. [33] considered that among the longitudinal knee impact injuries, bone contusion sizes combined with time of persistence are likely better measures of joint injury severity than isolated bone contusion volume.

In addition, studies [34] have shown that the bone mineral density of the medial tibial plateau is lower than that of the lateral side, which is one of the reasons that the medial side is more vulnerable. Yukata et al. [35] studied stress fractures of the tibial plateau and found that all stress fractures occurred in the medial plateau and that the fracture location was related to the posterior tilt of the medial tibial plateau. In our study, we found that in the knee longitudinal collision injury test, a longitudinal low-speed impact often led to an inner knee injury and a high-speed collision often resulted

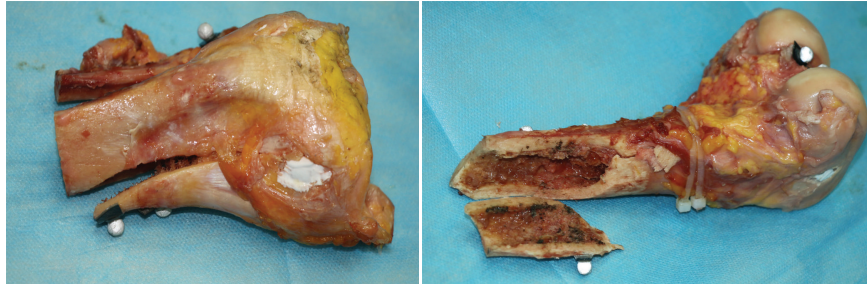


FIGURE 3: A fractured joint specimen at an impact speed of 8 km/h.

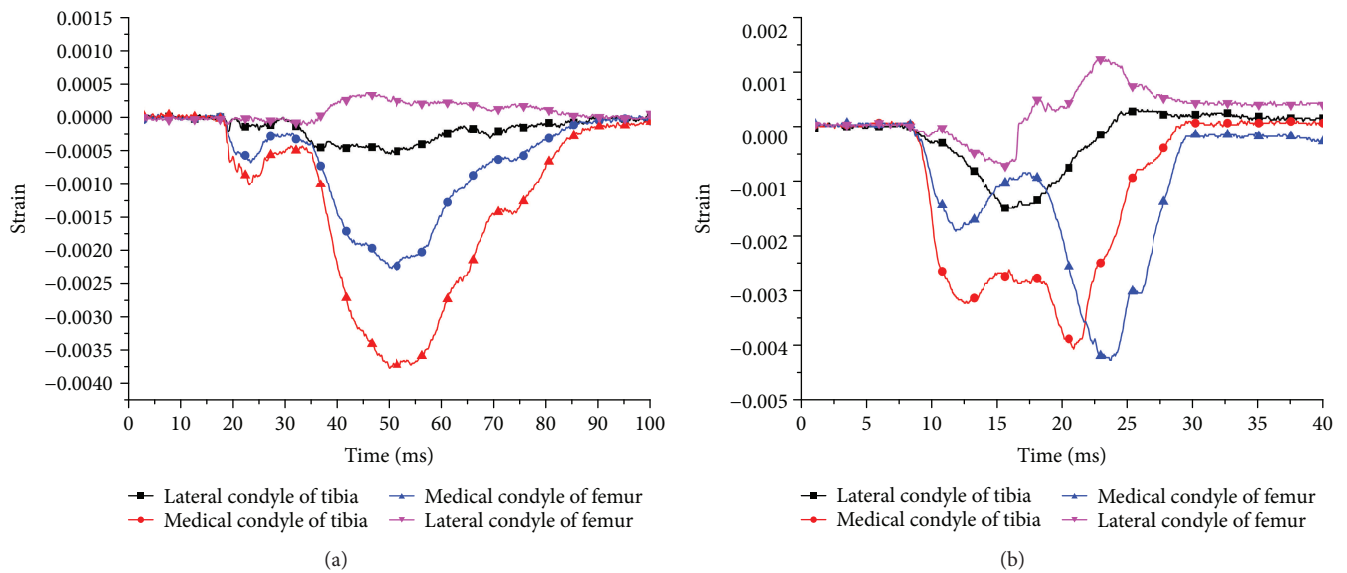


FIGURE 4: The strain curves of bones in the knee joints at the impact speeds of 2.5 (a) and 5 km/h (b).

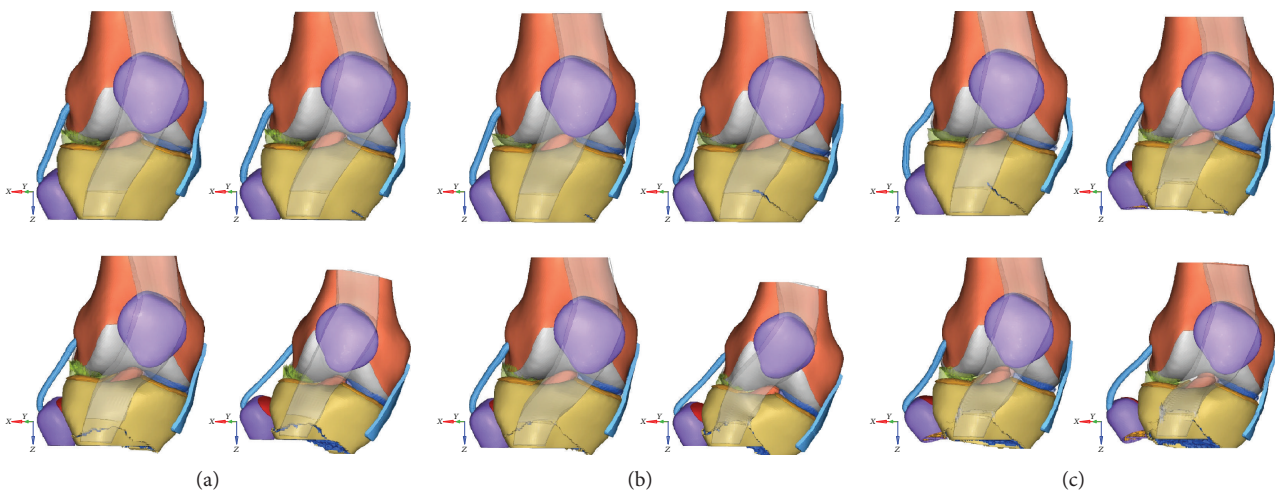


FIGURE 5: Knee kinematic process at the varied impact speeds ((a) 2.5 km/h; (b) 5.0 km/h; (c) 8.0 km/h).

in both medial and lateral knee injuries. In actual scenarios, there were several injury risks associated with the longitudinal knee impact injuries, that is, male patients, age < 30 years, and particularly patients who sustained a contact injury, and as a result, special attention is therefore necessary in those

patients and early referral to magnetic resonance imaging and/or arthroscopy is recommended to allow meniscus repair in a timely manner [36].

In recent years, finite element analysis has been widely used, applied in the establishment of joint models, and used

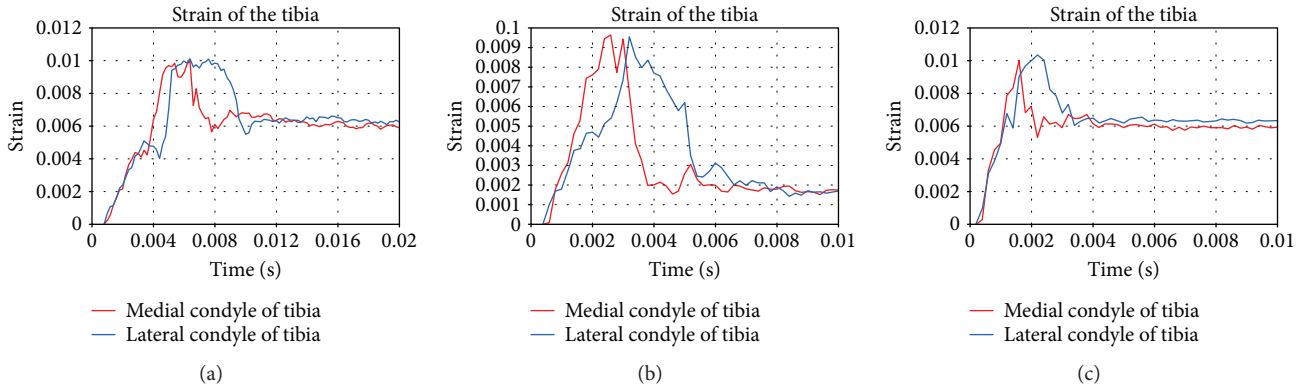


FIGURE 6: The strain response of medial and lateral tibial strain curves at the varied impact speeds ((a) 2.5 km/h; (b) 5.0 km/h; (c) 8.0 km/h).

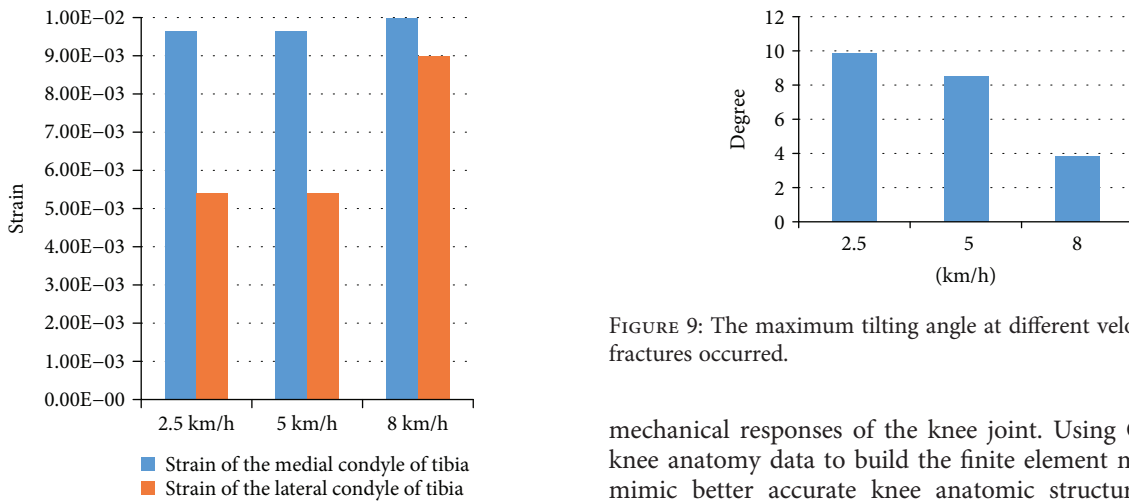


FIGURE 7: Strain peaks of the medial tibia at the varied impact speeds.

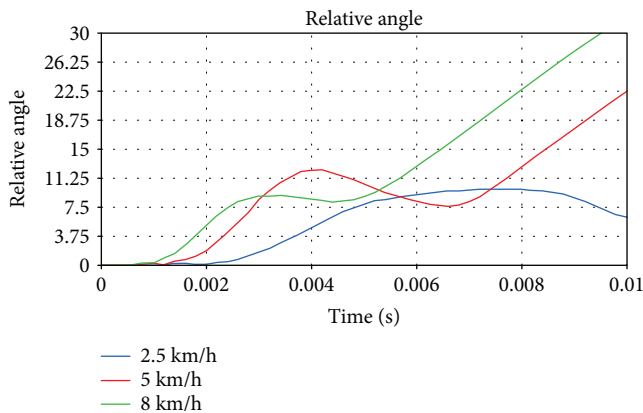


FIGURE 8: Curves of the varus angle at different impact speeds.

to simulate joint stress changes under different conditions, such as changes in the stress and strain of the femur and tibia after hip and knee replacements [3, 37–41]. Compared to experiments, the simulations conducted using finite element models have advantages such as high efficiency and noninvasiveness, and they allow for the expedient study of the

FIGURE 9: The maximum tilting angle at different velocities before fractures occurred.

mechanical responses of the knee joint. Using CVH-based knee anatomy data to build the finite element model could mimic better accurate knee anatomic structure, while it may reconstruct the meniscus and related ligaments in the knee and ensures the stability of the knee in the sagittal plane [42]. In the simulated impact experiment, the simulated impact unit used an average 65 kg body weight at the varied impact speeds to maximally simulate the characteristics of stress and strain in the knee joint during the longitudinal impact process. The results from the simulation and experiment showed that the knee begins to rotate when a longitudinal impact is loaded, and with an increase in the impact energy, the angle of the rotation increased. Our results found that in addition to rotation, the bone sustained a strain when knee was contacted. Huang et al. also showed that a knee joint finite element model could effectively simulate the characteristics of knee injury caused by contact in a car accident [43].

Makinejad et al. [44] studied the mechanisms of longitudinal impacts on the knee joint, which was similar to our study. They investigated the stress and deformation processes of the knee joint during the falling process from different heights and concluded that longitudinal impact to the knee joint is more likely to cause damage, but the distribution of the injury sites is not yet clear. Dong et al. [45] kept the knee straight and compressed 1150 N on the knee joint and concluded that a meniscus tear and partial meniscectomy can accelerate the knee joint injury, which had a significant effect on the pressure peaks and shearing force of medial meniscus and cartilage, which is consistent with the results

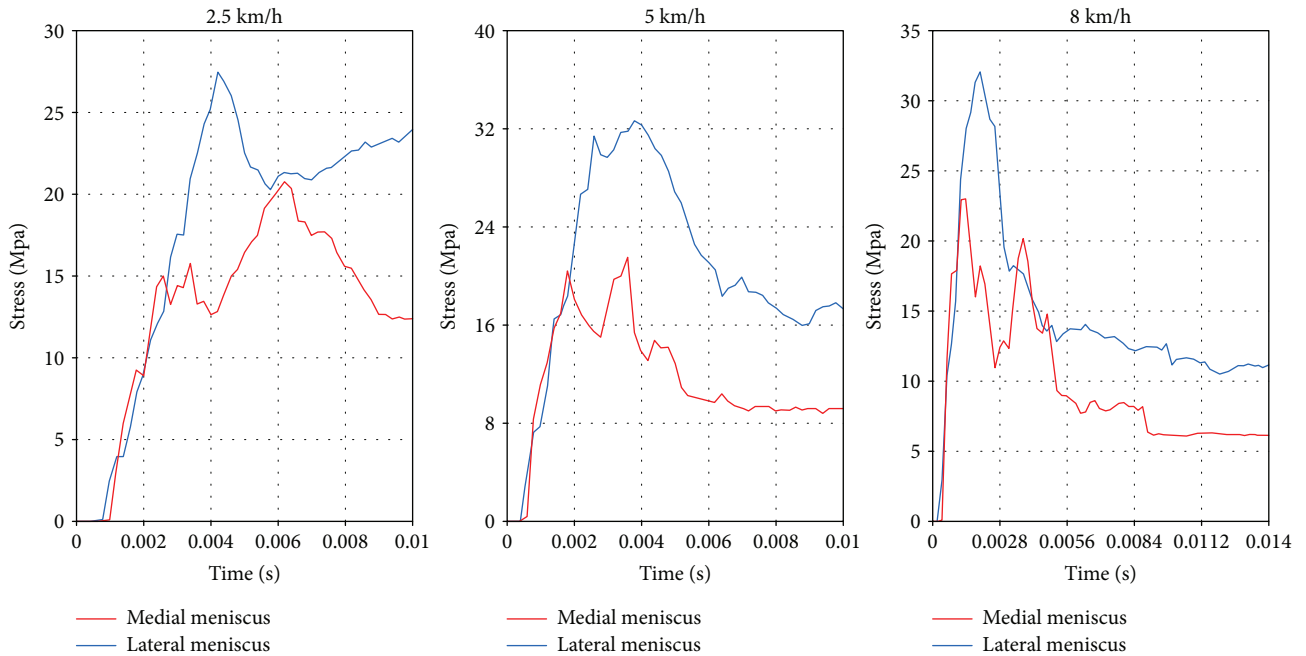


FIGURE 10: Meniscus stress curves at the varied impact speeds.

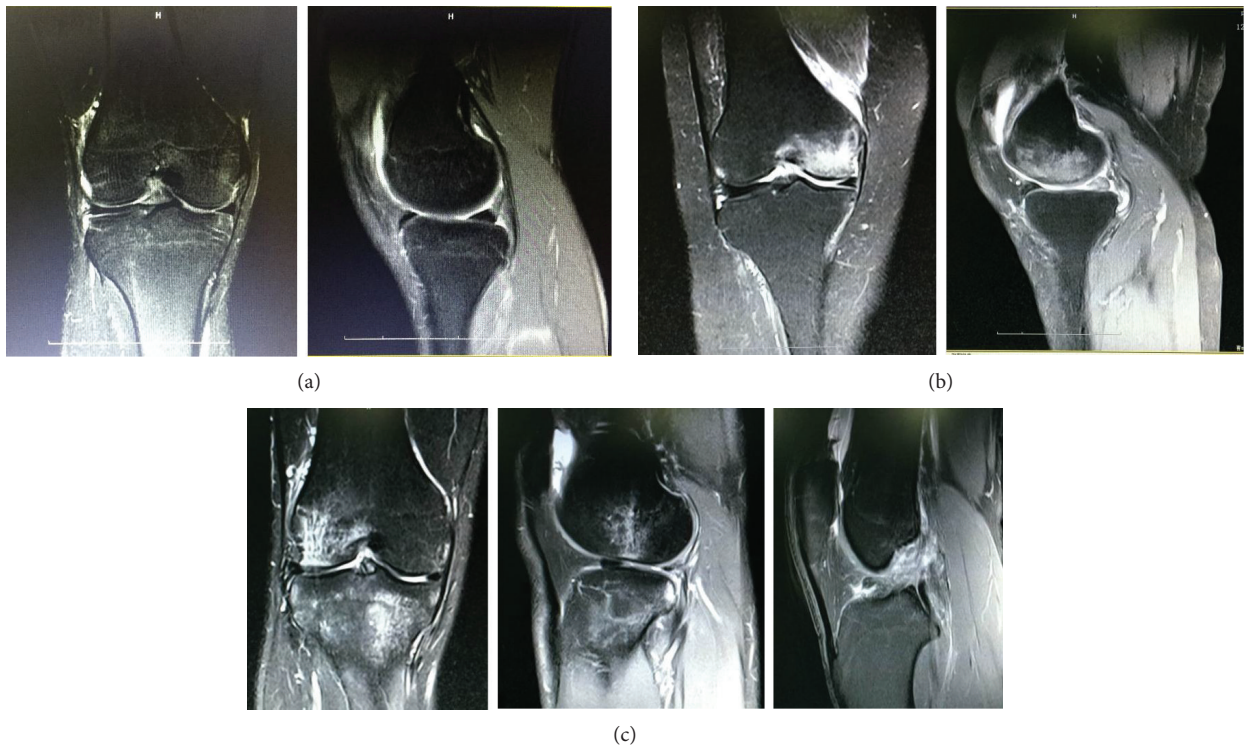


FIGURE 11: (a) Case 1: male, 21 years old, long distance runner, right knee pain, and swelling after knee longitudinal impact injury in one long-distance race. MRI showed that medial femur and medial tibia had mild bone bruise, bone marrow edema, and mild joint effusion. (b) Case 2: male, 77 years old, right knee pain, and swelling after one falling longitudinal impact injury at one meter high. MRI showed widely that medial femoral condyle had bone marrow injury and edema. Medial tibia had mild bone bruise and joint effusion. (c) Case 3: male, 22 years old, soldier, right knee pain, swelling, and movement dysfunction after knee longitudinal impact injury in one military training. MRI showed widely that medial tibia had bone marrow edema, meniscus injury, and rupture of anterior cruciate ligament.

of this study. Our study found that there was a greater risk of injury to the medial meniscus, tibia, and medial femoral condyle of the knee when the knee collision occurred while the knee was straight; that longitudinal low-speed impact mainly led to inner knee injury; and that high-speed impact led to both lateral and medial knee injuries. Some studies [46] have shown that incorrect running posture can cause varus deformities of the knee and even cause “O”-shaped legs. The stress distribution and damage characteristics of longitudinal impact injuries to the knee joint in the corpse specimens were consistent with those of the three-dimensional finite element analysis and coincided with the medial stress fractures seen in knee joints in clinical practice, as shown in Figure 11. To prevent knee arthritis [47], one should also consider the more severe medial stress damage caused by repeated longitudinal impact injuries to the knee joint during daily life; thus, the incidence of knee osteoarthritis with genu varum is higher. Moreover, in clinical practice, in the early stages of knee osteoarthritis, using a lateral fibular osteotomy to reduce the medial knee stress can achieve good clinical efficacy [48].

5. Limitations

In this study, the collision experiment used knee specimens for in vitro experiments, which have both advantages [13] and shortcomings. As the body specimens enrolled in the study were old, the structure and strength may have been different from younger specimens. Consequently, the responses derived from the study may represent those occurring in seniors. The number of specimens used in this study was small, and the specimens experienced more than one impact. In the impact experiment, however, the cumulative effects of impact at different speeds were not considered. The establishment of the knee finite element model was based on CVH data rather than the specimens, while the difference between the tested specimens and the finite element model was not considered, and the further validation has not been done in the present study.

6. Conclusion

The three-dimensional finite element analysis and impact experiments showed that the stress response characteristics of the femur and the medial condyle of the tibia are more prone to damage under different longitudinal impact velocities. Longitudinal low-speed collisions often lead to inner knee injury, and high-speed collisions often result in both medial and lateral knee injuries. This study can play an important role in providing key data for the prevention and treatment of longitudinal collision injuries of the knee joint.

Data Availability

The data used to support the findings of this study are available from the corresponding author upon request.

Conflicts of Interest

The authors declare that they have no conflicts of interest.

Acknowledgments

This study was supported by grants from the National Key Research and Development Program (2016YFC0800702), Army Medical Science and Technology Youth Fund (14QNP091), and National Natural Science Foundation of China (81772330).

References

- [1] B. Nie, J. R. Crandall, and M. B. Panzer, “Computational investigation of the effects of knee airbag design on the interaction with occupant lower extremity in frontal and oblique impacts,” *Traffic Injury Prevention*, vol. 18, no. 2, pp. 207–215, 2016.
- [2] K. L. Cameron, K. Y. Peck, B. S. Thompson, S. J. Svoboda, B. D. Owens, and S. W. Marshall, “Reference values for the Marx activity rating scale in a young athletic population: history of knee ligament injury is associated with higher scores,” *Sports Health: A Multidisciplinary Approach*, vol. 7, no. 5, pp. 403–408, 2015.
- [3] N. Filipovic, R. Vulovic, A. Peulic, R. Radakovic, D. Kosanic, and B. Ristic, “Noninvasive determination of knee cartilage deformation during jumping,” *Journal of Sports Science & Medicine*, vol. 8, no. 4, pp. 584–590, 2009.
- [4] J. S. Ruan, R. el-Jawahri, S. Barbat, S. W. Rouhana, and P. Prasad, “Impact response and biomechanical analysis of the knee-thigh-hip complex in frontal impacts with a full human body finite element model,” *Stapp Car Crash Journal*, vol. 52, pp. 505–526, 2008.
- [5] J. Multanen, T. Rantalainen, H. Kautiainen et al., “Effect of progressive high-impact exercise on femoral neck structural strength in postmenopausal women with mild knee osteoarthritis: a 12-month RCT,” *Osteoporosis International*, vol. 28, no. 4, pp. 1323–1333, 2017.
- [6] N. A. Mohd Sharif, S. L. Goh, J. Usman, and W. K. Z. Wan Safwani, “Biomechanical and functional efficacy of knee sleeves: a literature review,” *Physical Therapy in Sport*, vol. 28, pp. 44–52, 2017.
- [7] P. Thangavel, S. Vidhya, J. Li, E. Chew, A. Bezerianos, and H. Yu, “Biomechanical effects of robot assisted walking on knee joint kinematics and muscle activation pattern,” in *2017 International Conference on Rehabilitation Robotics (ICORR)*, vol. 2017, pp. 252–257, London, UK, July 2017.
- [8] J. C. Carter, D. R. Sturnick, P. M. Vacek et al., “Relationship between geometry of the extensor mechanism of the knee and risk of anterior cruciate ligament injury,” *Journal of Orthopaedic Research*, vol. 35, no. 5, pp. 965–973, 2017.
- [9] E. Cetinkaya, C. G. Aydin, Y. E. Akman et al., “A rare knee extensor mechanism injury: vastus intermedius tendon rupture,” *International Journal of Surgery Case Reports*, vol. 14, pp. 186–188, 2015.
- [10] A. M. Kiapour, C. E. Quatman, V. K. Goel, S. C. Wordeman, T. E. Hewett, and C. K. Demetropoulos, “Timing sequence of multi-planar knee kinematics revealed by physiologic cadaveric simulation of landing: implications for ACL injury mechanism,” *Clinical Biomechanics (Bristol, Avon)*, vol. 29, no. 1, pp. 75–82, 2014.
- [11] K. M. Fischenich, K. D. Button, G. A. Coatney et al., “Chronic changes in the articular cartilage and meniscus following traumatic impact to the lapine knee,” *Journal of Biomechanics*, vol. 48, no. 2, pp. 246–253, 2015.

- [12] B. J. Ewers, V. M. Jayaraman, R. F. Banglmaier, and R. C. Haut, "The effect of loading rate on the degree of acute injury and chronic conditions in the knee after blunt impact," *Stapp Car Crash Journal*, vol. 44, pp. 299–313, 2000.
- [13] L. Maletsky, S. Shalhoub, F. Fitzwater et al., "In vitro experimental testing of the human knee: a concise review," *The Journal of Knee Surgery*, vol. 29, no. 2, pp. 138–148, 2016.
- [14] A. Kiapour, A. M. Kiapour, V. Kaul et al., "Finite element model of the knee for investigation of injury mechanisms: development and validation," *Journal of Biomechanical Engineering*, vol. 136, no. 1, article 011002, 2014.
- [15] J. Divine, "Exercise training to prevent anterior knee pain in military recruits," *Clinical Journal of Sport Medicine*, vol. 22, no. 3, pp. 288–289, 2012.
- [16] R. Torres, J. Ferreira, D. Silva, E. Rodrigues, I. M. Bessa, and F. Ribeiro, "Impact of patellar tendinopathy on knee proprioception: a cross-sectional study," *Clinical Journal of Sport Medicine*, vol. 27, no. 1, pp. 31–36, 2017.
- [17] D. Kohn and B. Moreno, "Meniscus insertion anatomy as a basis for meniscus replacement: a morphological cadaveric study," *Arthroscopy*, vol. 11, no. 1, pp. 96–103, 1995.
- [18] A. J. S. Fox, F. Wanivenhaus, A. J. Burge, R. F. Warren, and S. A. Rodeo, "The human meniscus: a review of anatomy, function, injury, and advances in treatment," *Clinical Anatomy*, vol. 28, no. 2, pp. 269–287, 2015.
- [19] A. N. Varelas, B. J. Erickson, G. L. Cvetanovich, and B. R. Bach Jr, "Medial collateral ligament reconstruction in patients with medial knee instability: a systematic review," *Orthopaedic Journal of Sports Medicine*, vol. 5, no. 5, 2017.
- [20] C. Domnick, K. H. Frosch, M. J. Raschke et al., "Kinematics of different components of the posterolateral corner of the knee in the lateral collateral ligament-intact state: a human cadaveric study," *Arthroscopy: The Journal of Arthroscopic & Related Surgery*, vol. 33, no. 10, pp. 1821–1830.e1, 2017.
- [21] F. Djoudi, "3D reconstruction of bony elements of the knee joint and finite element analysis of total knee prosthesis obtained from the reconstructed model," *Journal of Orthopaedics*, vol. 10, no. 4, pp. 155–161, 2013.
- [22] M. W. J. Arun, S. Umale, J. R. Humm, N. Yoganandan, P. Hadagali, and F. A. Pintar, "Evaluation of kinematics and injuries to restrained occupants in far-side crashes using full-scale vehicle and human body models," *Traffic Injury Prevention*, vol. 17, Supplement 1, pp. 116–123, 2016.
- [23] L. L. C. Element, "User manual: M50 occupant version 4.3 for Ls-Dyna," *Global Human Body Model Consortium-owned GHBMC Model*, 2014.
- [24] Q. H. Zhang, E. C. Teo, H. W. Ng, and V. S. Lee, "Finite element analysis of moment-rotation relationships for human cervical spine," *Journal of Biomechanics*, vol. 39, no. 1, pp. 189–193, 2006.
- [25] T. R. Pitzen, D. Matthis, D. D. Barbier, and W. I. Steudel, "Initial stability of cervical spine fixation: predictive value of a finite element model. Technical note," *Journal of Neurosurgery*, vol. 97, 1 Supplement, pp. 128–134, 2002.
- [26] H. Schmidt, F. Heuer, U. Simon et al., "Application of a new calibration method for a three-dimensional finite element model of a human lumbar annulus fibrosus," *Clinical Biomechanics (Bristol, Avon)*, vol. 21, no. 4, pp. 337–344, 2006.
- [27] K. Nagasaka, K. Mizuno, E. Tanaka et al., "Finite element analysis of knee injury risks in car-to-pedestrian impacts," *Traffic Injury Prevention*, vol. 4, no. 4, pp. 345–354, 2003.
- [28] N. Yoganandan, A. Banerjee, F. C. Hsu et al., "Deriving injury risk curves using survival analysis from biomechanical experiments," *Journal of Biomechanics*, vol. 49, no. 14, pp. 3260–3267, 2016.
- [29] P. J. Atkinson and R. C. Haut, "Injuries produced by blunt trauma to the human patellofemoral joint vary with flexion angle of the knee," *Journal of Orthopaedic Research*, vol. 19, no. 5, pp. 827–833, 2001.
- [30] P. J. Atkinson and R. C. Haut, "Impact responses of the flexed human knee using a deformable impact interface," *Journal of Biomechanical Engineering*, vol. 123, no. 3, pp. 205–211, 2001.
- [31] D. Bose, K. S. Bhalla, C. D. Untaroiu, B. J. Ivarsson, J. R. Crandall, and S. Hurwitz, "Injury tolerance and moment response of the knee joint to combined valgus bending and shear loading," *Journal of Biomechanical Engineering*, vol. 130, no. 3, article 031008, 2008.
- [32] T. F. Besier, C. E. Draper, G. E. Gold, G. S. Beaupré, and S. L. Delp, "Patellofemoral joint contact area increases with knee flexion and weight-bearing," *Journal of Orthopaedic Research*, vol. 23, no. 2, pp. 345–350, 2005.
- [33] D. R. Pedersen, G. Y. el-Khoury, D. R. Thedens, M. Saad-Eldine, P. Phisitkul, and A. Amendola, "Bone contusion progression from traumatic knee injury: association of rate of contusion resolution with injury severity," *Open Access Journal of Sports Medicine*, vol. Volume 8, pp. 9–15, 2017.
- [34] G. H. Lo, Y. Zhang, C. McLennan et al., "The ratio of medial to lateral tibial plateau bone mineral density and compartment-specific tibiofemoral osteoarthritis," *Osteoarthritis and Cartilage*, vol. 14, no. 10, pp. 984–990, 2006.
- [35] K. Yukata, I. Yamanaka, Y. Ueda et al., "Medial tibial plateau morphology and stress fracture location: a magnetic resonance imaging study," *World Journal of Orthopedics*, vol. 8, no. 6, pp. 484–490, 2017.
- [36] M. J. Feucht, S. Bigdon, G. Bode et al., "Associated tears of the lateral meniscus in anterior cruciate ligament injuries: risk factors for different tear patterns," *Journal of Orthopaedic Surgery and Research*, vol. 10, no. 1, p. 34, 2015.
- [37] F. M. Pfeiffer, "The use of finite element analysis to enhance research and clinical practice in orthopedics," *The Journal of Knee Surgery*, vol. 29, no. 2, pp. 149–158, 2016.
- [38] C. Y. Chang, J. D. Rupp, M. P. Reed, R. E. Hughes, and L. W. Schneider, "Predicting the effects of muscle activation on knee, thigh, and hip injuries in frontal crashes using a finite-element model with muscle forces from subject testing and musculoskeletal modeling," *Stapp Car Crash Journal*, vol. 53, pp. 291–328, 2009.
- [39] H. N. Beidokhti, D. Janssen, S. van de Groes, and N. Verdonschot, "The peripheral soft tissues should not be ignored in the finite element models of the human knee joint," *Medical & Biological Engineering & Computing*, vol. 56, no. 7, pp. 1189–1199, 2018.
- [40] S. C. Huang, "The study of stresses characteristic of contact mechanism in total knee replacement using two-dimensional finite element analysis," *Bio-medical Materials and Engineering*, vol. 28, no. 5, pp. 567–578, 2017.
- [41] Z. H. Sun, Y. J. Liu, and H. Li, "Femoral stress and strain changes post-hip, -knee and -ipsilateral hip/knee arthroplasties: a finite element analysis," *Orthopaedic Surgery*, vol. 6, no. 2, pp. 137–144, 2014.
- [42] D. Ren, Y. Liu, X. Zhang, Z. Song, J. Lu, and P. Wang, "The evaluation of the role of medial collateral ligament

- maintaining knee stability by a finite element analysis,” *Journal of Orthopaedic Surgery and Research*, vol. 12, no. 1, p. 64, 2017.
- [43] W. H. Huang, P. Huang, Z. D. Li et al., “3D finite element model of human knee injuries in the traffic accident,” *Fa Yi Xue Za Zhi*, vol. 30, no. 1, pp. 1–6, 2014.
- [44] M. D. Makinejad, N. A. Osman, W. A. Abas, and M. Bayat, “Preliminary analysis of knee stress in full extension landing,” *Clinics (São Paulo, Brazil)*, vol. 68, no. 9, pp. 1180–1188, 2013.
- [45] Y. Dong, G. Hu, Y. Dong, Y. Hu, and Q. Xu, “The effect of meniscal tears and resultant partial meniscectomies on the knee contact stresses: a finite element analysis,” *Computer Methods in Biomechanics and Biomedical Engineering*, vol. 17, no. 13, pp. 1452–1463, 2014.
- [46] K. Asadi, A. Mirbolook, A. Heidarzadeh, M. Mardani Kivi, M. K. Emami Meybodi, and M. Rouhi Rad, “Association of soccer and genu varum in adolescents,” *Trauma Monthly*, vol. 20, no. 2, p. e17184, 2015.
- [47] M. A. Lopez-Olivo, A. Ingleshwar, R. J. Volk et al., “Development and pilot testing of multimedia patient education tools for patients with knee osteoarthritis, osteoporosis, and rheumatoid arthritis,” *Arthritis Care & Research*, vol. 70, no. 2, pp. 213–220, 2018.
- [48] Z. Y. Yang, W. Chen, C. X. Li et al., “Medial compartment decompression by fibular osteotomy to treat medial compartment knee osteoarthritis: a pilot study,” *Orthopedics*, vol. 38, no. 12, pp. e1110–e1114, 2015.

Research Article

Numerical Low-Back Booster Analysis on a 6-Year-Old Infant during a Frontal Crash Test

I. L. Cruz-Jaramillo ¹, C. R. Torres-San-Miguel,¹ O. Cortes-Vásquez,¹ and L. Martínez-Sáez²

¹Instituto Politécnico Nacional, Sección de Estudios de Posgrado e Investigación, Unidad Profesional “Adolfo López Mateos”, Escuela Superior de Ingeniería Mecánica y Eléctrica Zacatenco, Edificio 5, 2° Piso Col. Lindavista, 07738 México City, Mexico

²Universidad Politécnica de Madrid, Instituto Universitario de Investigación del Automóvil, Campus Sur UPM, Carretera de Valencia A-3, km. 7, 28031 Madrid, Spain

Correspondence should be addressed to I. L. Cruz-Jaramillo; breaking_182@hotmail.com

Received 3 April 2018; Accepted 24 June 2018; Published 16 July 2018

Academic Editor: Tatsuo Yoshino

Copyright © 2018 I. L. Cruz-Jaramillo et al. This is an open access article distributed under the Creative Commons Attribution License, which permits unrestricted use, distribution, and reproduction in any medium, provided the original work is properly cited.

This work studies descriptively the Head Injury Criterion (HIC) and Chest Severity Index (CSI), with a finite element model of the Hybrid III dummy type, for six-year-old subjects in a frontal vehicular collision, using the low-back booster (LBB) passive safety system. The vehicle seats and the passive safety systems were modelled in CAD (computer aided design) software. Then, the elements were analysed by the finite element method (FEM) in LS-DYNA® software. The boundary conditions were established for each study, according to the regulations established by the Federal Motor Vehicle Safety Standard (FMVSS), following the FMVSS 213 standard. The numerical simulations were performed during an interval of 120 ms and recording results every 1 ms. In order to analyse the efficiency of the system, the restraint performance of the LBB system is compared with the restraint configuration of the vehicle safety belt (VSB) only. The obtained injury criteria with the LBB system shows its ability to protect children in a frontal collision. The analyses allow obtaining the deceleration values to which the dummy head and chest was subjected. Of the studies herein performed, Study I: VSB obtained a HIC_{36} of 730.4 and CSI of 315.5, while Study II: LBB obtained a HIC_{36} of 554.3 and CSI of 281.9. The outcome shows that the restraint efficiency of each studied case differs. Used materials, the attachment system of the LBB, and the belt restraint system properly placed over the infant trunk are the main factors reducing the injury criteria rate.

1. Introduction

Annually, more than 260,000 children die worldwide as result of traffic collisions; it is also estimated that up to 10 million of them suffer nonfatal injuries. Trauma caused by traffic accidents are the second cause of death for children aged 5–14 years. The 22.3% of children who died during 2004 from 0 to 14 years old were involved in traffic accidents, of which the ones aged 5–9 years showed the highest mortality rate [1]. In Mexico, between 2000 and 2010, 17,700 children under the age of 15 have died in traffic accidents [2]. In 2011, traffic accidents in Mexico City became the third cause of death for children aged 5 to 9 years, as well as the fourth for children aged 10 to 14 years [3].

In 1972, the first Federal Safety Standard for children occupying vehicles FMVSS 213 (Federal Motor Vehicle Safety Standard) was issued, which specifies the requirements for infant seats to be marketed in the United States of America [4].

Severe injuries on the pelvis, shoulder, thorax, neck, and head have often occurred in frontal collisions. The neck usually experiences the inertial load generated by the head; during the initial phase of a crash, more restraint is applied in the lower neck, while the head is normally subjected to a horizontal translational displacement relative to the torso, inducing neck extension movements in frontal collisions [5]. Such movement generates high traction loads on the neck during the main horizontal deceleration of the head.

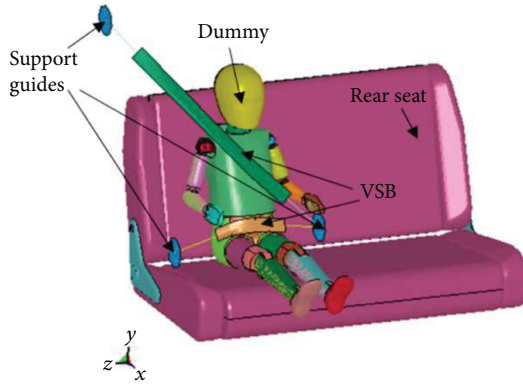


FIGURE 1: Study I (VSB).

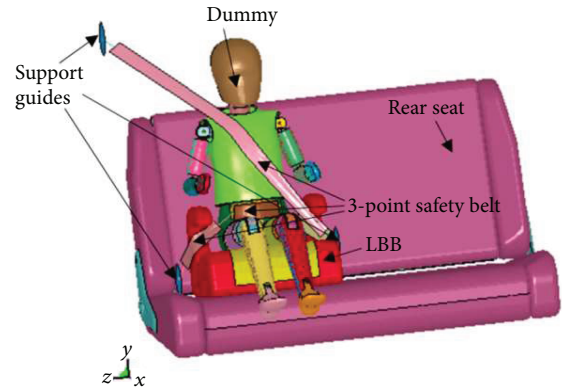


FIGURE 2: Study II (LBB).

The previous phenomenon occurs when no head contact exists with external objects like the backs of front seats.

The neck is exposed to significant mechanical loads when the natural range of neck extension and flexion is overpassed, causing elongation and tearing in different ligaments, as well as even the dislocation of the neck's articulations [6].

On the other side, chest injuries can range from rib fractures to even more severe injuries that cause internal organs to collide with internal body walls, producing abdominal bruises, wounds, and scratches. Lesions of the thoracic aorta, of the small intestine, or even mesentery, occur when the body abruptly stops while the interior organs and tissues continue to move forward by inertia, causing aortic twisting or tearing of intestinal loops at their mesenteric insertion [7].

The probability to suffer head injuries is calculated using HIC (Head Injury Criterion). The latter is obtained by calculating the resulting linear acceleration of the head's centre of gravity, and it is measured in units of the earth's gravity acceleration (g) [8]. HIC does not take into account factors such as the rotational acceleration of the skull or any effect on the location of the impact on the head. A HIC value of 1000 is considered as the threshold for brain lesions [9].

The FMVSS 208 establishes that in order to discard chest damage, the maximum acceleration on the chest must be below $60g$ in a time interval of 3 ms (CLIP3M) and a CSI (Chest Severity Index), calculated as the HIC but over the chest, value lower than 1000 [10].

The American Association of Paediatrics recommends the usage of a low-back booster (LBB) for children aged between 4 and 8 years or weighing 40–80 lb (18–36 kg) [11]. The Hybrid III 6-year-old dummy selected for this study fits well within these ranges of age and weight.

This research is intended to quantify the performance of a LBB system and to validate the numerical models with experimental tests performed by Hagedorn and Stammen [12].

2. Methods

In order to quantify the differences between HIC and CSI when implementing the LBB and vehicle seat belt (VSB),

two analysis scenarios were proposed and simulated with the LS-Dyna v. 9.7.1 software. Both analyses were performed with the Hybrid III 6-year-old FEM dummy model. The seat belt was modelled to perform the restraint analysis in both situations: VSB restraint only and VSB with the LBB under the dummy. The LBB Evenflo®, belonging to groups 2 and 3 (adjustable 3–11 years or 18–49.8 kg), was used to design the LBB system in CAD software.

The analyses were carried out with a crash speed of 48 km/h (13.34 m/s) as indicated by the FMVSS. The scenarios were done by implementing 2 passive safety systems (VSB and LBB):

- Study I (VSB): the dummy was placed on the back seat of a sedan vehicle and was restrained with just the seat belt implemented nowadays (Figure 1).
- Study II (LBB): the dummy was seated on the LBB and was secured with the 3-point safety belt included with the vehicle (Figure 2).

2.1. Designs and Materials. The vehicle rear seat was designed in CAD software accomplishing the approximate size of the rear seats of a model 2008 Honda Fit® vehicle.

The LBB is mounted on the rear seat as indicated in its user manual and the vehicle's user manual. The rear seat of the vehicle is composed of two materials: the steel bracket and the foam. A plastic holder is used as a joint between the seat backrest part and the seat cushion part.

In the same way, the LBB was designed with the measurements of the LBB Evenflo. It consists of structural material as well as foam. The rear seat with the LBB was assembled by CAD. Each study case is meshed by an Arbitrary Lagrangian-Eulerian (ALE) mesh, because it is a self-adjustable meshing method [13]. A mesh of 8 mm in size composed of 3D tetrahedral elements is computed and generated using the HyperMesh® V.14.0 software.

In order to accurately model the LBB structural material, polypropylene was selected. Polypropylene has the following mechanical properties: density of $9 \times 10^{-7} \text{ kg/mm}^3$, Young's modulus of 1.35 GPa, elastic limit of 0.036 GPa, and Poisson's ratio of 0.3 [14].

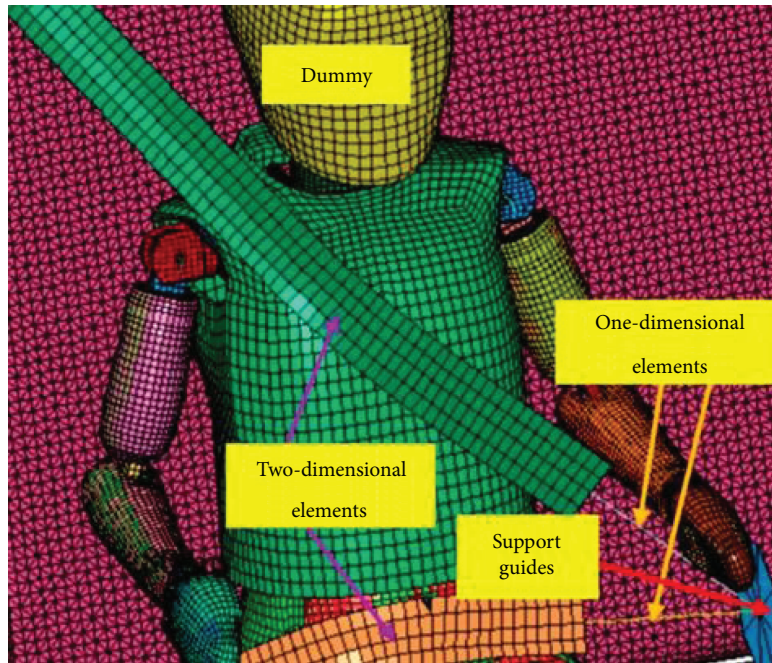


FIGURE 3: Design of the safety belts.

For the padding of the seat and LBB, the DAX 55 foam was chosen. This foam has the following mechanical properties: density of $3.5 \times 10^{-8} \text{ kg/mm}^3$, Young's modulus of $5 \times 10^{-5} \text{ GPa}$, and Poisson's ratio of 0.31 [15].

For the polypropylene and FAX 55 foam, the data presented above is to be loaded in LS-DYNA [16].

The mechanical properties of the steel bracket of the rear seat are: density of 7800 kg/mm^3 , Young's modulus of 210 GPa , elastic limit of 0.6 GPa , Poisson's ratio of 0.3, and tangent modulus of 0.3 GPa .

The design of the 3-point safety belt was made according to the specifications of the selected model of the belt, which is 4.7 cm wide by 1 mm thick. The design of the belts was performed with the BELFIT tool in the LS-DYNA software. The belt placement was performed according to the National Highway Traffic Safety Administration (NHTSA) standard (Figure 3). The design of the belts considered one-dimensional and two-dimensional elements (Figure 3).

Section and material for the one-dimensional elements were assigned with the predetermined seatbelt configuration in LS-DYNA. This material has a linear density of $\lambda = 5.97 \times 10^{-4} \text{ kg/mm}$ [17].

The two-dimensional elements were assigned a shell-type section with a thickness of 1 mm . Also, these elements were endowed with an elastoplastic-type material, with a piecewise linear plasticity behaviour and the mechanical properties of nylon: density of $1 \times 10^{-6} \text{ kg/mm}^3$, Young's modulus of 5.333 GPa , elastic limit of 0.08 GPa , and Poisson's ratio 0.3.

Curves of load and unload, representing the axial force as a function of the strain of the safety belt, were obtained by Dhole et al. [18]. The seat belts' anchorage guides and fixation points were approximately placed according to height and distances for the considered sedan vehicle.

In the case of the LBB system, the lap belt portion of the VSB has been upgraded to include 3 lengths of two-dimensional elements allowing the restraint of the LBB by the VSB.

2.2. Boundary Conditions. The initial speed of the system is 13.34 m/s along the "x" axis. In the "y" direction corresponding with the vehicle vertical direction, the only force acting is gravity ("−y" axis), with a constant value of 0.00981 mm/ms^2 . The deceleration curves in the "x" direction are taken from FMVSS regulation and are introduced in the software.

Contact boundary conditions were selected as automatic in the software for explicit simulations. In the tangential direction to the plane of the contact, the resulting stresses are due to friction between parts, and the stresses are defined by static and dynamic friction coefficients of 0.3 and 0.2, respectively [19]. The nodal elements (foam-LBB) were linked for them to behave like one body.

3. Results

Numerical simulations were performed in a range of 120 ms , recording results every 20 ms (Figure 4). In the next paragraphs, we present the results for each anatomic part analysed from the dummy (head and chest).

3.1. Head. Figure 5 shows the dummy head resultant acceleration for both LBB and VSB systems, which were obtained by an accelerometer sensor type located in the centre of gravity of the dummy head used in the simulations.

Figure 5 shows that the head resultant acceleration ramps up earlier for the LBB than for the VSB, due to a better connection of the dummy trunk for the LBB than in the case of the VSB. The same tendency can be observed for the

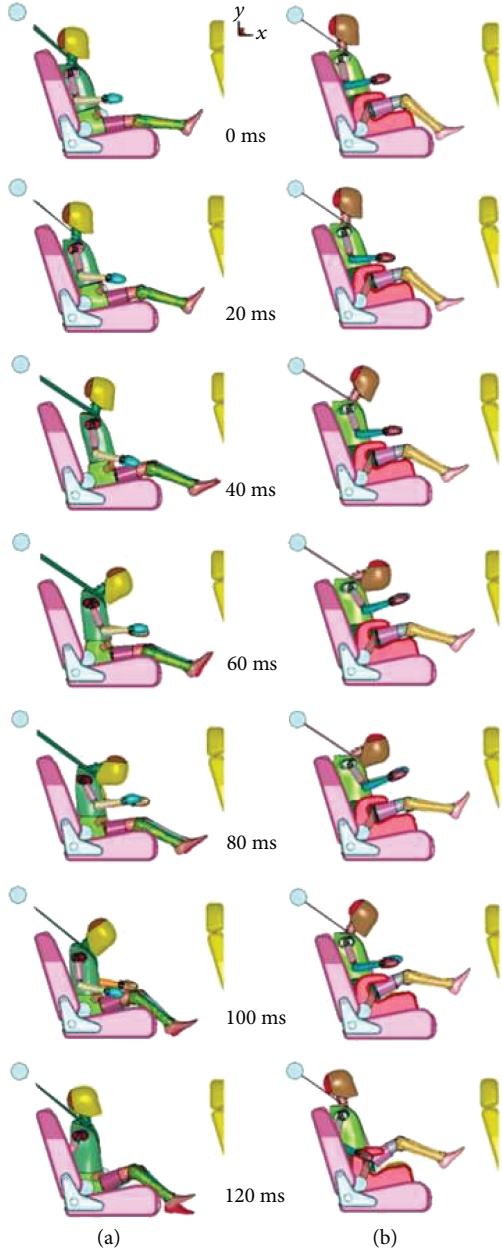


FIGURE 4: Dummy kinematics results: (a) VSB and (b) LBB.

resultant acceleration of the dummy thoracic spine analysed from the latter. This fact allows for a better restraint for the dummy during the earliest stages of the crash producing a wider restraint phase with lower maximum values at the end when the LBB system is used.

The lower value of HIC_{36} is presented for the LBB system, with a value of just 554.3 and a maximum peak head resultant acceleration of 62g, while for the VSB system, the same injury criteria increment is 730.4 and 65g.

3.2. Thorax. The analyses done in Section 3.1 were also reproduced for the chest, by placing the numerical accelerometer in the thoracic spine of the dummy's thorax. The position of the thoracic spine accelerometer in the dummy model replicates the position in the current physical dummy. Although

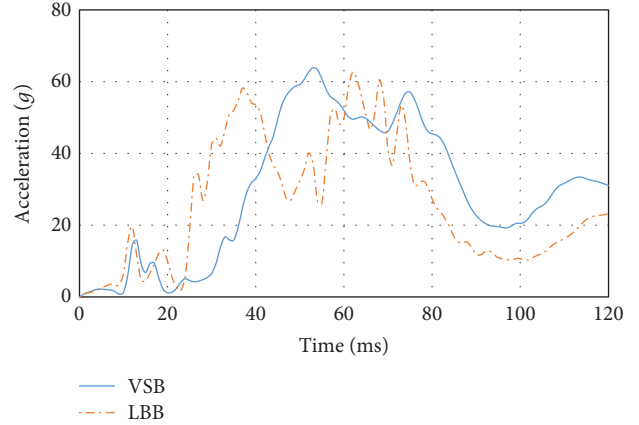


FIGURE 5: Head resultant acceleration.

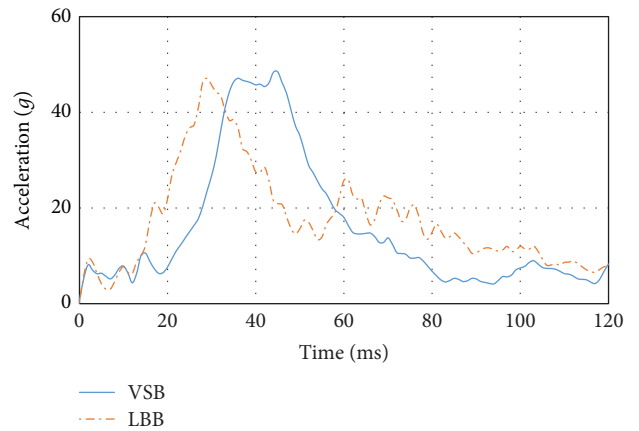


FIGURE 6: Thoracic spine resultant acceleration (g).

the thoracic spine acceleration is not an appropriate parameter to derive injury criteria for the chest, it has been used in this article to obtain references to the thoracic restraint capabilities of systems studied. The resultant thoracic spine deceleration value was obtained in the crash simulation, and later it was used to calculate the CSI. For CSI calculation, the same formula as the one used for the HIC has been employed replacing the head centre of gravity resultant acceleration by the thoracic spine resultant acceleration. Even the 3 ms cumulative resultant thoracic spine acceleration criterion was also obtained as FMVSS 213 was established. Thoracic spine resultant acceleration for both LBB and VSB can be observed in Figure 6.

LBB generated a CSI of 281.9 and a thoracic spine acceleration 3 ms clip of 44.36, while VSB yields to CSI values of 315.5 and thoracic spine acceleration 3 ms clip of 45.23, respectively. The area under the curves displayed in Figure 6, between 20g and 40g, shows an indication of the energy absorbed by the dummy trunk. It can be observed in the lower area for the LBB system compared to the VSB system. This fact produces a better restraint for the dummy pelvis area of the LBB system and includes the thoracic spine because the pelvis is linked to the lower portion of the thoracic spine through the lumbar spine.

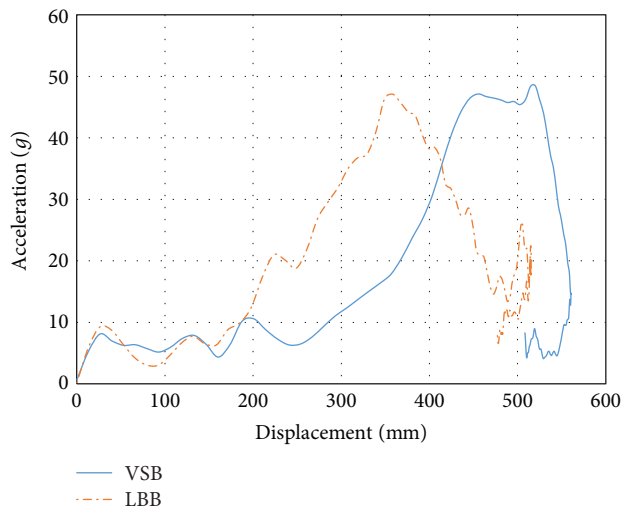


FIGURE 7: Effectiveness of the LBB and VSB restraint.

Figure 7 shows a comparison of the longitudinal acceleration of the chest in the two tests. The maximum thoracic spine displacement of LBB is lower than VSB and the highest energy absorption was generated in the last 300 mm.

4. Discussion

To validate the numerical analyses herein performed, a comparison of the peak values of the obtained uniaxial decelerations of the head and thorax, for the HIC_{36} and for the thoracic spine acceleration 3 ms clip, with experimental tests, is shown in Table 1 [12].

In Table 1, the HIC_{36} results approximate the experimental results with an error of less than 7.7% in the worst case. Also, it can be inferred that the principal reason for this error is because of the difference in dimension, geometry, and mass in the experimental and numerical seats that were used in this study. Likewise, in both restraint systems analysed, a higher HIC_{36} is generated when VSB is implemented with respect to the use of the LBB system.

5. Conclusion

The LBB system generates the smallest HIC_{36} , because the belt properly holds the dummy when its sitting height increases, properly fastening the belt over the children’s shoulder and pelvic area. This allows a child to benefit from the protection provided by three-point seat belts in frontal impacts by properly distributing the loads on the pelvis, thorax, and the shoulder during a frontal crash. Likewise, this reduces the risk of child movement by inertial force and the seat belt forces over the trunk are lower, reducing the neck moment, decreasing the HIC.

In this study, the best protection level obtained with the LBB system is based on two fundamental factors: a good anchorage behaviour to the vehicle and the improvement of the fit of the seat belt on both the pelvic and shoulder area of the child.

TABLE 1: Comparison of numerical and experimental results.

Numerical results		
Test 1		
$HIC_{36} = 730.43$	$TSA_{3MSC} = 45.23g$	
$H_{Ax} = 58$	$H_{Ay} = 51$	$H_{Az} = 7.4$
$TS_{Ax} = 46$	$TS_{Ay} = 10$	$TS_{Az} = 6$
Test 2		
$HIC_{36} = 554.3$	$TSA_{3MSC} = 44.36g$	
$H_{Ax} = 46$	$H_{Ay} = 53$	$H_{Az} = 15$
$TS_{Ax} = 45$	$TS_{Ay} = 12$	$TS_{Az} = 6.5$
Experimental results by Hagedorn and Stammen [12]		
Test 10		
$HIC_{36} = 801$	$TSA_{3MSC} = 44.3g$	
$H_{Ax} = 65$	$H_{Ay} = 51$	$H_{Az} = 6.5$
$TS_{Ax} = 40$	$TS_{Ay} = 20$	$TS_{Az} = 14$
Test 6		
$HIC_{36} = 594$	$TSA_{3MSC} = 50.8g$	
$H_{Ax} = 51$	$H_{Ay} = 47$	$H_{Az} = 7$
$TS_{Ax} = 50$	$TS_{Ay} = 17$	$TS_{Az} = 5$

H_{Ax} , head acceleration axis x; H_{Ay} , head acceleration axis y vertical; H_{Az} , head acceleration axis z; TS_{Ax} , thoracic spine acceleration axis x; TS_{Ay} , thoracic spine acceleration axis y vertical; and TS_{Az} , thoracic spine acceleration axis z.

There is, indeed, a clear need to improve a booster seat design to achieve higher levels of protection for children between 4 and 8 years old during frontal impacts. This could be through the usage of a fully rigid anchorage system and the adjustable height of the LBB system to allow the seat belt of the vehicle to fit properly to the child depending on his age and anthropometry.

Due to the high cost and time involved in developing the experimental tests herein presented, it is feasible to perform them numerically in order to simulate nonlinear physical phenomena, in order to obtain approximate values with respect to the experimental tests, allowing the minimisation of costs. Numerical tests also offer the possibility of modifying variables to carry out new analyses. In addition, numerical tests also allow simulating side and rear impact scenarios with the LBB.

Data Availability

The data used to support the findings of this study are available from the corresponding author upon request.

Conflicts of Interest

The authors declare that they have no conflicts of interest.

Acknowledgments

The authors acknowledge partial financial support from the Mexican Government through Consejo Nacional de Ciencia y Tecnología and Instituto Politécnico Nacional, as well as the participation of the biomechanics group of INSIA

incorporated into the Universidad Politécnica de Madrid, from Spain. The authors also thank the support of projects 1931 and 20181141, as well as an EDI grant, all by SIP/IPN.

References

- [1] M. Peden, K. Oyegbite, J. Ozanne-Smith et al., *Informe Mundial Sobre Prevención de las Lesiones en los Niños*, UNICEF OMS, 2012.
- [2] Observatorio Nacional de Lesiones (ONL), *Principales Indicadores de Resultados en Seguridad Vial*, ST del CONAPRA INEGI, Mexico, 2011.
- [3] Instituto Nacional de Estadística y Geografía (INEGI), *Perfil Estatal Distrito Federal*, Base de defunciones, 2011.
- [4] M. Huntley, *Federal Motor Vehicle Safety Standard No. 213 Child Restraint Systems*, National Highway Traffic Safety Administration. US Department of Transportation, 2002.
- [5] B. A. A. García, E. G. Sandoval, A. A. R. Sánchez, and P. C. González, “Valor pronóstico de las lesiones secundarias de esguince cervical diagnosticadas por resonancia magnética,” *Revista mexicana de medicina física y rehabilitación*, vol. 14, no. 1, pp. 20–25, 2002.
- [6] C. J. Denholm and J. T. Denholm, “The impact of trauma and critical care: reflections from a practitioner and a patient,” *Critical Care and Resuscitation*, vol. 11, no. 2, pp. 85–120, 2009.
- [7] M. Y. Svensson, O. Boström, J. Davidsson et al., “Neck injuries in car collisions—a review covering a possible injury mechanism and the development of a new rear-impact dummy,” *Accident Analysis & Prevention*, vol. 32, no. 2, pp. 167–175, 2000.
- [8] L. Obergefell, A. Rizer, and L. Rogers, *Biodynamic Modeling and Simulation of the Ejection Seat/Occupant System (No. AFRL-HE-WP-TR-2000-0080)*, Veridian Engineering, Dayton OH, USA, 2000.
- [9] G. Maudes, *Influencia de la Defensa de un Todoterreno en las Lesiones Sufridas por un Peatón en Caso de Atropello*, Universidad Carlos III De Madrid, 2010.
- [10] H. Zarei, *Experimental and Numerical Investigation of Crash Structures Using Aluminum Alloys*, Cuviller Verlag, 2008.
- [11] American Academy of Pediatrics, “CPS Issue Report,” September 2004, <http://www.aap.org/healthtopics/carseatsafety.cfm>.
- [12] A. Hagedorn and J. Stammen, *Comparative Evaluation of 6-Year-Old Hybrid III and DAPRR Prototype ATD Abdomen/Pelvis Components. (Report No. DOT HS 812 088)*, National Highway Traffic Safety Administration, Washington, DC, USA, 2015.
- [13] M. Arienti, P. Hung, E. Morano, and J. E. Shepherd, “A level set approach to Eulerian-Lagrangian coupling,” *Journal of Computational Physics*, vol. 185, no. 1, pp. 213–251, 2003.
- [14] W. D. Callister, *Introducción a la Ciencia e Ingeniería de los Materiales*, vol. 1, Reverté, 2002.
- [15] Y. Y. Tay, C. S. Lim, and H. M. Lankarani, “A finite element analysis of high-energy absorption cellular materials in enhancing passive safety of road vehicles in side-impact accidents,” *International Journal of Crashworthiness*, vol. 19, no. 3, pp. 288–300, 2014.
- [16] N. E. Dhole, *Development and Validation of a Finite Element Model of a Transport Aircraft Seat Under Part 25.562 Dynamic Test Conditions [Ph.D. thesis]*, University of Pune, 2010.
- [17] A. A. Carrero, *Simulación de un Choque Lateral con Dummy con Cinturón Mediante LS-DYNA*, Universidad Carlos III de Madrid, 2011.
- [18] N. E. Dhole, V. Yadav, and G. Olivares, “Certification by analysis of a typical aircraft seat,” in *National Institute for Aviation Research*, pp. 1–12, Wichita, KS, USA, 2012.
- [19] A. Gavelin, M. Lindquist, and M. Oldenburg, “Modelling and simulation of seat-integrated safety belts including studies of pelvis and torso responses in frontal crashes,” *International Journal of Crashworthiness*, vol. 12, no. 4, pp. 367–379, 2007.

Research Article

Numerical Analysis of Occupant Head Injuries in Impacts with Dump Truck Panel

Shence Wang , Deshun Liu, and Zhihua Cai 

School of Electromechanical Engineering, Hunan University of Science and Technology, Xiangtan 411201, China

Correspondence should be addressed to Shence Wang; scwang@hnust.edu.cn

Received 19 December 2017; Revised 11 April 2018; Accepted 19 April 2018; Published 3 June 2018

Academic Editor: Tatsuo Yoshino

Copyright © 2018 Shence Wang et al. This is an open access article distributed under the Creative Commons Attribution License, which permits unrestricted use, distribution, and reproduction in any medium, provided the original work is properly cited.

The human head will inevitably impact on the panel causing injury due to the inertia during dump truck collisions or emergency braking. Therefore, this paper aims to analyze the effects of panel design parameters on occupant head injuries via simulations using finite element (FE) models of a human head and a dump truck cockpit. Special focus was applied to understand how panel type (soft and hard), elastic modulus of the filling and frame, and the fixing distance for the soft panel could affect head injuries in head-to-panel impacts under different impact conditions (impact speed and location). Simulation results show that a soft panel is beneficial for head protection in impacts with the truck instrument panel, and a soft panel using a lower filling elastic modulus, lower frame elastic modulus, and longer fixing distance is helpful for head injury prevention. The findings also indicate that the head peak acceleration and maximum skull stress are more sensitive to the fixing distance and elastic modulus of frame than elastic modulus of the filling of the panel. Moreover, these trends are not affected by changing the impact speed and impact location. The findings of this study suggest that a safer panel design for head injury prevention should firstly have a long fixing distance and then followed by using softer filling and frame materials.

1. Introduction

The dump truck is widely used for transportation of large-scale metal mines, coal mines, water resources, and so on with high efficiency and loading capability. However, the safety of dump truck is particularly an important issue due to the complex workplace. Impacts between the head and instrument panel in a condition of truck collision or emergency braking generally lead to greater threat to the lives of the occupant of a dump truck. Therefore, the safety of the panel has become important for vehicle design.

At present, the study of the panel is mainly based on the United Nations Economic Commission for Europe Regulation number 21 (ECE R21 [1]). In this regulation, the head is simplified to a solid model with a rigid material body and a vinyl nonlinear material skin, and then they are bonded together as the impactor. In the tests, the diameter of the head form is 165 mm, the mass for the impactor is 6.8 kg, and the impact speed is 24.1 km/h. The ECE R21 requires

that the measured acceleration response of the head form under the prescribed test condition should not exceed 80 g continuously for more than 3 ms. Physical impact test using head form is an important method for study of panel safety design. Liu et al. obtained spherical head model acceleration changes based on impact tests of head form and gravity impactor with a panel [2]. However, physical impact test is not the optimal approach for study of panel design since it is difficult to control the factors around the period of the tests and the parameters about the impact test are inconvenient to change. Moreover, the circle of the physical impact test is long and the cost is high. Therefore, numerical simulations using the head form and car models were widely used for panel safety design. Haniffah et al. ascertained the appropriate material of the panel according to the rules of the head form stress changing predicted from simulations [3]. Zhao and Zhao [4] and Bao and Qi-ming [5] optimized the panel by changing panel attribute parameters to reduce head acceleration based on simulations. However, previous studies on

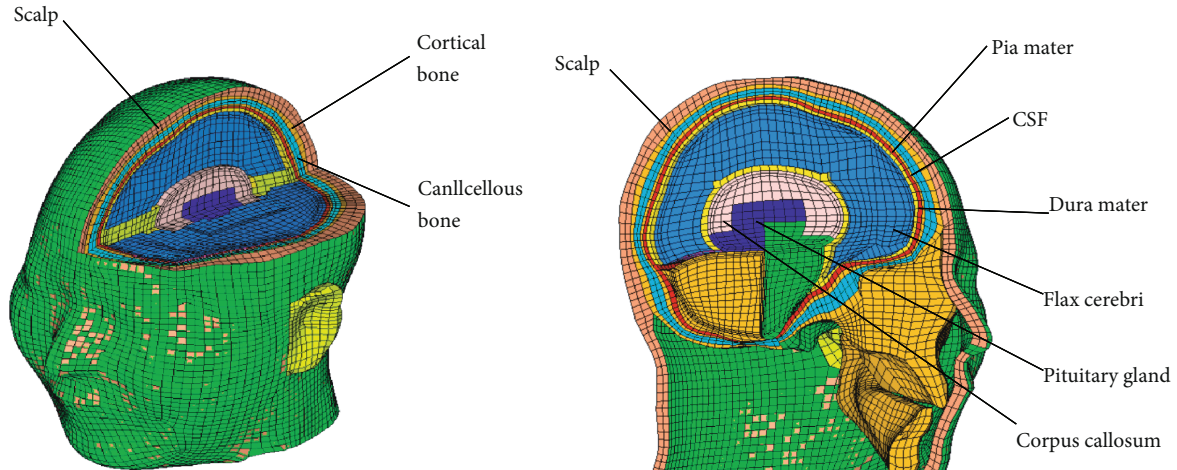


FIGURE 1: The FE model of the head.

TABLE 1: Materials of bones [6–8].

Material	Density (g/cm ³)	Young's modulus (GPa)	Poisson's ratio	Shear modulus (GPa)	Hardening parameter	Cowper-Symonds model		Molding failure strain (%)
						C	P	
Cranial cortical bone	2.0	11.5	0.3	1.15	0.1	2.5	7	0.02
Cancellous bone of skull	1.0	0.04	0.45	0.001	0.1	2.5	7	0.03
Bone of cortical bone	5	21	0.23	1.15	0.1	2.5	7	0.02
Cancellous bone of facial bone	1	0.04	0.45	0.01	0.1	2.5	7	0.03
Mandibular cortical bone	2	11.5	0.3	1.15	.1	2.5	7	0.02
Mandibular cancellous bone	1	0.04	0.45	0.01	0.1	2.5	7	0.03

TABLE 2: Head soft tissue material parameters.

Head component	Density, ρ (kg/m ³)	Young's modulus (MPa)	Poisson's ratio	G_0 (kPa)	G_{∞} (kPa)	β (s ⁻¹)	Bulk modulus (MPa)	Reference
Scalp	1000	16.7	0.42					[9]
Dural	1130	31.5	0.23					[9]
Pia mater	1130	11.5	0.45					[9]
CSF cerebrospinal fluid	1050			100	20	100	4.97	[9]
Brain	1040			1.66	0.928	16.95	557	[10]
Cerebellum	1040			1.66	0.928	16.95	557	[10]
Brainstem	1040			1.66	0.928	16.95	557	[10]
Corpus callosum	1140	31.5	0.45					[11]
Sickle	1140	31.5	0.45					[11]
Pituitary/ventricles	1140	31.5	0.45					[11]

panel safety design were mainly based on head form as mentioned above, which cannot predict the biomechanical response of human head in the collisions.

The purpose of this study is therefore to analyze the effects of different panel design parameters on occupant head injury using a more accurate human head model via finite

element (FE) simulations. In particular, the design parameters of the panel type, filling elastic modulus, frame elastic modulus, and length of panel were considered. This work will provide important data for the design of truck panel with the purpose of reducing occupant head injuries in the complex workplace [16–18].



FIGURE 2: The FE model of the dump truck.

2. Materials and Methods

2.1. Head FE Model. The head FE model was extracted from a whole body model which was developed and used to study the chest injury during impacts in different directions [12]. The head model was then improved and validated by Mao et al. in a later study [13], see Figure 1. The validation study mainly focused on evaluating the biomechanical response of the head model under loading conditions of drop and blunt impact at different speeds comparing with cadaver test data from Yoganandan et al. [14, 15], and the validation results show good agreement with the experiments [13]. Thus, the head FE model is reliable for analysis in the current study.

The brain is a soft biological organ with high water content (close to 80%). It shows incompressibility, nonlinearity, anisotropy, and viscoelasticity. Thus, the *MAT_VISCOELASTIC (6# material in LS-DNYA) was selected. Plenty of brain tissue experiments show that the deformation of the brain tissue depends on its shear modulus, so its formula is as follows:

$$G(t) = G_0 + (G_\infty - G_0)e^{-\beta t}, \quad (1)$$

where G_0 is short-term shear modulus, G_∞ is long-term shear modulus, and β is decay coefficient. The material parameters used for the head model components are given in Tables 1 and 2.

2.2. Dump Truck Cockpit FE Model. The FE model of a dump truck cockpit was developed using a finite element preprocessing software HyperMesh. It consists of the truck framework, seat, panel, and other structures in the cockpit, see

TABLE 3: The materials defined for dump truck frame and panel [4].

Structure	Material	Young's modulus (MPa)	Poisson's ratio	Density, ρ (kg/m ³)
Framework	DC01	2.1×10^5	0.28	7.85×10^3
Hard panel	PC	2400	0.35	1007
Soft panel				
Skin	PVC	2400	0.35	1350
Frame	ABS	3400	0.35	1007
Filling	PUR	20.0	0.01	140

Figure 2. The dump truck cockpit FE model includes 1513114 nodes and 1505251 elements.

Two panel types (soft panel and hard panel) are usually used in dump trucks. Soft panels are mainly made up of polyvinyl chloride (PVC) and polycarbonate (ABS), while hard panels are usually made of plastics. For the soft panel, ABS and PVC materials are usually used in the skin and frame, and the polyurethane (PUR) material is chosen as the filling layer to reduce the stiffness of the panel. Table 3 shows the materials for the truck framework and the panel, where the DC01 low carbon steel was selected to model the frame of dump truck and the material models for the soft and hard panel were defined, respectively. The data in Table 3 were extracted from a previous study of head-to-panel impacts [4].

2.3. Setup of Impact Simulations

2.3.1. Impact Location and Impact Speed. The impact location should cover the high aggressive structures in the panel, including the fragile places and high stiffness structures.

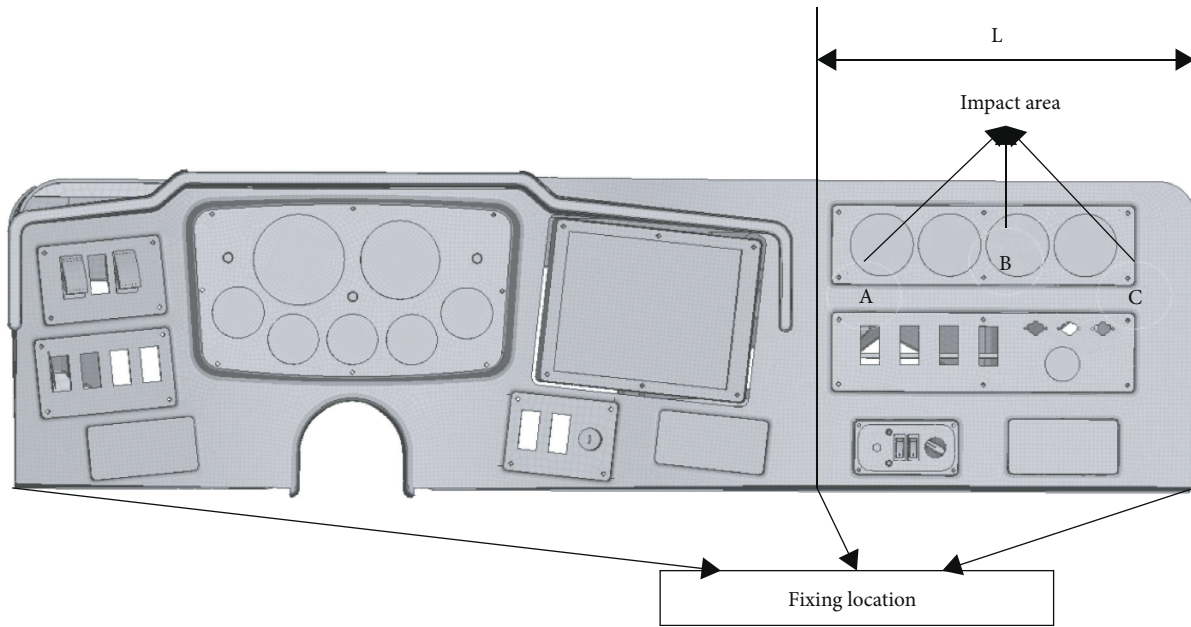


FIGURE 3: Impact area.

According to this principle, the impact locations in the panel were chosen as shown in Figure 3. The selection of the impact location is also to consider the potential contact locations of the occupant during operation.

The working speed of the dump truck usually does not exceed 40 km/h due to the terrible working environment. Therefore, the speeds of 10 km/h, 24.1 km/h, 32 km/h, and 40 km/h were used in this study with a combining consideration of the impact speed required by ECE R21 (24.1 km/h).

2.3.2. Parametric Study. Table 4 shows the information for different parametric studies. Firstly, a parametric study was carried out on the influence of the panel type (soft versus hard) on head injuries by comparing the results from the impact simulation of a soft instrument board with that from a hard panel. Then the effects of filling elastic modulus (filling E: 200 versus 20 MPa), frame elastic modulus (frame E: 0.34 versus 3.4 GPa), and fixing distance (L: 450 versus 550 versus 650 mm, see Figure 3) in the soft panel on head injuries were analyzed, respectively.

For the parametric study of softer panel design parameters, either different impact speeds (10 km/h, 24.1 km/h, 32 km/h, and 40 km/h) or different impact locations (A, B, and C) were used to consider the working environment of the dump truck. For the impact speed changing case impact, location B was selected to cover the main impact area (front of the occupant). While for the impact location changing case, impact speed of 24.1 km/h was used to take the requirement of ECE R21 (the only regulation for panel safety design) into consideration. The combinations of impact speed and location were not considered to reduce the computational time, and the increase of impact speed generally leads to a worse situation.

3. Results

3.1. Effects of Panel Type on Head Injury. The simulation results for different panel type are shown in Figure 4, including the time-acceleration curve and skull stress nephogram. The results show that the maximum acceleration of the head is 97 g (near 9.5 ms) for the hard panel, and the time range for head acceleration above 80 g in the hard panel case is from 7.6 ms to 13 ms (the peak width = 5.4 ms), see Figure 4(a). Both the peak value and duration time exceed the requirements in the ECE R21, where a maximum head acceleration of 80 g and a duration time of 3 ms are limited. However, for the soft panel, the maximum acceleration of the head is 72 g (at 7.4 ms), which meets the requirement of ECE R21. Similarly, the maximum stress of the skull for the impact with the hard panel (100 MPa) is significantly higher than that for the soft panel (75 MPa), and the peak stress area for the hard panel case is also obviously wider than that for the impact with the soft panel.

3.2. Effects of Soft Panel Design Parameters on Head Injury at Different Impact Speeds. Figure 5 shows the head acceleration curves for simulations of head-to-soft panel impact using different design parameters at different speeds. As shown in this figure, the peak acceleration values of head for the cases of filling elastic modules of 20 MPa are significantly lower than those for the cases of using a filling elastic modules of 200 MPa (#1 versus #4: 50 g versus 52 g, 64 g versus 71 g, 70 g versus 74 g, and 75 g versus 78 g for 10 km/h, 24.1 km/h, 32 km/h, and 40 km/h, resp.), when keeping other design parameters at the same level. The maximum head acceleration for the impacts with a panel using a frame elastic modules of 0.34 GPa (#2: 63 g, 48 g, 67 g, and 69 g) are also obviously lower than those for a stiffer frame with elastic modules of 3.4 GPa (#2 versus #3: 48 g versus 53 g, 63 g versus

TABLE 4: The properties of the panel for different parametric studies.

Parametric study	Filling	Frame	L	Speed (km/h)	Location
Panel type	Soft versus hard (see Table 3 for material parameters)		450 mm	24.1	B
Filling elastic modulus	200 versus 20 MPa	0.34 GPa	450 mm	10, 24.1, 32, and 40 at B	A, B, and C at 24.1 km/h
Frame elastic modulus	200 MPa	0.34 versus 3.4 GPa	550 mm		
Support position	200 MPa	0.34 GPa	450 versus 550 versus 650 mm		

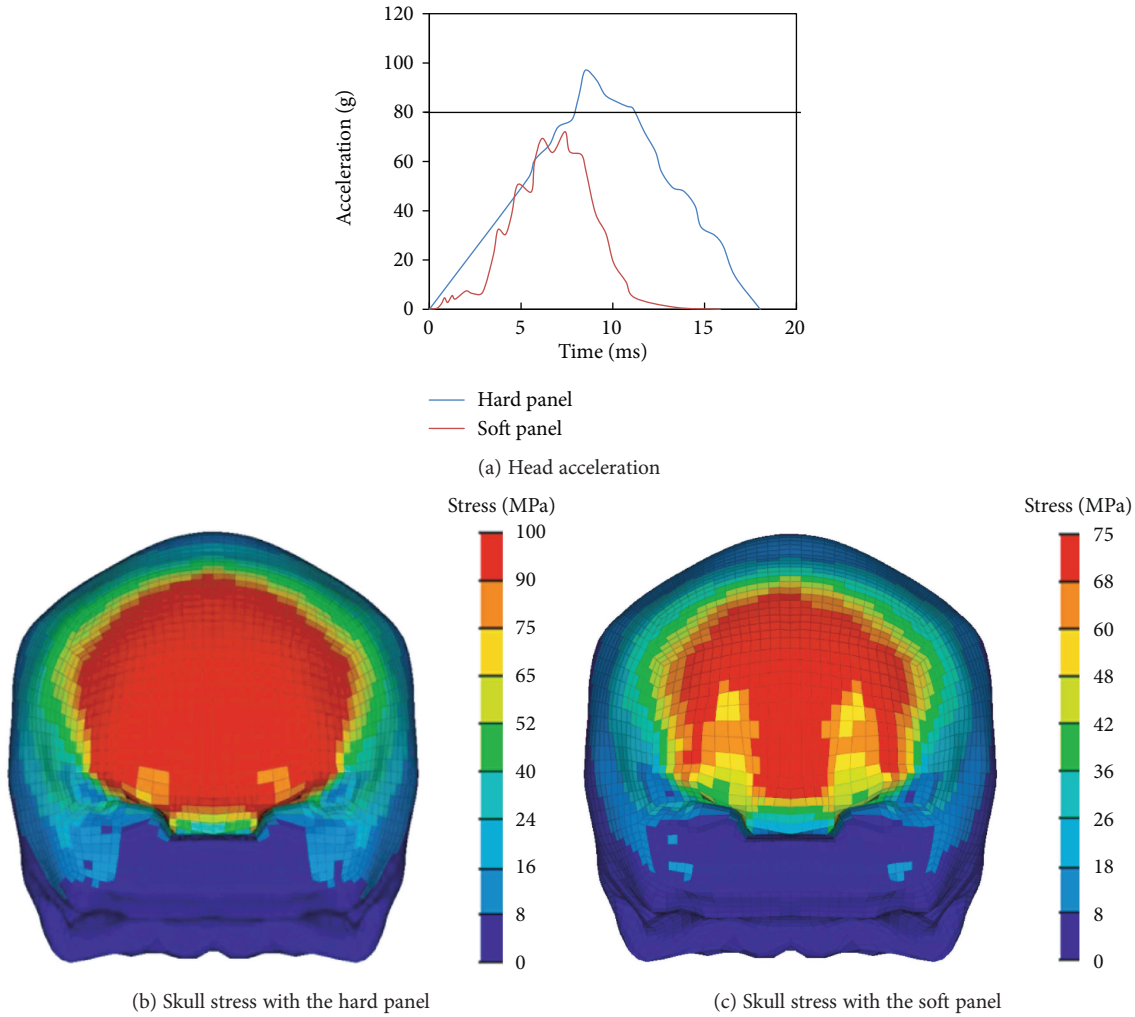


FIGURE 4: The simulation results for the hard and soft instrument panel.

72 g, 67 g versus 82 g and 69 g versus 89 g for 10 km/h, 24.1 km/h, 32 km/h, and 40 km/h, resp.), again other design parameters were controlled. For different fixing distances (controlling other parameters), the results show that the head peak acceleration values for the cases of 450 mm are the highest, followed by the cases of 550 mm and 650 mm (#4 versus #2 versus #5: 52 g versus 48 g versus 37 g, 71 g versus 63 g versus 42 g, 74 g versus 67 g versus 48 g, and 78 g versus 69 g versus 51 g for 10 km/h, 24.1 km/h, 32 km/h, and 40 km/h, resp.).

Figure 6 shows an example for the distribution of skull stress at the time point where the maximum stress occurred. These results show that the maximum stress value of the skull

for the case using a filling elastic modulus of 20 MPa is slightly lower than that for the case with a filling elastic modulus of 200 MPa when controlling other parameters. The peak skull stress area for the 20 MPa filling elastic modulus case is also smaller than the 200 MPa case. However, significant differences in maximum skull stress and its area were observed between the cases using a frame elastic modulus of 0.34 GPa and 3.4 GPa, where the maximum skull stress for the former is 15 MPa (Figure 6(b)) and 65 MPa (Figure 6(c)) for the latter. The maximum skull stress for the fixing distance of 450 mm, 550 mm, and 650 mm are 20 MPa (Figure 6(d)), 15 MPa (Figure 6(b)), and 3 MPa

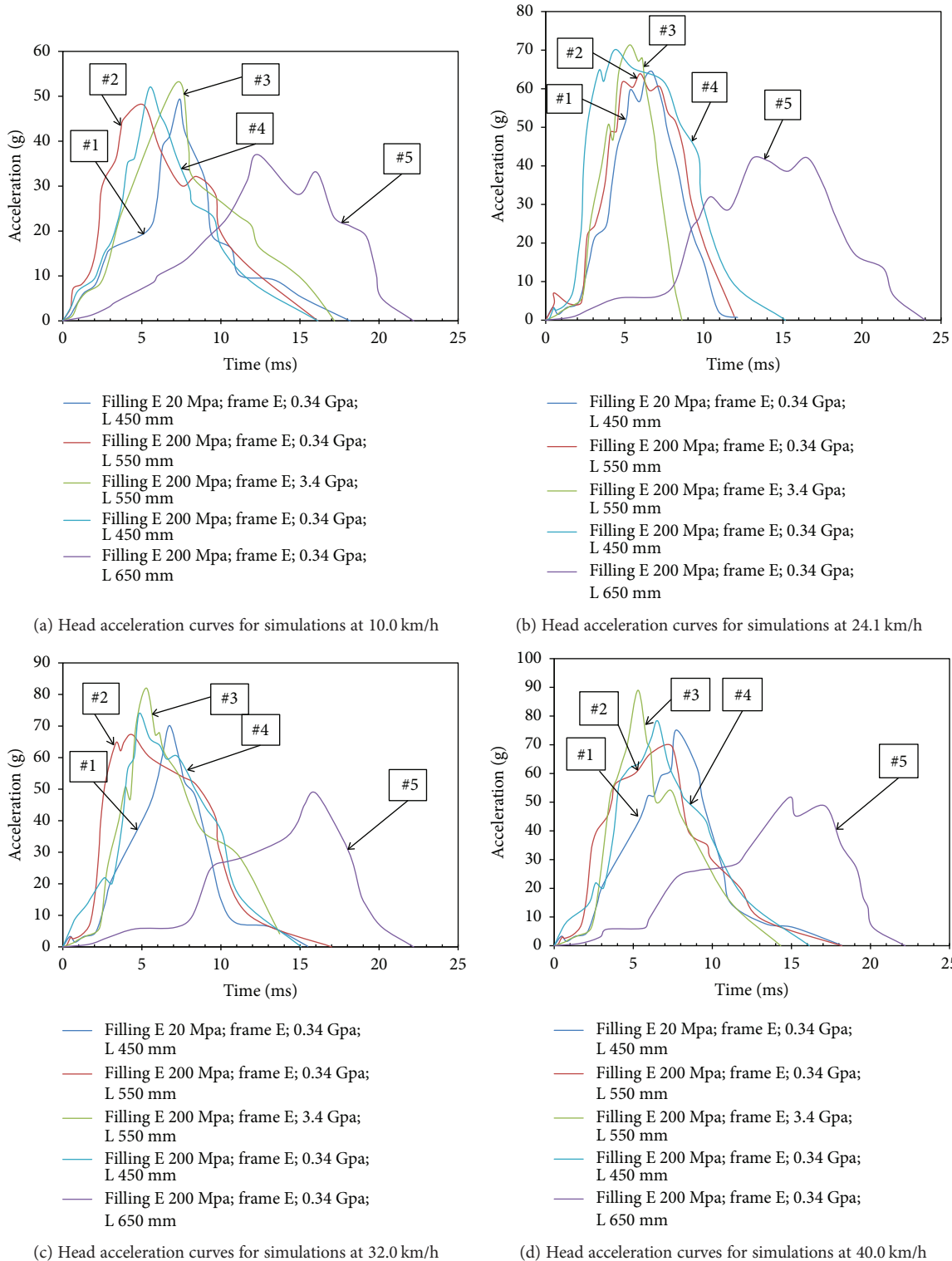


FIGURE 5: Head acceleration curves for simulations using different design parameters.

(Figure 6(e)), respectively. The case of 650 mm has the smallest peak stress area in the skull comparing to another two cases.

The stress distributions for the speeds of 10 km/h, 32 km/h, and 40 km/h are not shown here, but the similar (to the

24.1 km/h case) trend of the maximum stress as a function of changing the magnitude of a given design parameter was observed for other impact speeds (Figure 7). The data in Figure 7 also show that the maximum skull stress increases with increasing impact speed.

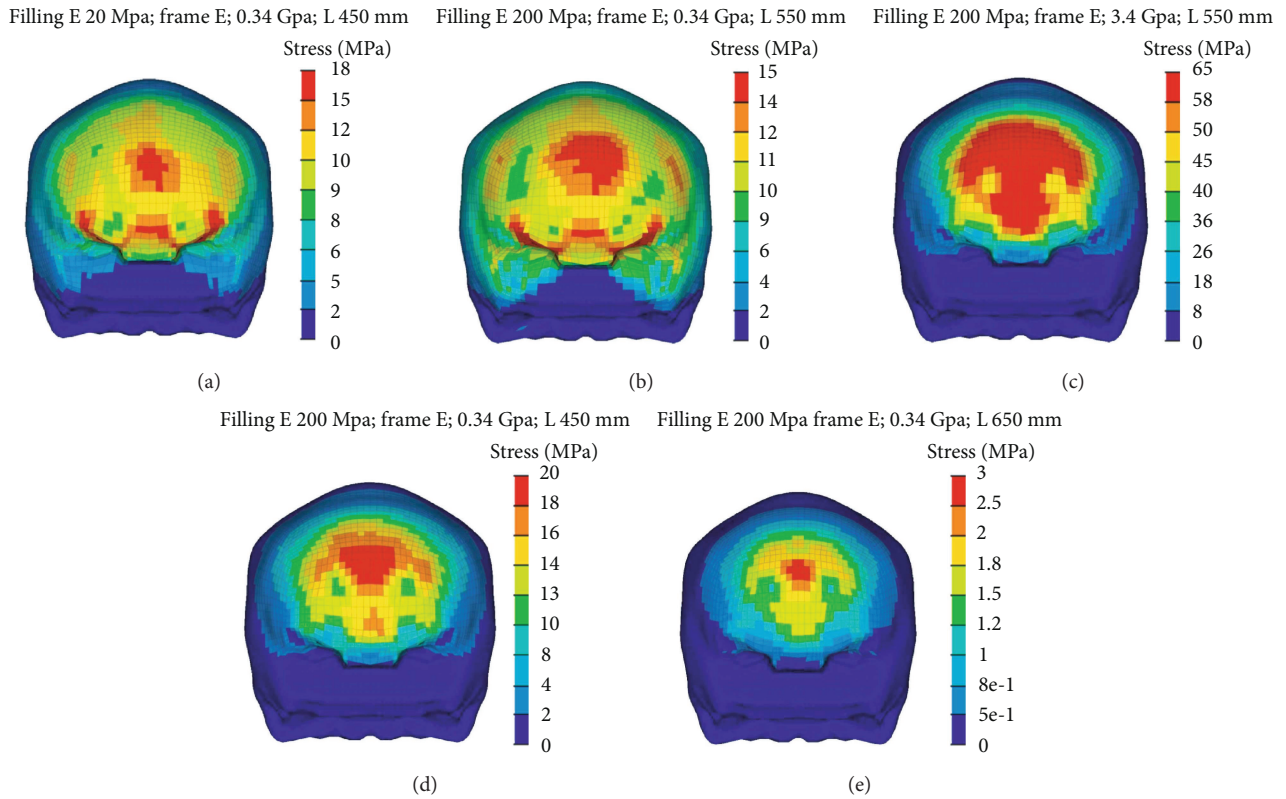


FIGURE 6: Skull stress for simulations at 24.1 km/h.

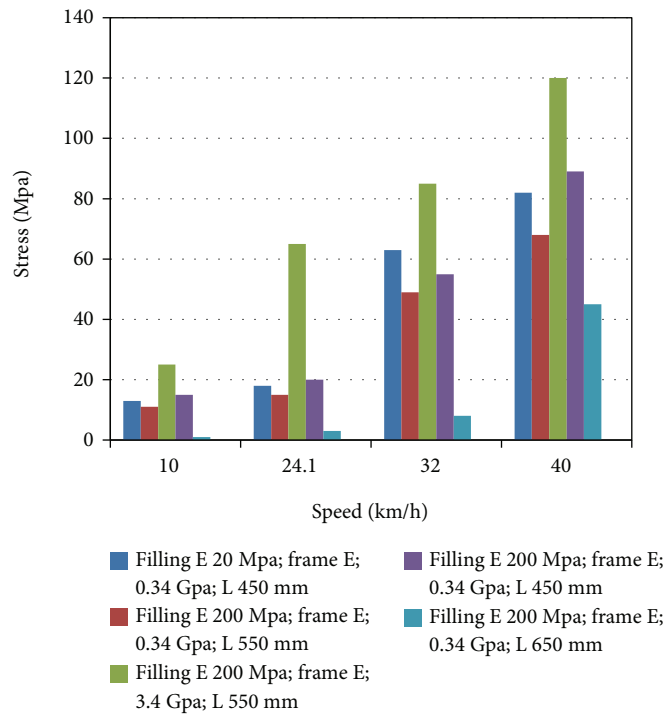


FIGURE 7: The peak value of the skull for simulations at different speed.

3.3. Effects of Soft Panel Design Parameters on Head Injury at Different Impact Locations. Figures 8 and 9 show the predicted head acceleration time history curves and the

maximum skull stress values for the simulations using different design parameters at different peak impact locations. It is clear from these data that both peak head acceleration and

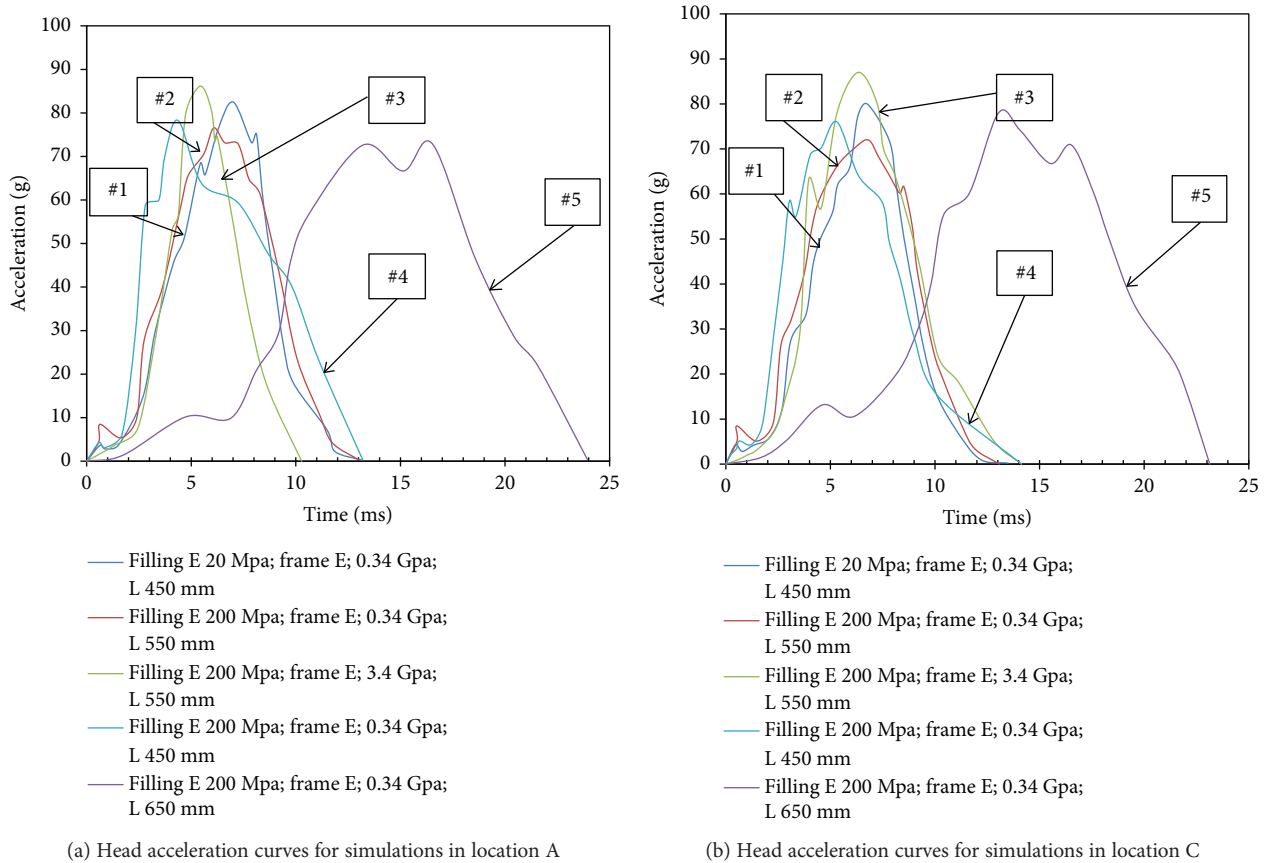


FIGURE 8: Head acceleration curves for simulations in different locations.

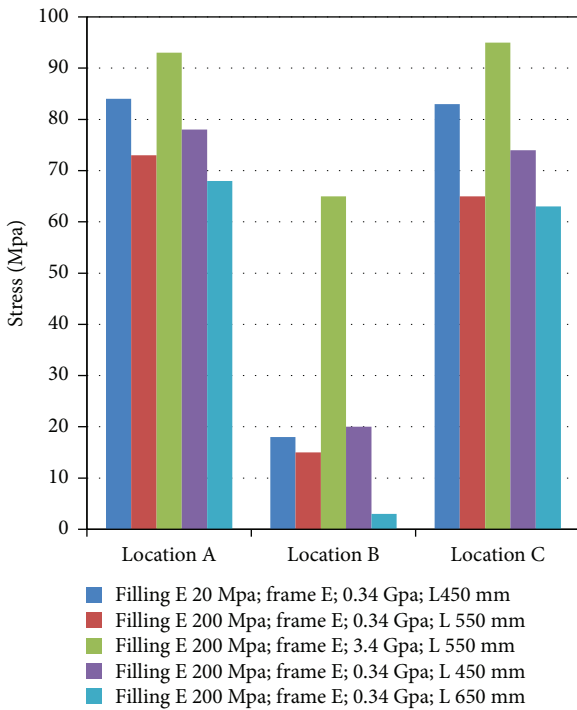


FIGURE 9: Skull stress of the simulation in location A, B, and C at 24.1 km/h.

maximum skull stress are lower in the cases with a relatively softer panel and longer fixing distances. This trend is constant for all impact locations, which is similar to that observed from changing impact speed.

The simulation results also show that the peak head acceleration values and maximum skull fractures in locations A and C (Figures 8 and 9) are larger than those for the location B (Figures 5(b) and 9).

4. Discussion and Conclusions

The effects of different panel type and design parameters of the soft panel on head injury index of peak acceleration and maximum skull stress in head-to-truck panel impacts were predicted using FE simulations. Comparisons of head acceleration and skull stress between hard and soft panel impacts indicate that the soft panel is beneficial for head protection when impacting with a truck instrument panel. This effect is mainly from the generally lower stiffness of the soft panel.

For the detailed analysis of how different design parameters of the soft panel affect head injuries in the head-to-panel impact, the results indicate that a lower filling elastic modulus, lower frame elastic modulus, and longer fixing distance are helpful for head injury prevention in head-to-panel impacts. Moreover, the above trends are not affected by changing the impact location and speed to some extent.

The results also suggest that the head peak acceleration and maximum skull stress are more sensitive to the fixing distance than elastic modulus of the filling. This is mainly due to the fact that increasing the fixing distance leads to a significant increase of panel deformation in the head-to-panel impact, which absorbed lot impact energy for head protection. While the differences in panel deformation from changing filling and frame elastic modulus are smaller than that from the change of fixing distance. Therefore, a safer panel design for head injury prevention is firstly suggested to have a long fixing distance and then followed by using softer filling and frame materials.

Conflicts of Interest

The authors declare that they have no conflicts of the interest.

Acknowledgments

The authors acknowledge the support from the National Natural Science Foundation of China (51779092), the Research Foundation of Education Bureau of Hunan Province, China (16C0651), the China Postdoctoral Science Foundation funded project (2016M592421), and the Educational Commission of Hunan Province of China (17A068).

References

- [1] United Nations Economic Commission for Europe Regulation No. 21, *Uniform Provisions Concerning the Approval of Vehicles with regard to Their Interior Fittings*, 2003.
- [2] C. H. Liu, Y. C. Lai, C. H. Chiu, and M. H. Lin, "Interior head impact analysis of automotive instrument panel for unrestrained front seat passengers," *Key Engineering Materials*, vol. 715, pp. 186–191, 2016.
- [3] N. A. Haniffah, M. F. Zakaria, and T. K. Sheng, "Design and analysis of automotive instrument panel," *Advanced Materials Research*, vol. 980, pp. 263–268, 2014.
- [4] L. Zhao and G. Zhao, "Simulation of human head damage caused by crash between head and automobile panel," *Transactions of the Chinese Society of Agricultural Machinery*, vol. 36, no. 3, pp. 22–26, 2005.
- [5] X. I. Bao and T. A. Qi-ming, "Head-Impact Simulation Analysis and Research of the Automobile Instrument Panel," *Journal of Anqing Teachers College*, vol. 3, 2012.
- [6] D. Sahoo, C. Deck, N. Yoganandan, and R. Willinger, "Influence of head mass on temporo-parietal skull impact using finite element modeling," *Medical & Biological Engineering & Computing*, vol. 53, no. 9, pp. 869–878, 2015.
- [7] Z. Asgharpour, D. Baumgartner, R. Willinger, M. Graw, and S. Peldschus, "The validation and application of a finite element human head model for frontal skull fracture analysis," *Journal of the Mechanical Behavior of Biomedical Materials*, vol. 33, pp. 16–23, 2014.
- [8] H. Mao, L. Zhang, B. Jiang et al., "Development of a finite element human head model partially validated with thirty five experimental cases," *Journal of Biomechanical Engineering*, vol. 135, no. 11, article 111002, 2013.
- [9] T. J. Horgan and M. D. Gilchrist, "The creation of three-dimensional finite element models for simulating head impact biomechanics," *International Journal of Crashworthiness*, vol. 8, no. 4, pp. 353–366, 2003.
- [10] E. G. Takhounts, S. A. Ridella, V. Hasija et al., "Investigation of traumatic brain injuries using the next generation of simulated injury monitor (SIMon) finite element head model," *Stapp Car Crash Journal*, vol. 52, pp. 1–31, 2008.
- [11] Z. S. Liu, X. Y. Luo, H. P. Lee, and C. Lu, "Snoring source identification and snoring noise prediction," *Journal of Biomechanics*, vol. 40, no. 4, pp. 861–870, 2007.
- [12] Z. Cai, Z. Li, L. Wang, H. Hsu, Z. Xiao, and C. J. Xian, "A three-dimensional finite element modelling of human chest injury following front or side impact loading," *Journal of Vibroengineering*, vol. 18, no. 1, pp. 539–550, 2016.
- [13] Z. Y. Mao et al., "The simulation analysis on biomechanical responses of human head under different loading conditions," *Journal Medical Biomechanics*, vol. 31, no. 6, pp. 532–539, 2016.
- [14] N. Yoganandan, F. A. Pintar, A. Sances Jr. et al., "Biomechanics of skull fracture," *Journal of Neurotrauma*, vol. 12, no. 4, pp. 659–668, 1995.
- [15] N. Yoganandan, J. Zhang, and F. A. Pintar, "Force and acceleration corridors from lateral head impact," *Traffic Injury Prevention*, vol. 5, no. 4, pp. 368–373, 2004.
- [16] X. Deng, S. Potula, H. Grewal, K. N. Solanki, M. A. Tschopp, and M. F. Horstemeyer, "Finite element analysis of occupant head injuries: parametric effects of the side curtain airbag deployment interaction with a dummy head in a side impact crash," *Accident Analysis & Prevention*, vol. 55, pp. 232–241, 2013.
- [17] N. Li, H. Fang, C. Zhang, M. Gutowski, E. Palta, and Q. Wang, "A numerical study of occupant responses and injuries in vehicular crashes into roadside barriers based on finite element simulations," *Advances in Engineering Software*, vol. 90, pp. 22–40, 2015.
- [18] K. A. Danelson, A. J. Golman, A. R. Kemper et al., "Finite element comparison of human and hybrid III responses in a frontal impact," *Accident Analysis & Prevention*, vol. 85, pp. 125–156, 2015.